Detection of Surface Contaminants on Aerospace Structural Composites Prior to Adhesive Bonding

---

A Dissertation

Presented to

the faculty of the School of Engineering and Applied Science

University of Virginia

---

in partial fulfillment

of the requirements for the degree

Doctor of Philosophy

by

Rodolfo I. Ledesma

December

2018

APPROVAL SHEET

This Dissertation
is submitted in partial fulfillment of the requirements
for the degree of
Doctor of Philosophy

Author Signature: ______________________

This Dissertation has been read and approved by the examining committee:

Advisor: Dr. James Fitz-Gerald

Committee Member: Dr. Robert Weikle

Committee Member: Dr. Leonid Zhigilei

Committee Member: Dr. Thomas Katsouleas

Committee Member: Dr. John Connell

Committee Member: ______________________

Accepted for the School of Engineering and Applied Science:

Craig H. Benson, School of Engineering and Applied Science

December 2018

To my loving wife and supportive family

Abstract

Aerospace structural composites, owing to their light weight and advantageous combination of mechanical properties, have enabled a substantial advancement in the fabrication of commercial aircraft. These composite materials have allowed optimization in aerospace design by reducing weight, thus enabling the construction of aircraft that have excellent fuel efficiency and release fewer emissions. Costs in aerospace design and manufacturing can also be decreased by the use of composite materials. Further advancement of composite materials depends on the advancement of adhesive bonding and related processes. Adhesive bonding provides for a large stress-bearing area, fatigue resistance, and high strength-to-weight ratio. By adhesively bonding aerospace composite structures, riveting and mechanical fasteners can be minimized or eliminated, and the necessity of structural alteration to fit the mechanical fasteners can be reduced, thereby taking maximum advantage of the inherent mechanical capabilities of the composites.

In this dissertation, laser induced breakdown spectroscopy (LIBS) and optically stimulated electron emission (OSEE) were studied as surface characterization techniques for the detection of trace contamination levels of silicone on carbon fiber reinforced polymer (CFRP) composites. An OSEE instrument developed by NASA was used to characterize the composite surfaces. Prior to adhesive bonding, the CFRP surfaces were coated with different silicone thicknesses to determine the effect of silicone on the fracture characteristics and failure modes of the bonded structures. The OSEE experiments were performed before and after laser surface treatment under various conditions. The failure modes from the double cantilever beam

(DCB) tests were correlated with the OSEE characterization results.

This research advanced the field of LIBS by investigating the mechanistic interaction of laser energies below 100 μJ, referred to as μLIBS. A novel LIBS system was designed, assembled, and used to experimentally characterize CFRP surfaces before and after laser surface treatment. The ability to detect and resolve levels of silicone contaminants on CFRP surfaces has been achieved in both bulk and thin films. The surface sensitivity of LIBS to detect ultralow level contaminants has now been proven. Time-resolved analysis was conducted to determine the optimal emission conditions of plasma plumes for LIBS. An ultraviolet (UV) picosecond laser source was used to determine the single pulse ablation threshold of CFRP substrates comprised of an epoxy matrix and carbon fibers.

LIBS and X-ray photoelectron spectroscopy (XPS) results were correlated to study the sensitivity and limit of detection (LOD) of LIBS to detect silicone contamination on CFRP surfaces before and after laser surface treatment. Different surface conditions, and thus different residual silicone concentrations, were produced by varying the laser powers. The CFRP surfaces were subsequently characterized by LIBS and XPS. It was found that LIBS demonstrated comparable surface sensitivity to that of XPS. Thus, LIBS could readily detect silicone concentrations below those known to be a threat to adhesive bonding. Overall, it was demonstrated that LIBS is an extremely sensitive, rapid, and practical technique to ensure that the CFRP surfaces are adequately prepared for adhesive bonding.

Acknowledgments

This work was possible with the supervision of Dr. John Connell. His support, encouragement, and advice during my doctoral program was immeasurably valuable. I am grateful for his guidance and leadership, which set an example for my academic and professional career. I thank Dr. Frank Palmieri for numerous thought-provoking discussions, guidance during my research, and support during the conferences I attended. I sincerely appreciate Dr. William Yost for his valuable encouragement, scientific rigorosity, and thoughtful conversations. I recognize the support and academic rigor of my advisor, Dr. James Fitz-Gerald. He has the best interest of his students at heart, and that is an outstanding trait among academic advisors.

I thank the Advanced Materials and Processing Branch at NASA Langley Research Center (LaRC) for hosting me during my doctoral research work. I acknowledge John Hopkins for laser operation and help with experimental instrumentation. I appreciate early support from Daniel Perey and Joshua Brown, at the Nondestructive Evaluation Sciences Branch, for several discussions and technical assistance with the OSEE instrument. I also thank several other scientists and technicians at NASA LaRC for meaningful conversations and technical support.

I am grateful for the support, guidance, and time dedicated to serving on my doctoral committee by Dr. Leonid Zhigilei, Dr. Thomas Katsouleas, and Dr. Robert Weikle. I am thankful for their interesting discussions and technical advice that greatly improved the content of this dissertation.

Finally, this journey was also possible with the support, help, and encouragement of my family, and my loving wife, Whitney Ledesma. Moreover, her help and patience with thorough proofreading have enhanced the quality of this dissertation. Special thanks are extended to my uncle Cesar Goyzueta, who was a great support and guidance in my early academic life to study Engineering.

Contents

List of Tables

List of Figures

Acronyms

AWT	Aerosol wetting test
CCD	Charge-coupled device
CFRP	Carbon fiber reinforced polymer
DCB	Double cantilever beam
EDS	Energy-dispersive X-ray spectroscopy
FEP	Fluorinated ethylene propylene
FTIR	Fourier transform infrared spectroscopy
FWHM	Full width at half maximum
HAZ	Heat affected zone
ICCD	Intensified CCD
LIBS	Laser induced breakdown spectroscopy
LOD	Limit of detection
LTE	Local thermodynamic equilibrium
LPMV	Low-pressure mercury vapor
OSEE	Optically stimulated electron emission
PDMS	Polydimethylsiloxane

SBR	Signal-to-background ratio
SEM	Scanning electron microscopy
SNR	Signal-to-noise ratio
UV	Ultraviolet
VASE	Variable angle spectroscopic ellipsometry
WCA	Water contact angle
XPS	X-ray photoelectron spectroscopy
XRF	X-ray fluorescence

Nomenclature

$\alpha(\lambda)$	Absorption coefficient at a given wavelength λ
$\Delta\lambda_D$	Doppler broadening
$\Delta\lambda_N$	Natural broadening
$\Delta\lambda_S$	Stark broadening
$\Delta\lambda_{\text{shift}}$	Stark shift
ΔE	Uncertainty of the energy state
δ	Effective optical penetration depth
ϵ_b	Total bremsstrahlung emission
γ	Grating blaze angle
λ_B	Grating blaze wavelength
ν	Photon frequency
ϕ	Work function
ρ	Density
σ_b	Standard deviation of spectrally quiet region
ξ	Atomic ionization energy

A	Hamaker coefficient
a	Grating groove spacing
A_e	Cross-sectional area of focused laser beam
A_{ki}	Emission transition probability from upper level k to lower level i
c	Speed of light
c_L	Concentration limit of detection
d	Electron impact shift
D_0	Diameter of a Gaussian beam waist
d_a	Single-shot ablation depth
d_s	Distance of separation between a spherical particle and a flat surface
d_{pitch}	Line pitch
E_j	Atomic free-bound transitions
E_p	Laser pulse energy
$E_{\max}$	Maximum electron kinetic energy
E_{th}	Threshold laser pulse energy for ablation
F	Fluence
f	Laser pulse rate or frequency
F_p	Peak fluence
F_{LW}	London-van der Waals force
g_b	Gaunt factor

h	Planck's constant
I	Intensity
i	OSEE photocurrent
I_p	Background-corrected peak height
I_{th}	OSEE threshold photocurrent
l	Film thickness
M	Atomic mass
M_m	Molecular weight
N	Number of channels
N_A	Avogadro's number
n_A	Areal number density
n_c	Critical electron density
n_D	Number of particles in the Debye sphere
n_e	Electron density
N_g	Number of grooves on a grating surface
P_{avg}	Laser average power
R	Resolving power of a grating
S	Analytical sensitivity
v_{scan}	Scan speed
w	Electron impact width

Chapter 1

Introduction

In the aerospace industry, the use of carbon fiber reinforced polymer (CFRP) composites has enabled significant weight and fuel savings, leading to more economical and environmentally friendly (fewer emissions) large transport aircraft. To further advance aircraft performance and reduce manufacturing costs, efforts to reduce weight focus on replacing riveting and other mechanical fasteners with adhesive bonding of the CFRP composite materials [1]. Adhesive bonding plays a key role in the transition to lightweight structures for aircraft. Adhesive bonding is used in secondary aircraft structures (e.g. flight control surfaces, leading and trailing edges, and engine cowls) and has demonstrated excellent reliability. The use of mechanical fasteners and rivets increases the manufacturing complexity and the assembly weight, and alters the structural design of the composite materials by drilling holes to fit the arrest features. Some major advantages of adhesive bonding are that it provides a large stress bearing area, fatigue resistance, and a high strength-to-weight ratio. Presently, for primary structures on commercial transport aircraft to meet certification criteria designated by the Federal Aviation Administration (FAA) [2], adhesively bonded primary assemblies often rely on arrest features to prevent catastrophic failures if their critical limit design load is experienced. In cases where failures have occurred, the cause is often traced back to improper treatment of materials and insufficient process controls. Pre-bonding process controls for surface preparation, combined with characterization methods, will ensure that the surface has been chemically activated and is free of the contaminants which may cause inadequate bonding.

Therefore, pre-bonding surface treatment and surface contamination detection are necessary to enhance the quality of the adherend surface of aerospace composites prior to adhesive bonding and to improve the reliability of the bonded structures. This analysis is required in order to meet the FAA-designed certification criteria for aircraft structures. From a practical viewpoint, the ability to detect contaminants must be sensitive, rapid, and amenable to automation in order for it to be adopted by the industry.

Silicone based mold release agents are used during the fabrication of CFRP parts and can cause surface contamination. Silicone can penetrate hundreds of nanometers into the CFRP matrix [3, 4], and depending on the composite and associated processes (surface treatment, adhesive, and bonding method), silicone contamination can interfere with bonding even at low concentrations (< 1 μg/cm^2) [5, 6].

Laser ablation is a method that has been under research for the past decade at NASA Langley Research Center (LaRC) for surface preparation of aerospace materials. Laser treatment can be used to remove contaminants from CFRP surfaces, and roughness can be created by the adequate adjustment of laser parameters, such as the laser pulse power, scan speed, and pulse frequency. The laser-solid interactions can be controlled by optimizing the laser ablation parameters. In this way, superficial contaminants can be selectively and efficiently removed without damaging the underlying carbon fibers and the CFRP substrate [5–9].

1.1 State of the Art

Currently, surface characterization of adherend surfaces prior to adhesive bonding is performed off-line or ex-situ. Common techniques employed for surface characterization include: X-ray photoelectron spectroscopy (XPS), Fourier transform infrared spectroscopy (FTIR), water contact angle (WCA), aerosol wetting test (AWT), and X-ray fluorescence (XRF). In the case of XPS, the samples require preparation and destructive sizing to fit the analysis vacuum chamber, and testing and analysis are time consuming. FTIR, specifically the diffuse reflectance technique, requires multivariate analysis due to the multiple spectral peaks detected in CFRP materials, increasing the time required to detect contaminants. Depending on the type of FTIR instrument, the sample preparation can be destructive or non-destructive (as in the case of handheld devices). With the WCA method, the inspected area is small, and the technique requires depositing small droplets on the surface. A more automated technique, that covers larger areas, is AWT, which consists of software-based analysis of the droplets sprayed on the inspected surface. The droplets used for analysis must be removed prior to bonding and can potentially change the surface chemistry and degrade the surface conditions for adhesive bonding. XRF is a technique used to measure constituents in the substrate bulk and shows higher limits of detection (LOD) in comparison to other characterization techniques such as XPS. However, off-line analysis may be required for quantification and can be time consuming. As with other handheld device for surface characterization, XRF handheld devices provide portability but detection sensitivity is compromised.

1.2 History of Optically Stimulated Electron Emission

Optically stimulated electron emission (OSEE) is based on the photoelectric effect, which is the ejection of electrons by irradiation of light on a material. The origins of OSEE are thus closely related to the theory of the photoelectric effect. In 1887, Hertz designed a transmitter based on an induction coil, a Leyden jar, and a spark gap. The receiver was a ring with two metallic electrodes and a spark gap. Hertz reported [10] that a brighter spark at the receiver's spark gap was observed when ultraviolet (UV) radiation was received from the transmitted electromagnetic waves. Hertz put the receiver in a dark enclosure in order to see the dim spark more easily and found that the spark intensity decreased. Then he used glass, which blocked the emitter's UV radiation, therefore no spark was produced. When quartz was used instead, the spark intensity was re-established. Though Hertz observed and reported the photoelectric effect, he made no attempt to explain or elaborate a theory. In 1888, Hallwachs simplified Hertz's experimental setup to explain his observations [11]. Hallwachs used a polished zinc plate, which was connected to a gold-leaf electroscope. When the zinc plate was negatively charged, and then exposed to UV radiation, discharge occurred rapidly. In contrast, when the positively charged zinc plate was irradiated, charge leakage did not occur. Hallwachs hypothesized that electricity was produced by negatively charged bodies exposed to UV light. In 1899, Thomson published experimental results with a cathode in a vacuum tube [12]. He proved that the cathode irradiated by UV light discharged “negative corpuscles” (later named electrons), producing “negative electrification” (current). Those “negative corpuscles” were the same charged particles found in the cathode rays. In the same manuscript, he reported the charge of an electron. In 1902, Lenard published his findings on the photoelectric effect based on an apparatus comprised of a photocell, a carbon arc light source, a voltage source, and an ammeter [13]. He described the kinetic energy of an ejected electron as dependent not on the incident light intensity but on its frequency (wavelength). He was able to measure the electron kinetic energy and found that a critical voltage stopped the electron mobility. Also, the incident light intensity increased the number of photoelectrons but their energies remained the same. The photoelectric effect observed by Lenard was later explained by Einstein [14], who postulated that the light was comprised of discrete energy quanta, that later were called photons. The light energy quantum interacts with an electron in the surface and is transformed into the kinetic energy of the ejected electron. The maximum kinetic energy can also be calculated based on the minimum energy (work function characteristic to the material) required to eject an electron. Millikan confirmed Einstein’s quantum analysis about the photoelectric effect [15, 16].

In 1975, Smith measured photoemissions [17] from Al and Ni and was able to determine the oxide film thickness (0 to 200 Å). In 1980, controlled silicone contaminated Al alloys (painted and unpainted) were examined by Smith using OSEE [18]. He compared photoelectron emission and ellipsometry, concluding that photoelectron emission provided superior results, since it could be reliably applied to either painted or unpainted surfaces. For the purpose of contamination detection before the application of coatings, Smith continued his work and reported photoelectron emissions from Al and epoxy-painted Al surfaces [19]. In 1986, the US patent 4590376 was granted to Smith for an apparatus to assess surface cleanliness based on induced photoelectron emission [20]. The UV-light-induced photocurrent provided information about the quality and surface condition of the irradiated material. Preliminary work in metal substrates by Welch et al. [21] improved the performance of the OSEE technique. The report included an analysis of the OSEE response based on the physical interactions during the UV exposure. The OSEE unit was also characterized by the current-voltage response using a steel substrate. In addition, the implemented OSEE device included an argon purge of the working area to improve the measurement reproducibility. Another finding was that 95% of the OSEE photocurrent was produced by the 185 nm emission line of the UV light source. Consequently, in 1995, Yost et al. [22] were granted a patent for a quality monitor based on OSEE. The novel improvements over the conventional OSEE monitor included reproducibility allowed by, for example, temperature control of the UV lamp and an argon purge to avoid interactions with air, increased sensitivity owing to implementation of a parallel electric field for electron collection, and extension of OSEE applications to non-metallic substrates. The OSEE probe and the control unit were described in detail by Perey et al. [23].

1.3 History of Laser Induced Breakdown Spectroscopy

The origins of laser induced breakdown spectroscopy (LIBS) certainly start with the conception and invention of the laser. In 1957, Gould, then a graduate student at Columbia University, used the acronym LASER (light amplification by stimulated emission of radiation) on a page of his notebook describing his design of the optical resonator (Figure 1.1). Gould presented his work about LASER in a conference in 1959 [24]. During the same time frame, in 1958, Schawlow and Townes published a paper [25] that describes the theory and principles of an optical maser, which could produce oscillations in the infrared or optical regions by pumping incoherent light.

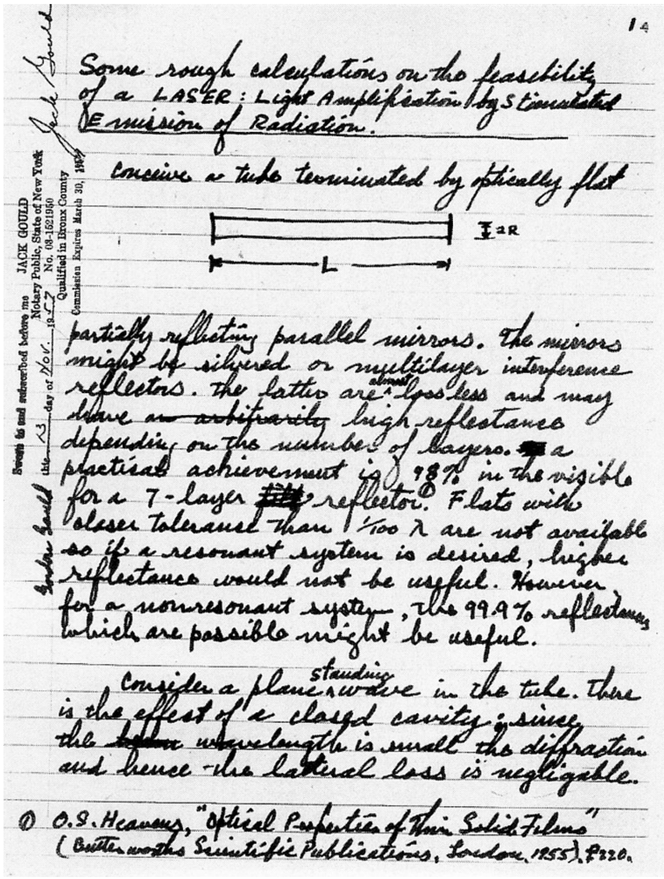

14

Some rough calculations on the feasibility
of a LASER: Light Amplification by Stimulated
Emission of Radiation.

Conceive a tube terminated by optically flat

partially reflecting parallel mirrors. the mirrors might be silvered or multilayer interference reflectors. the latter are almost lossless and may have ~~an arbitrarily~~ high reflectance depending on the number of layers. a practical achievement is 98% in the visible for a 7-layer reflector.① Flats with closer tolerance than 1/100 λ are not available so if a resonant system is desired, higher reflectance would not be useful. However for a nonresonant system, the 99.9% reflectance which are possible might be useful.

Consider a plane standing wave in the tube. there is the effect of a closed cavity; since the wavelength is small the diffraction and hence the lateral loss is negligible.

① O.S. Heavens, "Optical Properties of Thin Solid Films" (Butterworths Scientific Publications, London, 1955), p. 220.

Sworn to and subscribed before me this 13 day of Nov. 1957
JACK GOULD
Notary Public, State of New York
No. 03-1621950
Qualified in Bronx County
Commission Expires March 30, 19

Jack Gould

Gordon Gould

Figure 1.1: Gould's notebook page that describes the fundamental element of the laser. This page is where he coined the acronym LASER, and it was notarized in 1957.

In 1960, the US patent 2929922 [26] was granted to Schawlow and Townes, under Bell Telephone Laboratories, for their optical maser, which is currently called laser. In 1960, Maiman developed the first working laser. The implementation of the ruby laser included a high-power flash lamp as the pump source. His findings were reported in a brief article in 1960 [27].

During the mid-1960s, a technique that can be described as laser-ablation electrode-discharge optical emission spectroscopy (LA-ED-OES) was performed for elemental micro-analysis. In LA-ED-OES, the laser-induced plasma plume expands and passes through two electrodes held at high voltage. The electric discharge excites the atoms in the plume, increasing the spectrum intensity [28–31]. Atomic emissions from the plasma plume are recorded. In

1962, LA-ED-OES was reported in a meeting abstract by Breck and Cross [28]. The authors presented the vaporization of metallic and non-metallic samples using a ruby laser. They highlighted that LA-ED-OES is an improved technique over conventional arc-spectroscopy because of its ability to examine non-conducting samples. Jarrell Ash commercialized Breck's apparatus, which was called Laser Microprobe (Figures 1.2 and 1.3) [29]. The technique was named micro-emission spectroscopy.

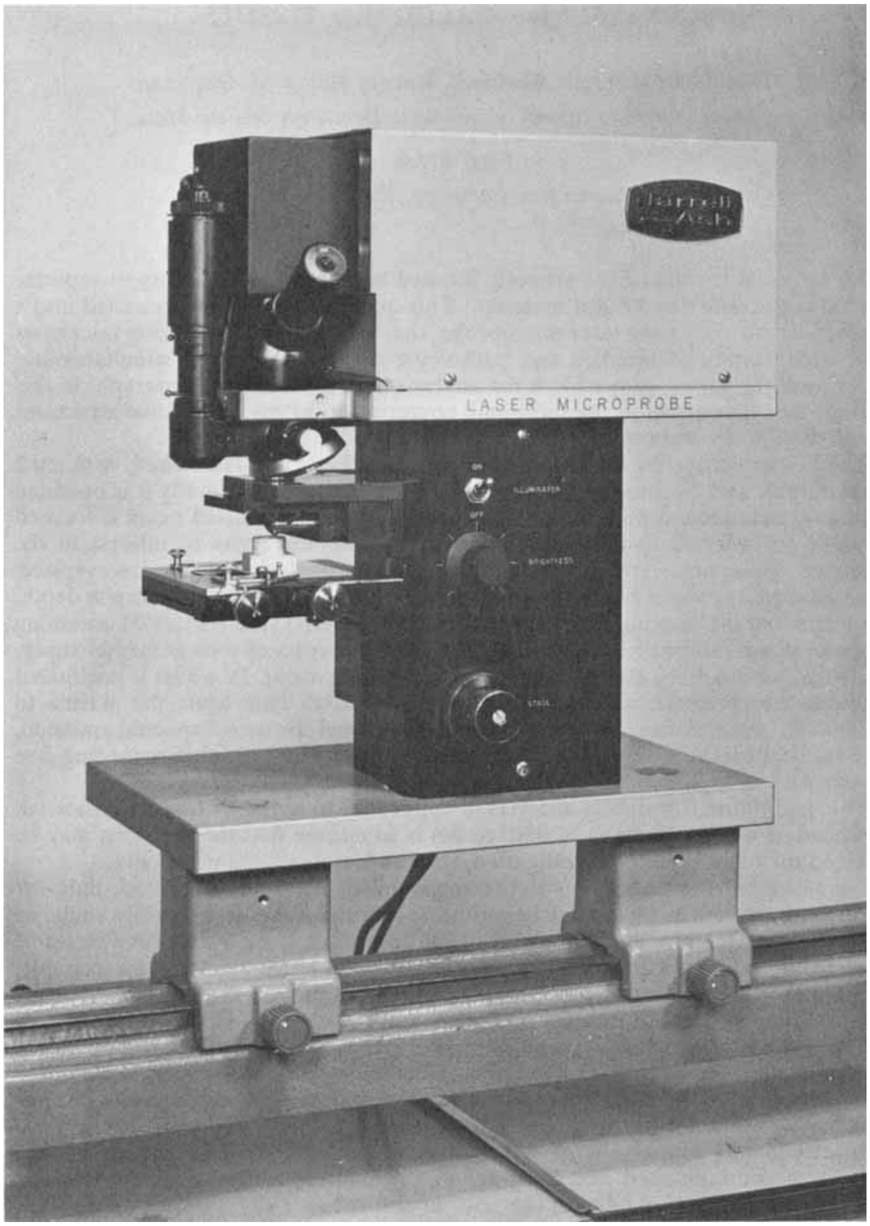

Figure 1.2: Laser Microprobe manufactured by Jarrell Ash. (Reprinted from [29] with permission of John Wiley and Sons.)

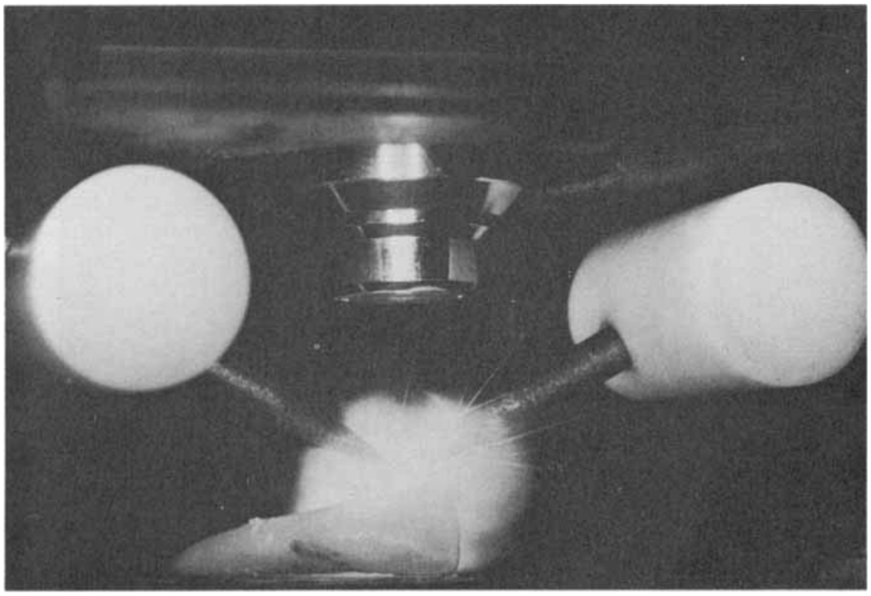

Figure 1.3: An electric spark discharged by two electrodes on a laser induced vapor, above the specimen. (Reprinted from [29] with permission of John Wiley and Sons.)

In 1963, Maker et al. [32] reported the first optical breakdown in a gas. Also, seminal work on time-resolved plasma emission and plasma-matter interactions were published by Ready [33]. In 1964, Runge et al. [34] showed spectrochemical analysis of three stainless steel standard samples, with a technique now known as LIBS. The authors used a ruby laser operated in Q-switched mode, with pulse widths of 15 to 20 ns and pulse energies of 50 to 75 mJ. They reported the analytical (calibration) curves for Ni and Cr in the steel samples. In 1965, Debras-Guedon et al. [35] published spectrochemical results using an electrode-less apparatus with a microsecond ruby laser (694.3 nm wavelength). They also reported the detection of molecular bands. Quantitative results of chromium in steel substrates were documented. The same year, in Germany, VEB Carl Zeiss Jena manufactured the LMA instrument for spectral analysis of laser-induced plasmas. The introduction of the instrument occurred at the Leipzig Spring Fair in 1965 [36]. Additionally, the first results using this instrument were published [37,38]. In 1967, Rasberry et al. [31] used a 35 ns Q-switched ruby laser to perform laser ablation to vaporize target samples, followed by a spark discharge on the ionized vapor. Comparison of the results with and without the spark excitation (using

LA-ED-OES and LIBS, respectively) was performed. They concluded that LA-ED-OES spectra yielded sharper, less self-absorbed, and more intense peaks. Daiber and Winans reported lifetime and time-resolved analysis from laser-induced breakdown plasmas [39] in 1968. In previous work, reported in the Bulletin of the American Physical Society in 1965, breakdown plasmas of gases were investigated. The measurements [39] were performed in nitrogen and argon using an interference-filter-photomultiplier tube to record the time history of the radiation. The excitation source was a ruby laser with a maximum pulse energy of 9 J and pulse widths of 10 to 40 ns. From the spectroscopic measurements, the authors concluded that atomic emission characteristics varied depending on the ionization degree, and that the emission lines outside the continuum emission were not so broad as when the emission was in the high-density plasma and buried in the continuum.

In 1971, Schroeder et al. [40] reported an electronic circuit that gated a photomultiplier and integrated the signal current. This device was utilized for time-resolution applications in spectrochemical and laser-plasma studies. In 1978, Belyaev et al. [41] reported the spectrochemical analysis of solid aerosol particles using CO_2 laser pulses. In 1981, Loree and Radziemski [42] coined the term LIBS. The authors conducted time-integrated LIBS experiments and reported the detection of atomic species in gases and gas-entrained particulates. The LIBS apparatus was comprised of a Q-switched Nd:YAG laser operating at 1064 nm with pulse energies of 0.1 to 1 J. The detector was an intensified silicon photodiode array coupled to a multichannel analyzer. During 1983 and 1984, studies were performed for the detection of hazardous gases, aerosols, and liquids [43–45].

In 1995, Häkkänen et al. [46] published the first paper on the use of LIBS with microjoule pulses. Around 1995 and 1996, remote analysis by LIBS using fiber optic cables was investigated for detection of Ba and Cr in soil [47], and Pb in dry paint [48]. In 1998, Bauer et al. [49] documented a LIBS instrument using an echelle spectrograph connected to a time-gated intensified charge-coupled device (ICCD) camera. The paper highlighted the wide range of the echelle-based instrument for the detection of all analytes in the target solids. Calibration-free LIBS (CF-LIBS) was introduced in the paper by Ciucci et al. [50] in 1999. The method was proposed for quantitative analysis based on the characteristics of the laser-induced plasma. Some assumptions were taken into account for the application of the CF-LIBS algorithm, for example, that the plasma composition is representative of the target material, and that the induced plasma is in local thermodynamic equilibrium (LTE).

In 2000, the first international conference on LIBS was held in Pisa, Italy. That first international conference demonstrated the growth and progress of LIBS as an easy-to-use and versatile spectrochemical analysis technique.

In 2001, the term micro-LIBS or µLIBS was introduced, initially to refer to ablation craters of dimensions in the micrometer range [51]. Currently, the term is most commonly used to refer to LIBS using microjoule laser pulses [52]. Depending on the application context, the term µLIBS can be used to denote either definition.

In terms of books on the subject, Radziemski and Cremers edited Laser-Induced Plasmas and Applications [53] regarding the theory and applications of LIBS, published in 1989. The book captured the growing interest in LIBS and the development and applications of the technique. The LIBS-relevant chapters covered the physics of laser-induced breakdown (Chapter 1), laser plasma diagnostics (Chapter 3), and laser-induced spectrochemical analysis (Chapter 7). Books specializing in LIBS were published and edited by Miziolek, Palleschi, and Schechter (2006) [54], Cremers and Radziemski (first edition, 2006) [55], Singh and Thakur (2007) [56], Noll (2012) [57], and Musazzi and Perini (2014) [58]. Additionally, two comprehensive and important reviews were written by Hahn and Omenetto [59,60]. The first review (2010) covered the diagnostics of laser-induced plasmas and the second part (2012) focused on instrumentation and analytical approaches.

An important milestone in LIBS history is its application to extraterrestrial material analysis [61]. NASA developed the Mars Science Laboratory rover “Curiosity” (Figure 1.4). Figure 1.4 shows a self-portrait image of Curiosity, which is a reconstruction from dozens of images [62]. The exploration rover included a chemistry and camera (ChemCam) instrument which was comprised of a LIBS instrument and a remote micro-imager (RMI) to deliver high-resolution images of the target morphology [63]. The operation of the rover started in mid-August 2012.

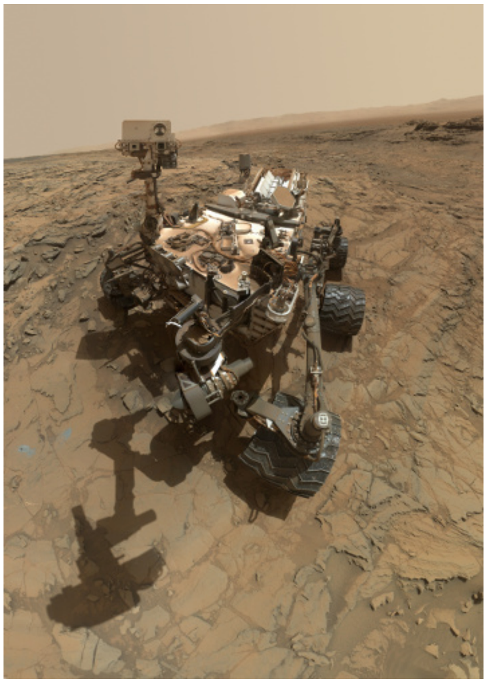

Figure 1.4: Mars Science Laboratory rover "Curiosity". The image was reconstructed from dozens of self-photographs. The rover landed on Mars in mid-August 2012. (Credit: NASA/JPL-Caltech/MSSS)

The increasing interest in LIBS is reflected in the number of publications over the last two decades. The data shown in Figure 1.5 were obtained from the SAO/NASA astrophysics data system (ADS). The data set is not comprehensive but indicates the increasing trend in LIBS publications. The data set was compiled using the keywords "laser induced breakdown spectroscopy".

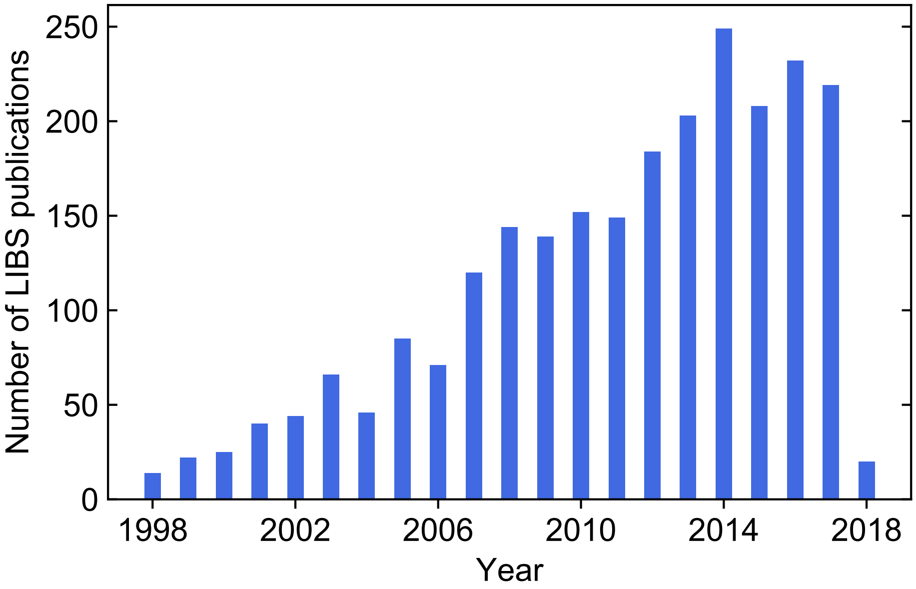

Figure 1.5: Number of LIBS related publications during the last 20 years. The data for 2018 was compiled on January 17, 2018.

1.4 Applications of Aerospace Structural Materials

1.4.1 OSEE

Gause presented the results of his OSEE experiments, for which he used a commercial contamination sensing device [20] on a D6AC steel based solid rocket motor (SRM) surface contaminated with Conoco HD-2 grease [64]. OSEE was used as a pre-bonding, nondestructive surface inspection technique. The experiments involved different grease concentrations. He demonstrated the correlation between contamination levels and OSEE responses, and the contaminant's effect on the strength of bonding between the D6AC steel and rubber insulation. Allen et al. [65] performed OSEE measurements, using a commercial unit, for CFRP and Al surfaces prior to bonding. The CFRP surfaces were contaminated with silicone and hydraulic fluid, while the Al surfaces were coated with silicone and polytetrafluoroethylene (PTFE). In the same work, the effectiveness of solvent cleaning was investigated using OSEE. Epstein and Shlanger [66] published a review in which they discussed the theory, operation, and applications of OSEE for surface contamination sensing on aerospace materials (e.g.

graphite-epoxy skin on aluminum honeycomb) for improved efficacy in bonding, coating, and welding processes. To enable more consistent analysis, the review also provides experimental considerations for OSEE, such as the humidity and the distance between probe and surface. Mattes reported the OSEE theoretical background and the instrumentation used at Thiokol Corp. over seven years since 1987 [67]. The report focused on the progress of detection of Conoco HD-2 grease on the SRM. Welch and Yost explained the advancements of the OSEE technique based on their work with an OSEE device implemented by NASA [21]. For example, they discussed how contamination changes the surface chemistry and thus, the surface work function, and how the sensitivity of OSEE to contaminants is affected by light absorption [68]. Lingbloom published a review article [69] about surface inspection of the RSM hardware and the theory, calibration, and production environment for the OSEE instrument implemented at ATK Launch Systems (former Thiokol Inc.). He also included the contributions of NASA to advance the technique. Brune et al. [70, 71] investigated OSEE as a surface quality control tool for CFRP composites and steel substrates prior to adhesive bonding.

1.4.2 LIBS

Markus et al. [72] performed LIBS analysis on CFRP materials for detection of different contaminants, e.g. polydimethylsiloxane (PDMS), hydraulic fluids, and fingerprints. According to their XPS analysis, the amount of surface PDMS was 1 nm. The authors used a Nd:YAG laser at 1064 nm and were able to identify the contaminants based on their atomic emission lines. The authors concluded that LIBS is a feasible technique to provide quality control when preparing CFRP surfaces for adhesive bonding. Tornow et al. [73] reported the applications of extended non-destructive testing (ENDT) using LIBS, OSEE, and AWT on CFRP composites for the detection of different contaminants, including silicones, before adhesive bonding. Regarding LIBS, the authors used a 1064 nm Nd:YAG laser and an echelle spectrograph combined with a ICCD detector. LIBS was tested for detection of silicone-based release agents and hydraulic oil. One main conclusion was that LIBS was able to characterize thin layers of silicone-based release agents on CFRP surfaces. The Extended Non-Destructive Testing of Composite Bonds (ENCOMB) project [74] investigated different surface characterization techniques, including LIBS. LIBS was used for the surface inspection of CFRP composites under conditions of contamination (e.g. hydraulic fluid, silicone mold release agents), thermal degradation, and moisture intake. In the most recent works, Palmieri et al. [6] and Ledesma et al. [75] performed microjoule LIBS using picosecond laser pulses on carbon fiber reinforced epoxy resin composites. Both works focused on this composite material system for improved adhesive bonding.

1.5 Research Overview

The research work presented in this dissertation aimed to develop effective methods to monitor laser surface treatment for sensitive detection of remaining surface contaminants, and to provide near-instantaneous, pre-bonding surface characterization. OSEE and LIBS were studied as non-destructive and rapid surface characterization techniques that provide opportunities to automate. At NASA LaRC, laser ablation is under investigation as a method to prepare aerospace structural surfaces. Thus, LIBS is the main focus of this research project since the same laser system can be used for both ablation and surface characterization. To advance the application of LIBS as a technique for non-destructive surface characterization of aerospace polymer composites, the laser-matter interaction during laser ablation using microjoule pulses was investigated. The aim was to decrease the amount of ablated material, thereby minimizing damage and improving surface sensitivity and quality of surface sensing. Reduced pulse energy for LIBS sensing is also advantageous since more economic laser systems and spectrometers can be implemented. Another task was to study the time-resolved spectra and achieve optimal signal-to-noise ratio (SNR) to enhance the detection of surface contamination. Because the industry requires rugged and amenable-to-automation techniques for in-line process control, LIBS and OSEE are posed as robust surface quality tools. The remainder of the dissertation is outlined as follows:

Chapter 2 presents a background review of OSEE and LIBS. Regarding OSEE, the optical absorption by surface contamination of the incident light and the photoelectric effect are explained. Concerning LIBS, relevant physics are discussed. μLIBS is briefly reviewed.

Chapter 3 describes the methodology utilized throughout this research work. Details on the OSEE light source and photocurrent response are described. The LIBS apparatus and its main optical components are presented. Description of the temporal calibration and LIBS signal analysis are included.

Chapter 4 covers the application of OSEE on CFRP surfaces. The correlation of OSEE and the failure modes of CFRP adherends after mechanical testing is investigated to assess the effects of surface contamination on adhesive bonding performance. Different surface conditions are analyzed by varying laser parameters in order to study their effect on the OSEE photocurrent response.

Chapter 5 reports an advancement of the LIBS technique by using picosecond microjoule pulses to non-destructively characterize CFRP surfaces. Ablation damage and surface sensitivity are studied for the laser parameters utilized for LIBS characterization.

Chapter 6 presents the investigation of the limits of detection of LIBS from calibration analytical curves by comparing the LIBS and XPS results.

Chapter 7 provides a summary of the research work. Future work is described for the applications of LIBS and OSEE.

Chapter 2

Background

2.1 OSEE

OSEE is a photoemission-based technique designed for inspection of surface cleanliness [64–71]. Contamination, adherent particles, and adsorbates on surfaces can be detected owing to changes in the photoelectron emission properties of the target surface. Chemistry changes of a surface cause an alteration of the electron work function and the mechanism through which electrons are emitted from the surface [14,76]. Thus, the work function of a surface is affected by its surface cleanliness.

2.1.1 Optical Absorption by Surface Contamination

In the OSEE technique, UV source radiation impinges on the target surface with photon energy $E = h\nu$, where h is Planck's constant and ν is the incident photon frequency. When a contamination film covers the top of a target surface, the incident intensity I_0 (i.e. $h\nu$ times the number of photons per unit area per unit time) from the UV light source travels through the contamination layer. The incident intensity undergoes photon absorption and scattering in the contamination layer. The relationship between the one-dimensional coordinate of the pathlength x and the OSEE photocurrent $i_t(x)$ is described by

$$i_t(x) = i_0 e^{-\alpha(\lambda)x} \tag{2.1}$$

where the absorption coefficient of the contaminant is $\alpha(\lambda)$, which depends on the wavelength λ. For a contamination layer whose thickness extends from $x = 0$ to $x = l$, the transmitted intensity I_t at $x = l$ that excites the surface is less than the incident intensity I_0 at $x = 0$.

As the UV radiation passes through the contamination layer, it produces a decrease in the intensity I_0. The incident intensity I_0 is proportional to the photocurrent i_0, and this is true when no contamination is present. However, when there is a contamination film on the target surface, the transmitted intensity I_t, after passing through the contaminant and striking the target surface, is proportional to the photocurrent i_t. Solving Eq. 2.1 for the contamination thickness l, the decrease in the photocurrent owing to an absorbing medium is given by

$$i_t = i_0 e^{-\alpha(\lambda) l} \tag{2.2}$$

Solving for l gives

$$l = \frac{1}{\alpha(\lambda)} \ln \left(\frac{i_0}{i_t} \right) \tag{2.3}$$

By applying Eq. 2.3, contamination thickness can be determined from photoelectron emission.

2.1.2 Photoelectric Effect

The impingement of the UV photons on the target surface affects the photoelectron emission from that surface. If a photon energy is high enough to eject an electron from the target surface, the ejected electron's kinetic energy is described according to the Einstein's equation, shown in Eq. 2.4 [14],

$$E_{\max} = h\nu - \phi \tag{2.4}$$

where $E_{\max}$ is the maximum kinetic energy of an electron emitted from the surface and $\phi = h\nu_0$ the work function of the target surface. If the target surface is contaminated, its work function will be altered. In addition, depending on the photoelectric work function of a contamination layer, a contaminant can be emitting or nonemitting. Photoelectron generation occurs when the incident energy is greater than the threshold energy of the target surface: $\nu > \nu_0 \rightarrow E > 0$. In addition, the difference between the source photon energy and the contamination-altered work function of the target surface affects the efficiency of the electron emission. Figure 2.1 shows the photoelectric effect for an emitting target surface (e.g. CFRP) contaminated with a nonemitting material (e.g. silicones). In comparison to the contaminated surface, the bare surface emits more electrons under UV light exposure.

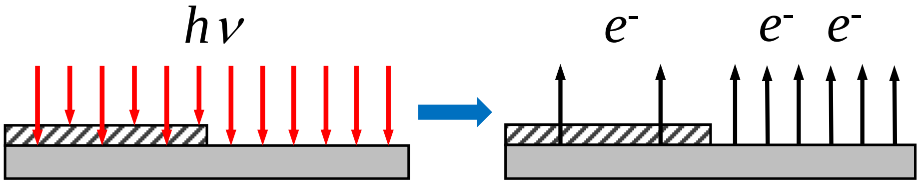

Figure 2.1: Schematic graph of the photoelectric effect when an emitting surface is coated with a nonemitting contamination layer. The uncontaminated surface emits more electrons.

2.2 LIBS

LIBS is an elemental characterization technique that utilizes an intense laser source to excite a material (solid, liquid, or gaseous) into a plasma state which emits light [34, 45, 77]. The optical emission from the plasma plume provides information about the elemental composition of the starting target material.

2.2.1 Laser-matter Interactions

For picosecond and ultrashort pulses, the primary interaction is laser-matter. During the laser pulse width, incident laser radiation interacts with electrons in the solid. The electrons in the substrate are heated by the laser pulse, and the transfer of energy to the lattice by collisions takes more time than the incident laser pulse duration. The laser pulse width is shorter than relaxation times (e.g. thermal relaxation time) of most solids. Therefore, the laser pulse interacts with the target surface entirely prior to plasma formation, improving ablation efficiency. If the laser electric field strength is very high, it will produce a high peak power [78] that will ionize both conducting and wide bandgap materials by multiphoton absorption [79], and the free electrons generated (also called seed electrons) can initiate electron avalanche ionization [80].

For nanosecond pulses, the incident laser pulse first interacts with electrons in the material, then the induced plasma plume interacts with the pulse trailing edge. In this pulse width regime, the main interaction is laser-plasma. The longer pulses produce significant heat transfer to the material bulk, leading to heating, melting, and vaporization. After the material is vaporized, free electrons in the plasma plume continue absorbing energy from the laser radiation (inverse bremsstrahlung [81]) during the remaining pulse duration [82], producing multiphoton absorption and avalanche ionization from the collision of free and emitted electrons. The expanding vaporized material is ionized by inverse bremsstrahlung, forming the plasma plume. In the case of multiphoton absorption, the ionization of atoms occurs when multiple photons are needed to remove an electron. Avalanche ionization is a consequence of inverse bremsstrahlung, which is the main mechanism in the absorption of laser radiation [80, 82]. In inverse bremsstrahlung, a photon is absorbed by a free electron during the collision with heavy particles. Because of the continuing absorption of laser radiation, electron energy rises to a higher state in the continuum. The energetic free electrons will ionize through collisions with other atoms, whose free electrons will continue absorbing energy from the laser [83]. Inverse bremsstrahlung absorption is more efficient in the IR than in the UV regime [84]. Since the temperature increases owing to electron collisions and multiphoton ionization events given continuing absorption of a laser pulse, the plasma plume can become dense enough to produce plasma shielding. High fluence also increases the likelihood of plasma shielding. The equation of the critical electron density n_c (in cm^{-3}), when plasma shielding occurs, is given by [85]

$$n_c = \frac{10^{21}}{\lambda^2} \tag{2.5}$$

where λ is the incident laser wavelength (in μm). Plasma shielding partially or completely obstructs the interaction of the laser pulse with the material and the core of the plasma plume. Plasma shielding decreases the laser ablation efficiency as the laser pulse radiation is screened by the dense plasma plume.

2.2.2 Plasma Emission Process

The high intensity laser radiation interacts with the electrons in the material, causing ionization. The resulting high-temperature dense plasma expands at supersonic velocities into the ambient gas [86]. During early stages of the plasma plume, free electrons, atoms, and ions collide and interact. At this time, the plasma emission is governed by continuum radiation caused by free-free transitions, or bremsstrahlung [87], along with free-bound transitions, or radiative recombination [88]. In bremsstrahlung, a free electron loses kinetic energy and emits photons at different wavelengths, and the electron remains free after emitting photons. In the recombination process, a free electron is completely stopped by the electromagnetic field of an ion. The free electron is then captured by the ion and the excess of kinetic energy is released as photons, producing recombination radiation. The continuum emission frequencies from radiative recombination are given by [89]

$$h\nu = \xi - E_j + \frac{1}{2}mv^2 \tag{2.6}$$

where ξ is the ionization energy of the atom, E_j the free-bound transitions, and $\frac{1}{2}mv^2$ the kinetic energy of the free electron.

For picosecond and ultrashort pulses, the laser-plasma interactions decrease with the pulse duration, since the primary interaction is laser-matter, which affects the electrons in the solid [90–92]. The electrons are heated by the laser pulse, and the transfer of energy to the lattice by collisions takes longer time than the incident laser pulse duration [90, 91, 93–96].

In the nanosecond laser regime, the laser pulse duration remains after the plasma formation, thus the laser beam interacts with the plasma plume as it expands. The plasma plume increases in temperature owing to the electron collisions as free electrons continue absorbing the laser energy by inverse bremsstrahlung. This phenomenon also contributes to the prolonging the plasma lifetime. Assuming a Maxwellian distribution of the electron velocity, the bremsstrahlung emission (in W/cm^3/Hz) is expressed by [97]

$$\epsilon_b(\lambda) = 6.3 \times 10^{-47} n_e n_i z^2 g_b(\lambda, T)(kT)^{-1/2} e^{-hc/\lambda kT} \tag{2.7}$$

where n_e and n_i are the electron density and ion density, respectively, z the effective ionic charge, $g_b(\lambda, T)$ the Gaunt factor, T the electron temperature (kT in eV), and k the Boltzmann constant. After integrating Eq. 2.7 over all wavelengths, $\int_0^\infty \epsilon_b(\lambda) d\lambda$, the total bremsstrahlung emission (in W/cm^3) is given by [97]

$$\epsilon_b(\lambda) = 1.5 \times 10^{-32} n_e n_i z^2 \bar{g}_b (kT)^{1/2} \tag{2.8}$$

where $\bar{g}_b$ is the wavelength-averaged Gaunt factor. As the plasma plume expands and cools down, bound electrons in atoms and ions descend through the quantized energy states, producing characteristic emission lines [98]. This process is called bound-bound transition and is responsible for the optical emission lines. In this process, the emitted photon that corresponds to the transition from state k to state i, has a wavelength λ_{ki} and frequency ν_{ki} as follows,

$$\lambda_{ki} = \frac{hc}{E_k - E_i} = \frac{c}{\nu_{ki}} \tag{2.9}$$

where h is Planck's constant, c the speed of light, and E_k and E_i the energies of the upper and lower state, respectively.

2.2.3 Laser Ablation

The ablation mechanism occurs after the ablation threshold of the material has been surpassed, and depends on material properties (e.g. binding energy, optical absorption), microstructure, laser pulse duration, laser power intensity, and laser photon energy. For example, in the nanosecond pulse regime, organic materials have lower threshold fluences (0.01-1 J/cm^2) than metals (1-10 J/cm^2) [99]. Threshold fluence may decrease owing to an increase of laser photon energy, generation of defects by multiple laser pulse irradiation (incubation), or introduction of dopants in the material.

Photothermal Ablation

The mechanism that removes material from the target substrate by laser-induced thermal degradation is known as photothermal ablation. If the laser pulse duration is long (e.g. nanosecond), the laser pulse will heat, melt, and vaporize the material. For nanosecond pulses, since the pulses are longer than electron-phonon relaxation times (a few picoseconds [100]), electrons and lattice are considered to be in local thermal equilibrium. Once the plasma is induced, the plasma plume will interact with the incident laser pulse trailing edge, producing a reheating of the plasma plume and a consequent increase in heat transfer to the solid. This thermal ablation will leave a heat affected zone (HAZ) behind. The HAZ exhibits thermal stress around the ablative crater edges, typically evidenced by redeposited or melted material. Laser power intensity can increase the thermal damage if the laser photon energy is much less than the bond-dissociation energy of the different molecules in the material. When long pulses (e.g. nanosecond) are used on metallic substrates, the availability of electrons in the conduction band allows the generation of seed electrons for plasma formation, subsequently creating a plasma plume from the matter that is melted and vaporized by thermal processes. In contrast, for polymers and other dielectrics, the electrons from the valence band need enough energy to be transferred to the conduction band to generate free electrons. If the intensity is high enough, non-thermal processes such as multiphoton absorption and impact ionization can enable the transfer of electrons to the conduction band. In polymers and wide bandgap dielectrics, thermal and non-thermal (photochemical) ablation mechanisms may coexist. Now, when excitation energies are below dissociation energies (< 3.6 eV [86]), the probability of photothermal ablation increases. Thermal ablation is produced by vibrational transitions in molecular collisions [86]. The excitation of vibrational modes in molecules leads to thermalization of the excitation energy. Ablation is produced by absorption of several localized quanta by chemical bonds, which will induce thermal desorption [86]. For long pulse widths and laser photon energies above 3.6 eV (e.g. UV laser wavelengths), the ablation mechanism become more complex and a combination of photothermal and photochemical ablation (photophysical ablation) is likely.

Photochemical Ablation

Photochemical ablation occurs when the photon energy of the laser beam is above the bond-dissociation energy of the molecules and binding energy of the atoms in the material. For nanosecond pulses, despite the fact that thermal relaxation times of polymers are some orders larger than a few picoseconds, photochemical ablation is possible for high photon energy pulses (e.g. in the UV range below 200 nm) [86], decreasing HAZ. In addition to high photon energy, photochemical ablation occurs if the laser pulse duration is very short and high peak power levels can produce direct ionization of the target material [78]. In this situation, most of the laser energy is transferred directly to the solid. Picosecond and ultrashort pulses excite the target surface rapidly. Because the relaxation times are longer than the laser pulse width, the laser pulse does not act as a heat source, and the excited electrons do not transfer the heat to the lattice. The energy transfer time from the electron to the lattice (electron-phonon relaxation time) is in the order of a few picoseconds [100]. Thus, there is minimal energy transferred to the regions outside the irradiated material volume, producing less thermal stress in the material. For polymers, if the laser intensity irradiated on the material is sufficient, bond dissociation occurs by multiphoton transition. This photochemical mechanism produces mechanical stress sufficient to break bonds, and the material is removed from the target surface by fragmentation [95, 101]. Multiphoton transition also produces seed electrons in the conduction band transferred from the valence band. Consequently, those electrons collide against other electrons in the valence band, increasing the electron density in the conduction band, initiating impact (avalanche) ionization. In the ultrashort pulse regime, a high-intensity (above 10 TW/cm^2 [80]) laser pulse can also produce cold ablation by Coulomb explosion [102]. Coulomb explosion occurs when free electrons create a strong electric field with highly ionized atoms. The ionized atoms on the surface have the same charge and an electrostatic repulsion leads to ejection of those ions from the substrate. Coulomb explosion is likely to occur in dielectrics and polymers owing to their wide bandgap and inhibited in metals and semiconductors by their high electron mobility to replenish the ionized surface. Non-thermal mechanisms govern the ablation of materials for short and ultrashort pulses and high photon energy pulses, typically in the UV wavelength range.

2.2.4 Spectral Line Analysis

Broadening of emission lines from laser-induced plasmas is caused by different mechanisms, for example, Stark, Doppler, and instrumental. In LIBS, it is important to understand these mechanisms in order to obtain physical parameters of the induced plasma, for example, electron density. In the following sections, the main broadening mechanisms in LIBS are discussed.

Natural Broadening

Natural broadening arises from the uncertainty of the energy state due to the finite lifetime of a particle (atom, ion, or molecule) in its excited state. This broadening is consistent with the Heisenberg uncertainty principle: $\Delta E \Delta t = \hbar$, where ΔE is the uncertainty of the energy state E above the ground state, Δt the lifetime of an excited state, and $\hbar$ the reduced Planck constant. Considering that the particle has an energy transition $k \rightarrow i \rightarrow 0$, the broadening has a Lorentzian profile with a full width at half maximum (FWHM) given by [103]

$$\Delta\lambda_N = \frac{\lambda^2}{2\pi c}\left(\frac{1}{\tau_k} + \frac{1}{\tau_i}\right) = \frac{\lambda^2}{2\pi c}\left(\sum_{p<k} A_{kp} + \sum_{q<i} A_{iq}\right) \tag{2.10}$$

where τ_k and τ_i are the lifetime of the upper and lower energy states, respectively. Natural broadening is negligible in LIBS plasmas in comparison to Doppler and Stark broadening effects [57].

Doppler Broadening

Doppler broadening is due to the Doppler effect caused by thermal motion of emitting particles (atoms, ions, or molecules). Assuming that the particles in motion have a Maxwellian velocity distribution, the broadened-emission line is Gaussian with a FWHM given by [104]

$$\Delta\lambda_D = 7.16 \times 10^{-7}(T/M)^{\frac{1}{2}}\lambda \tag{2.11}$$

where T is the radiating particle's temperature (in K), M atomic mass (in u), and λ the central wavelength of the emission line (in Å).

Stark Broadening

Stark broadening is due to the Stark effect, which is caused by collisions of emitting atoms and charged particles (ions and electrons). The Stark effect in plasmas therefore produces broadening and a wavelength shift of the atomic emission line, with a Lorentz profile:

$$L(\lambda) = \frac{\Delta\lambda_S/2\pi}{(\lambda - \lambda_0 - \Delta\lambda_{\text{shift}})^2 + (\Delta\lambda_S/2)^2} \tag{2.12}$$

where $\Delta\lambda_S$ is the Stark broadening of an emission line and FWHM, λ_0 the center wavelength at vacuum, and $\Delta\lambda_{\text{shift}}$ the Stark shift. The Stark broadening and the Stark shift can be estimated by [88]

$$\Delta\lambda_S = 2w\frac{n_e}{n_r}\left(1 + 1.75A\left(\frac{n_e}{n_r}\right)^{1/4}(1 - Bn_D{}^{-1/3})\right) \tag{2.13}$$

$$\Delta\lambda_{\text{shift}} = w\frac{n_e}{n_r}\left(\frac{d}{w} \pm 2A\left(\frac{n_e}{n_r}\right)^{1/4}(1 - B{n_D}^{-1/3})\right) \tag{2.14}$$

where the minus sign in Eq. 2.14 applies to lines with negative d/w at low temperature, w and d are the electron impact width and shift, respectively, n_e the electron density, n_r the reference density (10^{16} cm^{-3} for atomic lines and 10^{17} cm^{-3} for ionic lines [105]), A the ion broadening parameter, B is equal to 0.75 for neutral and 1.2 for ionic lines, respectively, and n_D the number of particles in the Debye sphere (in cm^{-3}) [88]:

$$n_D = 1.72 \times 10^9 \frac{T^{3/2}}{{n_e}^{1/2}} \tag{2.15}$$

where T is the electron temperature (in eV). Stark broadening is typically assumed to be dominant in contrast to Doppler or other broadening mechanisms in laser-induced plasmas [106], except for low pressure plasmas [107].

2.2.5 μLIBS

The extension of LIBS toward lower pulse energies, typically below 100 μJ, is known as μLIBS [46, 108–110]. The benefits of μLIBS include the use of the lower energy pulses and higher pulse frequencies that most modern laser systems can provide. In μLIBS, the decay time of the emission line couples with an even faster decay of the continuum emission, making possible the detection of the LIBS signal using ungated detectors [109, 110]. Figure 2.2 shows the normalized signal-to-background ratio (SBR) as a function of time for the Si I emission line at 251.6 nm [46]. The decay time increases as the pulse energy increases.

The low pulse energy and improved ratio of line to continuum emission in μLIBS can be optimized to achieve limits of detection comparable to those obtained by conventional LIBS, which is in the millijoule regime [108]. In addition, the ablation crater size decreases with lower pulse energies, and thus, the technique may be considered nondestructive with enhanced resolution [111, 112].

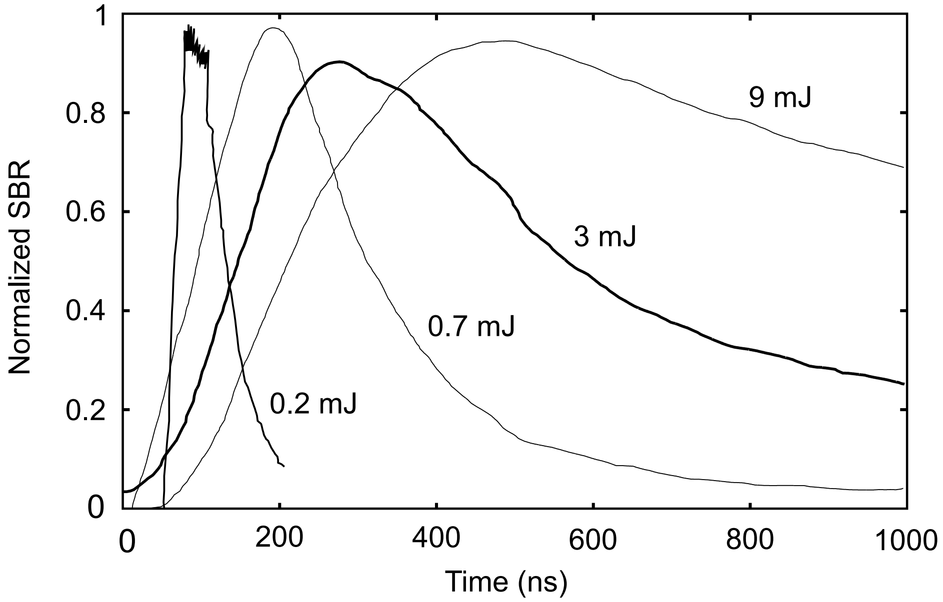

Figure 2.2: Normalized signal-to-background ratio (SBR) as a function of time for the Si I emission line at 251.6 nm. The decay time decreases for lower pulse energies. (Reprinted from [46] with permission of SAGE Publishing.)

Chapter 3

Methodology

3.1 OSEE

The OSEE probe head [23, 113] is comprised mainly of a low-pressure mercury vapor (LPMV) lamp, a shutter to control the UV light exposure, gas connections to purge the working area with argon, and a collector plate. The Hg emission line at 185 nm is responsible for 95% of the OSEE photocurrent. The collector plate was coated with chromium, and a parallel electric field (PEF) configuration was included to optimize the collection of electrons. The argon prevents chemical interactions on the surface with species in the ambient atmosphere when UV light is irradiated on the target surface. Figure 3.1 shows the OSEE photocurrent response and the different stages of the photocurrent time progression for a control CFRP surface. After the shutter opens completely, the initial photocurrent is stable for ∼400 ms. In Figure 3.2, the first derivative trace shows the moment when the shutter is completely open and the UV radiation is fully exposed on the surface. The moment the shutter opens completely is after ∼100 ms. Therefore, for reliability of data recording, the OSEE measurement was considered at ∼150 ms. At this point, the measurement of the OSEE signal was referred to as threshold current, I_{th}. From the threshold value, the current rises rapidly to a maximum point. After that, the current decreases monotonically. The recorded OSEE photocurrent provides a qualitative measurement of the surface condition with respect to a control surface.

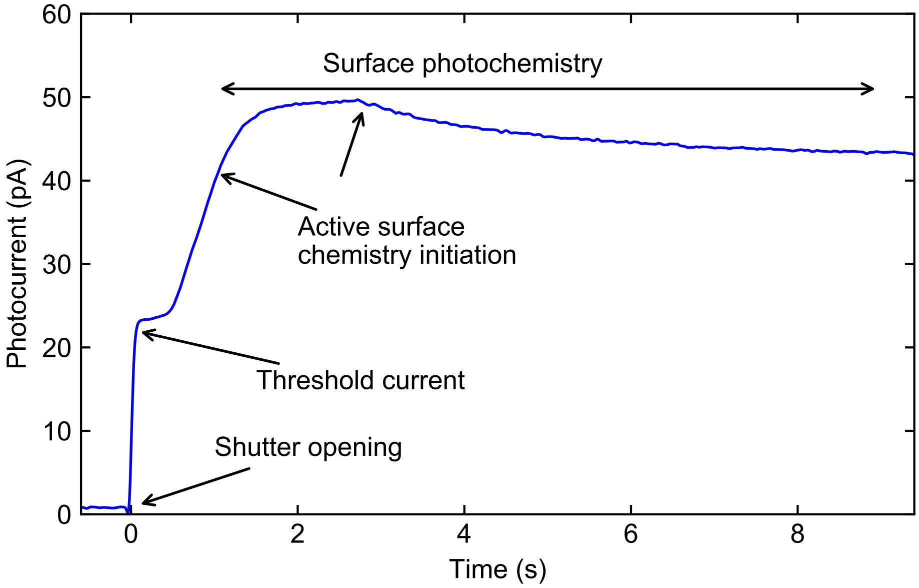

Figure 3.1: OSEE photocurrent regions. After the shutter opens completely, the initial photocurrent is stable for ∼400 ms. Once the current reaches its maximum, it decreases monotonically.

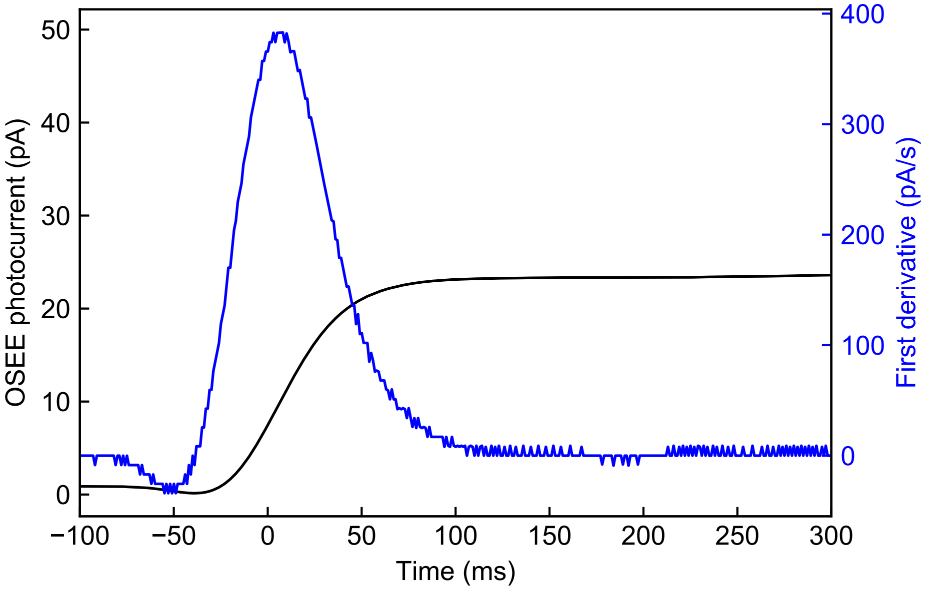

Figure 3.2: OSEE photocurrent signal and its first derivative. When the shutter opens completely after ∼100 ms, the first derivative signal is almost constant. OSEE measurements were considered at ∼150 ms.

3.2 LIBS

3.2.1 Spectroscopy System

Diffraction gratings are components in a spectrometer utilized to disperse the radiation from the laser induced plasma. Diffraction gratings can be transmissive or reflective. In reflective gratings, the incident wavefront is divided into different directions because of the equidistant reflective grooves on the grating surface. The diffraction grating equation is described by [114]

$$n\lambda = a(\sin\theta - \sin\varphi) \tag{3.1}$$

where n is the order of the principal maxima, λ the diffracted wavelength, a groove spacing, θ the diffracted angle, and φ the incident angle.

Reflective gratings can be non-blazed or blazed. Figure 3.3 shows the schematic of a blazed grating, also known as echelette grating.

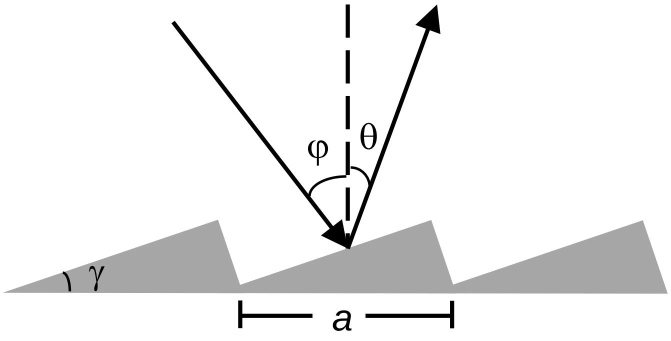

Figure 3.3: Schematic diagram of a blazed grating.

A blazed grating operates at a specific wavelength, called blaze wavelength. At the blaze wavelength, the highest efficiency of the grating is achieved. The blaze angle γ (Figure 3.3) is the angle at which the efficiency is highest. The blaze angle is the difference between the surface normal and the facet normal. The diffracted wavelength will be equal to the blaze wavelength when the incident and diffracted angles are equal to the blaze angle, $\gamma = \varphi = \theta$.

This definition can be described by the Littrow condition [114],

$$n\lambda_B = 2a\sin\gamma \tag{3.2}$$

where λ_B is the design or blaze wavelength.

The resolving power R of a grating is its ability to separate two adjacent spectral lines and is defined as [114]

$$R = \frac{\lambda}{\Delta\lambda} = nN_g \tag{3.3}$$

where λ is the observed wavelength, $\Delta\lambda$ is the minimum wavelength shift that can be resolved, and N_g is the number of grooves illuminated on the grating surface.

A common spectrograph for LIBS is the Czerny-Turner (CT) design. Figure 3.4 shows the schematic diagram of a CT spectrograph. This spectrograph has two concave mirrors and a grating. The light dispersed by the grating is imaged to the detector plane by the second concave focusing mirror.

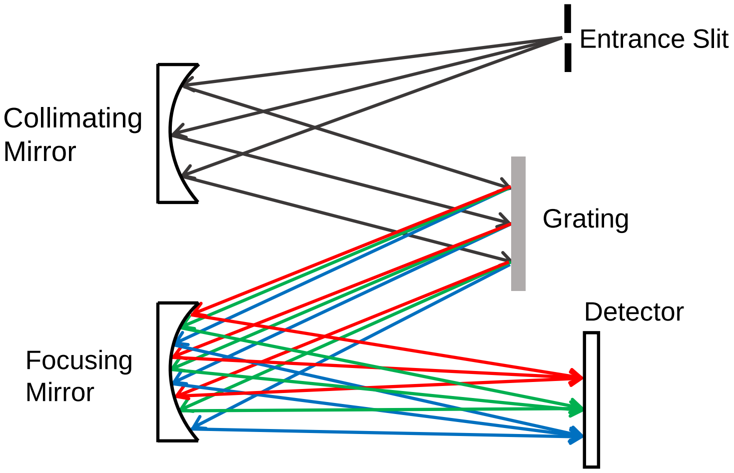

Figure 3.4: Schematic diagram of a Czerny-Turner spectrograph.

Schmidt-Czerny-Turner (SCT) spectrographs [115,116] are dispersion systems that improve upon the performance of Czerny-Turner spectrographs. SCT spectrograph design eliminates astigmatism and reduces spherical and comatic aberrations. This spectrograph is comprised of an entrance slit, a collimating mirror, a grating, an aberration corrector plate, and a focusing mirror. Figure 3.5 shows the schematic diagram of a SCT spectrograph. The plasma radiation enters by the entrance slit. The light is then collimated by the collimating mirror. The collimated beam is dispersed by the grating and the dispersed radiation is reflected by an aberration correction plate. The reflected beam is then imaged by the concave focusing mirror to the detector focal plane.

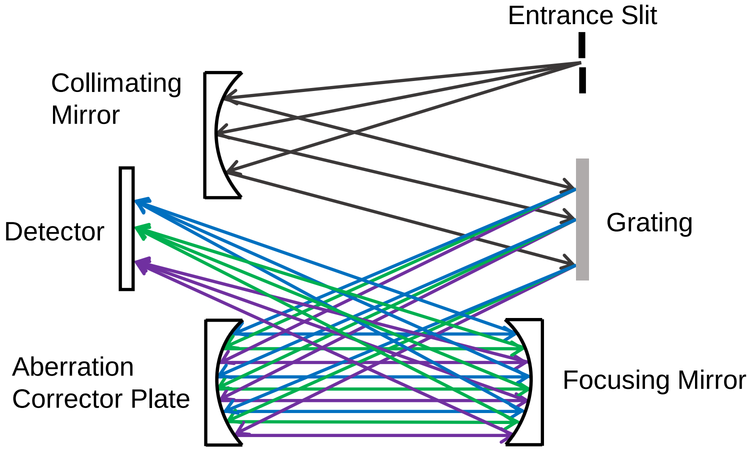

Figure 3.5: Schematic diagram of a Schmidt-Czerny-Turner spectrograph.

Figure 3.6 shows the comparison of the spectral response between a CT and a SCT spectrograph from a dispersed light source. In Figure 3.6a, astigmatic aberration is evident in the CT focal plane image. In contrast, Figure 3.6b shows an anastigmatic focal plane image from a SCT spectrograph.

Furthermore, the imaged radiation reaches the detector, which can be an electron-multiplier intensified charge-coupled device (emICCD) instrument. Figure 3.7 shows the schematic diagram of an emICCD detector. The incident photons strike the photocathode and are converted into electrons. The photoelectrons are accelerated by the bias voltage to the microchannel plate (MCP). The multiplied electrons from the MCP impinge on the phosphor screen, which converts the electrons back to photons. The larger number of photons are guided by fiber-optic coupling and collected on the active array of the CCD. The electrons from each pixel of the CCD are transferred to the electron-multiplication (EM) register. In the EM register, the electrons are multiplied by impact ionization process. Finally, the

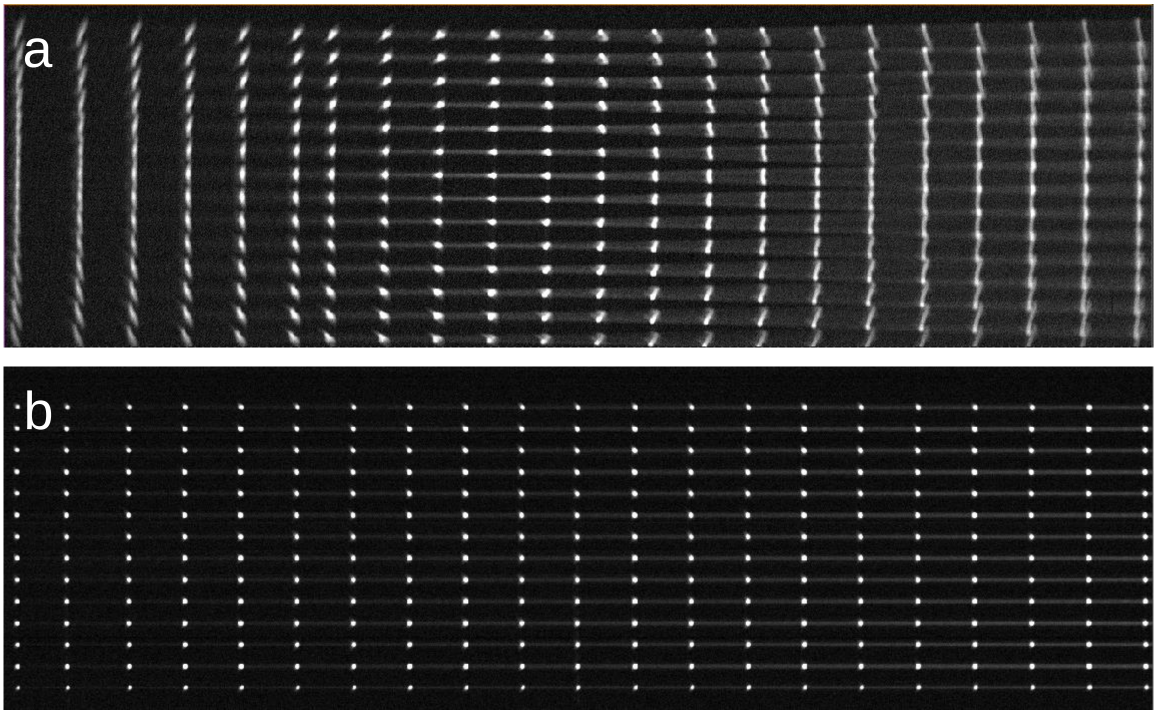

Figure 3.6: Focal plane images of dispersed light from a) a CT spectrograph showing aberrations, and b) a SCT spectrograph showing anastigmatic performance. (Printed with permission of Princeton Instruments.)

output of the EM register is sent to the analog-digital converter (ADC), from which the digitized output is read out to display the spectrally resolved light on a computer. The first multiplication process of photoelectrons in the detector occurs in the MCP. Figure 3.8 shows the schematic diagrams of an MCP and an individual channel. An incident electron is multiplied by the generation of secondary electrons within the channel.

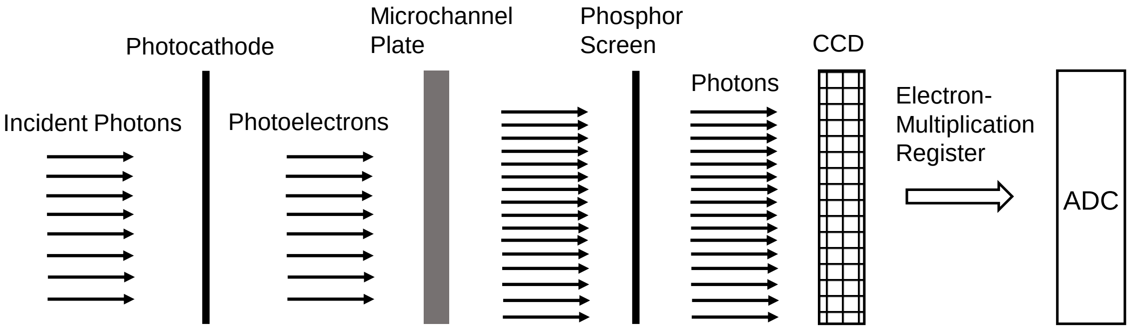

Figure 3.7: Schematic diagram of an electron-multiplier intensified CCD (emICCD) detector.

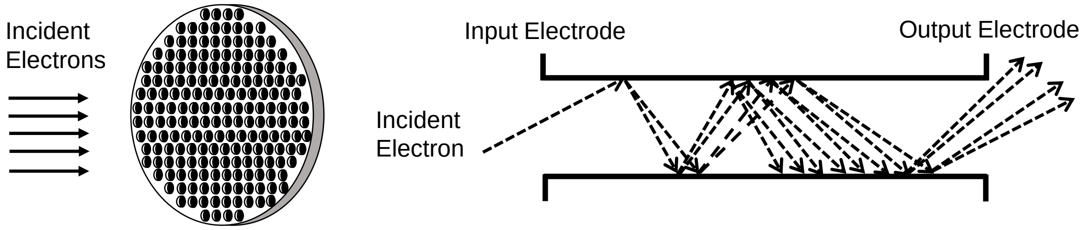

Figure 3.8: Schematic diagrams of a multichannel plate (MCP) (left) and an individual channel (right).

Figure 3.9 shows the quantum efficiency traces for a Gen II intensifier included in the emICCD camera utilized in this research work. The spectral performance was recorded in fast mode (gate width < 2 ns) and slow mode (100 ns). This Gen II has a blue enhanced photocathode (super blue, SB).

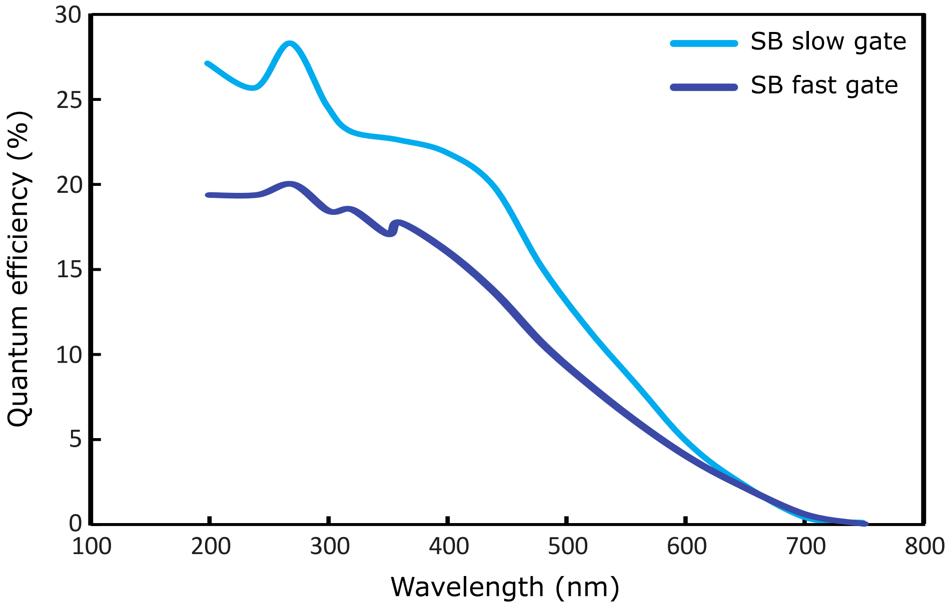

Figure 3.9: Quantum efficiency traces of super blue (SB) Gen II intensifier in slow and fast gate mode. The minimum gate width is < 2 ns in fast mode and 100 ns in slow mode. (Credit: Princeton Instruments)

3.2.2 Temporal Calibration

In order to optimize the plasma emission collection, it is critical to control the gate delay. By controlling the gate delay, the continuum emission can be excluded from the radiation that will be integrated by the spectrometer. As the plasma plume cools down after the hot plasma formation, more defined line emissions will be evident. Different elements and molecular species have different lifetimes and optimum emission times. Thus, temporal calibration shall consider not only the avoidance of continuum emission but also the optimum collection of emission lines for the species of interest.

Regarding μLIBS, the plasma plume lifetime is shorter than that of conventional (millijoule) LIBS and the decay of the continuum radiation is faster. Therefore, optimum gate delays are typically in the range of tens of nanoseconds for plasmas induced by microjoule pulses.

The first method to determine the optimum gate delay was performed using an avalanche photodetector (APD430A2, Thorlabs) to record the plasma emission with respect to the laser trigger output. This experiment takes into account the delay of the components involved in the LIBS apparatus to trigger the emICCD camera. These components include the optical cable, coaxial cable connected to the laser trigger output, and the laser trigger circuitry. Figure 3.10 shows the trigger signal and the plasma emission signal from the avalanche photodetector. Figure 3.11 shows the zoomed-in graph for clearer visualization.

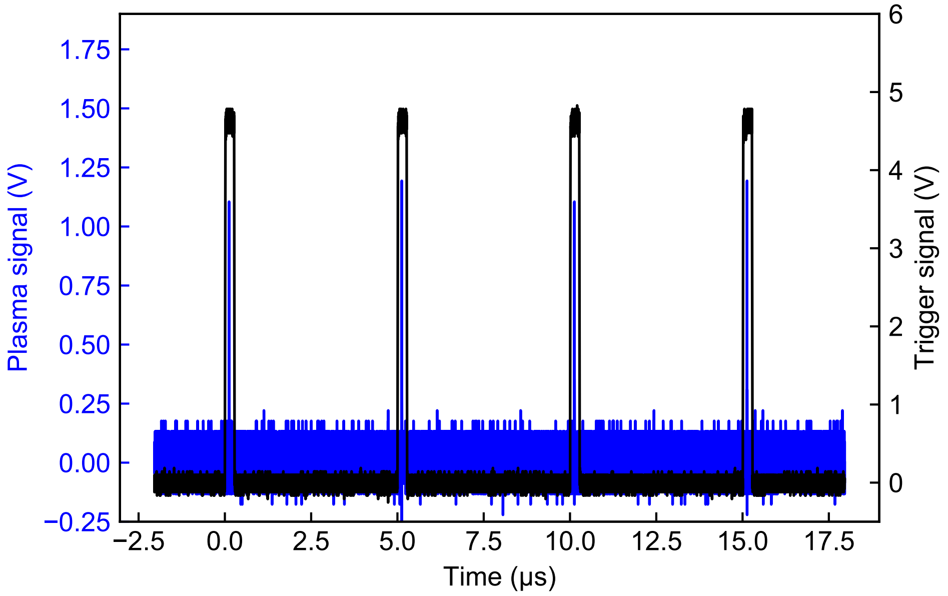

Figure 3.10: Temporal relationship between the plasma emission signal (blue) from the avalanche photodetector and the laser trigger signal (black).

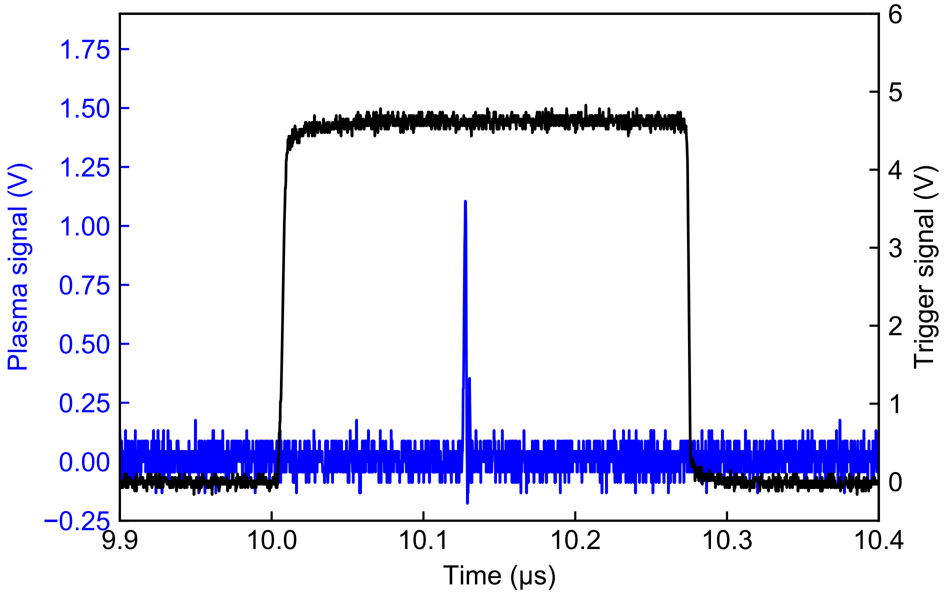

Figure 3.11: Zoomed-in graph from Figure 3.10 showing the temporal relationship between the plasma emission signal (blue) from the avalanche photodetector and the laser trigger output signal (black).

The second method was performed using the spectrometer, which included the SCT spectrograph and the emICCD detector. By varying the delay and using a fixed gate width of 5 ns, the spectral signal was recorded. Figure 3.12 shows a schematic overview that includes LIBS spectra for various delays (see insets), elapsed from the trigger signal of the spectrometer. For these measurements, the gate width was kept at 5 ns. This second method confirms the results from the first method, with an accuracy of ±1 ns.

Using both methods enabled the determination of the laser arrival, and the gate delay reported in this work represents the normalized gate delay from the laser arrival. The laser arrival was found to happen at 120.15 ± 0.1 ns. Therefore, to simplify the calculations, the gate delays were normalized for 120 ns.

3.2.3 LIBS Spectrum Analysis

After the LIBS signal is acquired, the spectrum may include dark signal, background noise, and emission lines. The dark signal shall be corrected prior to LIBS measurements. The

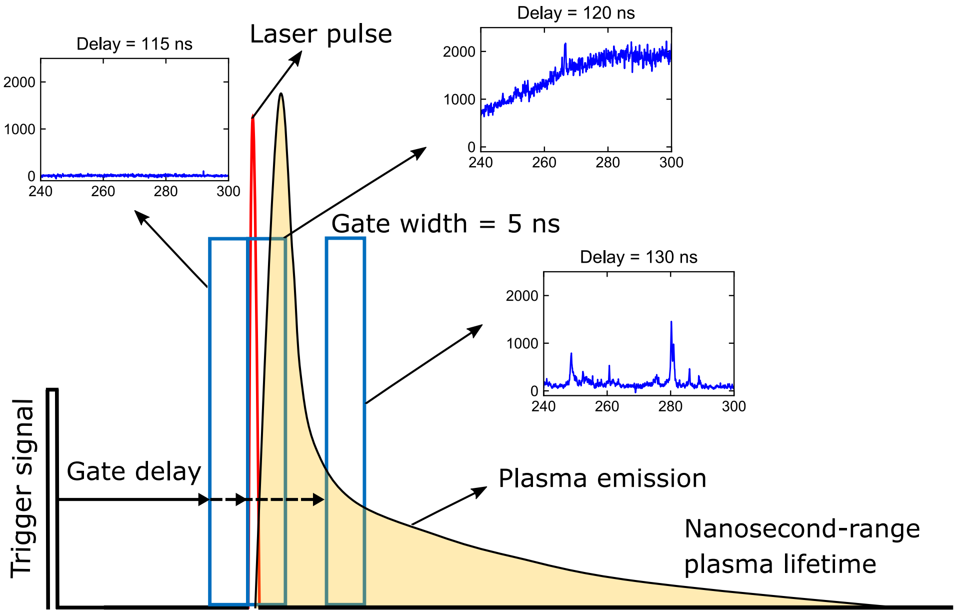

Figure 3.12: Schematic diagram of a plasma emission evolution, whose lifetime is typically in the nanosecond range for picosecond and ultrashort pulses. The nominal delay, from the spectrometer trigger signal, was varied. LIBS emissions, shown in the insets, were recorded at different delays, while maintaining the gate width of 5 ns. The abscissa and ordinate represent the wavelength (nm) and intensity (counts), respectively.

dark signal is considered the “fingerprint” of the ICCD detector, since it has a deterministic pattern, although its intensity may vary. Figure 3.13 shows a representative dark signal acquired before LIBS measurements. The acquisition of dark signal is performed in the absence of incident light, typically the ICCD detector deactivates its intensifier feature or the mechanical shutter remains closed. Once the dark signal is acquired, it can be removed from subsequent LIBS signals. In most acquisition software, this process is referred to as online background correction, and once the dark signal is recorded, it is removed during the LIBS measurements.

The background noise is a random signal, and it is influenced by various factors such as plasma emission conditions, plasma temperature, and ambient light. There are different methods available to correct the background in a LIBS spectrum, depending on the pattern of the background noise (e.g. linear or parabolic). Figure 3.14 illustrates the method to remove the background noise for a certain emission line.

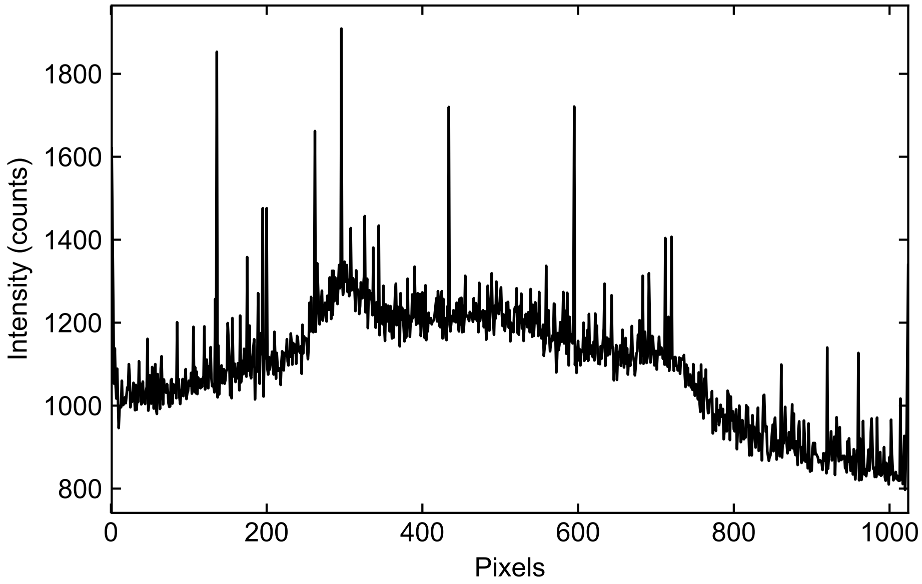

Figure 3.13: Dark signal taken at the absence of incoming light, when the intensifier is off. The dark signal is removed automatically from the final frame (spectrum) by the data acquisition software.

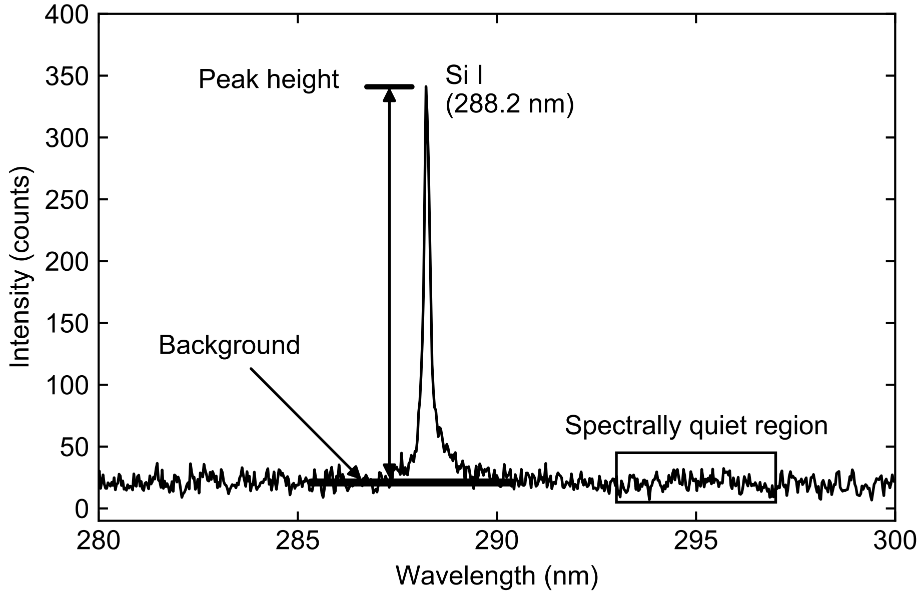

Figure 3.14: Definitions of the LIBS signal analysis, where the peak height is the single-channel LIBS signal intensity, the background is the background noise, and the spectrally quiet region is the noise region used to calculate the standard deviation.

Once the removal of the background noise is achieved, the peak height of the emission line can be determined. The SNR is a quantitative measure that defines the relative intensity between the emission line and the background noise. The general definition of SNR is given by

$$SNR = \frac{\sum_{i=1}^{N} I(\lambda_i)}{\sigma_b \sqrt{N}} \tag{3.4}$$

where $I(\lambda_i)$ is the background corrected intensity at the wavelength λ_i, i the channel index, N the number of channels over which the signal of interest is integrated, and σ_b the standard deviation of a spectrally quiet region away from the peak of interest. In this work, the peak height is considered, thus the intensity of one channel ($N = 1$) is used to determine the SNR. The simplified equation of the SNR, from Eq. 3.4, is as follows,

$$SNR = \frac{I_p}{\sigma_b} \tag{3.5}$$

where I_p is the background corrected peak height in one channel.

3.3 Laser Beam Characterization*

Measurement of the waist diameter of a focused Gaussian-beam at the $1/e^2$ intensity, also referred to as spot size, is key to determining the fluence in laser processing experiments. Fluence is an important parameter needed to calculate the amount of energy irradiated on a surface per unit area. Several reports in the literature have addressed the determination of Gaussian laser beam spot size [118–122], even for two-dimensional energy distribution [123]. A conventional method [120, 121], by analyzing single laser ablated spots for different laser pulse energies, was used to determine the cross-sectional area of a focused Gaussian beam.

Tungsten polycrystalline substrate (MTI Corp.) was used for the determination of the focused Gaussian beam area. The tungsten substrate had two sides polished, nominal purity of 99.95%, and nominal average surface roughness of less than 30 Å. The surface characteristics of the tungsten substrate provided a homogeneous surface to clearly measure the ablated

---

[*] The main results and content of this section have been published in R. Ledesma, F. Palmieri, J. Fitz-Gerald, J. Connell, NASA/TM-2018-219809 (2018) [117].

crater dimensions. The single-shot ablation was performed with a Nd:YVO_4 (Atlantic 20-355, EKSPLA) laser, which was operated at 355 nm with a nominal pulse duration of ∼10 ps. The laser beam was focused by an f-theta lens (S4LFT6062/075, Sill Optics), with an effective focal length of 250 mm, for a wavelength of 355 nm. The laser source operates at TEM_{00} beam mode before being focused by the f-theta lens. The laser system was assembled and calibrated by PhotoMachining Inc. The laser ablated spots were produced by moving the XY translational stage to expose a fresh surface after each single laser shot.

Figure 3.15 shows the SEM micrographs of the ablation craters for the pulse energies of 5 μJ, 15 μJ, and 30 μJ. The contours of the ablated craters exhibit smooth edges. This demonstrates that there is no thermal damage or redeposited material around the craters. As the laser energy increases, the shape of the ablated crater diverges from an ellipse. In addition, the absorption of the laser pulse at the center increases and produces an inner crater with a more consistent elliptical shape. The inner crater can be evidently observed in Figure 3.15c. The inner crater in Figure 3.15c also presents smooth edges. Above 15 μJ, the craters exhibit a deformation, which may be due to a distortion in the spatial laser energy distribution. The contours of ablated craters exhibit effects of astigmatism, which produces an elliptical shape. Different angles of divergence in two transverse directions cause astigmatism and elliptical beams [124–126]. Despite the drawback of the crater shapes ablated above 15 μJ, Figure 3.16 shows the closest elliptical fit to the crater contours. Figure 3.16a shows that the ablated crater was easily fit, however in Figures 3.16b and 3.16c, the elliptical fits became more challenging. From the elliptical fit (red contour) shown in Figure 3.16, consider D_1 as the minor diameter (green chord) and D_2 the major diameter (yellow chord).

Theoretically, the diameter of an ablated spot can be calculated by [127]:

$$D^2 = \frac{D_0^2}{2} \ln\left(\frac{E_p}{E_{th}}\right) \tag{3.6}$$

where D is the diameter of the ablated crater, D_0 the diameter at the Gaussian beam waist,

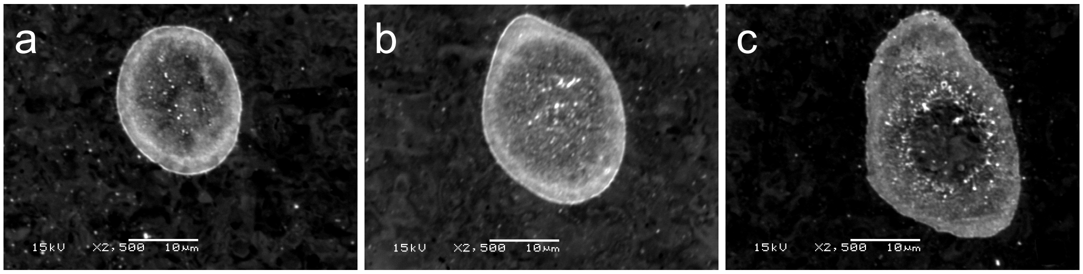

Figure 3.15: SEM micrographs of craters ablated at a) 5 µJ, b) 15 µJ, and c) 30 µJ.

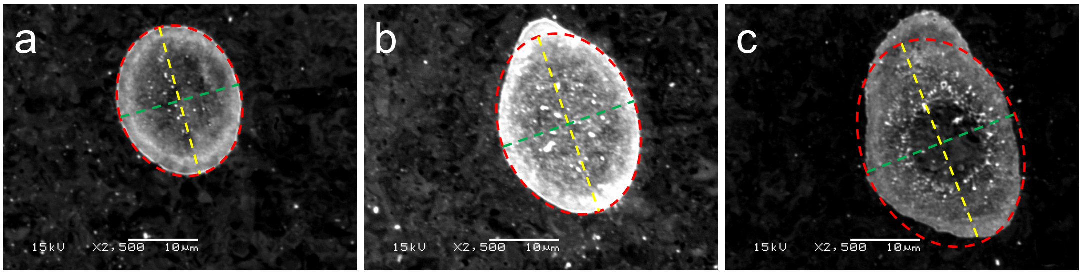

Figure 3.16: SEM micrographs with measurements of the elliptical fits to ablated crater contours, a) 5 µJ, b) 15 µJ, and c) 30 µJ. The green chord is the minor diameter, and the yellow chord is the major diameter.

E_p the irradiated pulse energy on the material, and E_{th} the ablation threshold of the material. The optical diameter D_0 represents $1/e^2$ of the intensity peak value. Within the circle of radius $w(z)$, 86% of the laser beam power is carried. At the waist, $z = 0$, the radius is $w(0) = D_0/2$.

From the SEM micrographs, it is clear that the Gaussian beam distribution is two-dimensional. Considering the minor diameter axis to be x and the major axis to be y, the two-dimensional Gaussian intensity (irradiance) at the beam waist is given by:

$$I(x,y) = I_0 \exp\left(-\frac{2x^2}{w_{0x}^2}\right) \exp\left(-\frac{2y^2}{w_{0y}^2}\right) \tag{3.7}$$

where I_0 is the peak intensity at the center of the beam and w_0 is the Gaussian beam radius, at which the intensity drops to $1/e^2$ of its peak intensity. The peak of the two-dimensional Gaussian function occurs when both radial positions, x and y, are on the center axis of the beam, i.e. $(x, y) = (0, 0)$.

Figure 3.17 shows the single-shot laser ablation threshold measurements of tungsten. Each data point is an average of three measurements, and the error bars indicate 1σ standard deviation. The logarithm of the ratio of E_p to E_{th} is linearly proportional to D^2. From the logarithmic fit to D_1, $E_{th,1} = 0.34$ µJ. Likewise, for D_2, $E_{th,2} = 0.8$ µJ. Since the threshold for D_1 is smaller than that for D_2, D_1 is used to determine the ablation threshold energy, E_{th}, needed to produce ablation damage on the tungsten substrate. Therefore, $D_0 = D_1 = 2w_{0x}$. Consequently, $E_{th} = E_{th,1} = 0.34$ µJ.

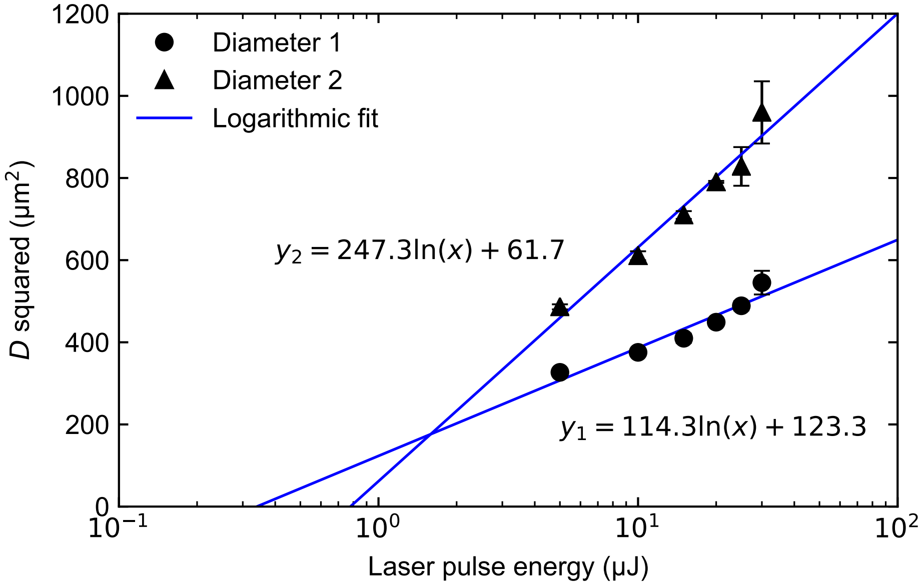

Figure 3.17: Single-shot laser ablation threshold measurements of tungsten. Diameter 1 is referred to as D_1, the minor diameter, and Diameter 2 is referred to as D_2, the major diameter.

Figure 3.18 shows the linear relationship between $\ln(E_p/E_{th})$ and D^2, according to Eq. 3.6. From Eq. 3.6, the one-dimensional optical diameter of the Gaussian beam can be determined when $D = D_0$, and consequently $E_p/E_{th} = e^2$. Considering the minor diameter, when $D_1 = D_{1,0} = 15.1$ µm, E_1 equals 2.5 µJ. Now, calculating for D_2 at $E_1 = 2.5$ µJ yields $D_2 = 16.8$ µm. The cross-sectional area A_e of the focused elliptical laser beam is calculated as:

$$A_e = \left(\frac{\pi}{4}\right) D_1 D_2 \tag{3.8}$$

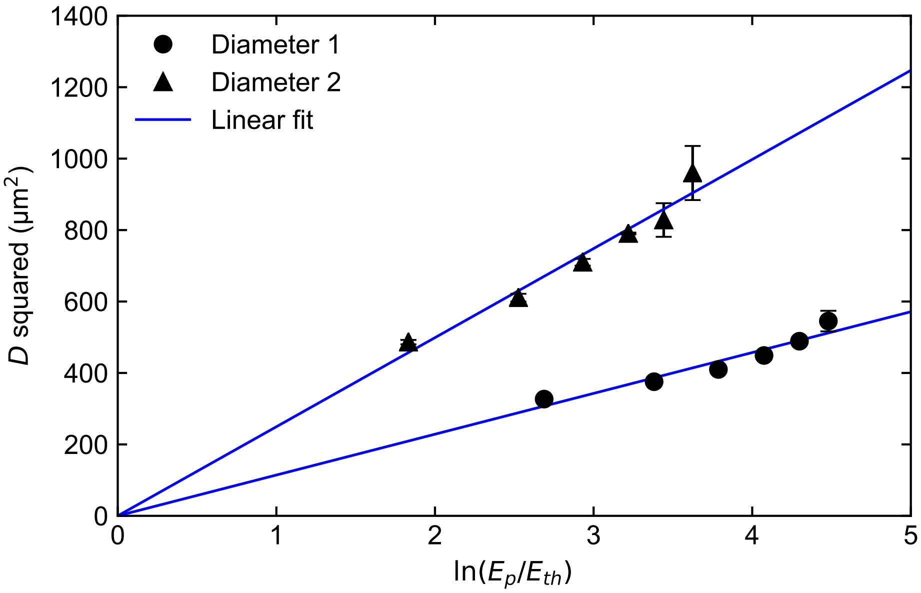

Figure 3.18: Linear relationship between $\ln(E_p/E_{th})$ and D^2, according to Eq. 3.6.

Therefore, the elliptical area A_e is 1.99×10^{-6} cm^2. By knowing the focused laser beam area, the average fluence F can be calculated as:

$$F = \frac{E_p}{A_e} \tag{3.9}$$

and the peak fluence as:

$$F_p = \frac{2E_p}{A_e} \tag{3.10}$$

Thus, the threshold fluence of the tungsten substrate using the ~10 ps focused laser beam is 0.17 J/cm^2. This fluence threshold is similar to other values found in literature [128–131].

Chapter 4

Correlation of OSEE with Failure Mode of CFRP Adherends*

Effective techniques for monitoring the pre-bonding surface conditions are crucial to obtain surfaces free from bond-degrading contaminants, e.g. mold release agents, which are widely used in CFRP manufacturing. In this work, OSEE was used prior to and after laser ablation to measure deposited levels of PDMS on CFRP. OSEE was also used to model the contamination layer thickness. After the specimens were adhesively bonded with a modified epoxy film adhesive, they were subjected to double cantilever beam (DCB) tests to investigate the hypothesis that surface contamination species and levels affect the fracture characteristics of adhesively bonded joints. This study relates OSEE photocurrent and the classification of the bond failure modes to their PDMS surface contamination levels prior to adhesive bonding. DCB test results show (1) that the region under the traces within the load and unloading boundaries consistently correlates with the bond strength and the probability of different failure modes, and (2) bond performance at fracture depends on the surface PDMS film thickness coating prior to laser surface treatment. The decrement in bond performance in this study correlates to the OSEE readings of contaminant levels on the adherend surfaces.

4.1 Introduction

A successful bond between adjacent structural components must fulfill the service requirements established by the manufacturer for any given structure. Typically, these requirements include

---

*The main results and content of this chapter have been published in R. Ledesma, W. Yost, F. Palmieri, D. Cataldo, J. Connell, Int. J. Adhes. Adhes. (2018) [132].

the ability to transfer loads across bonded regions under operating conditions during the useful lifetime. Operating conditions include exposure to environmental conditions (specifically large temperature and humidity changes and extreme weather conditions) as well as, for example, fuel spills or leakage of hydraulic and other fluids onto bond regions.

Success in establishing a bond between two surfaces depends on the conditions of the surfaces involved in the adhesive bonding process. Important components in the study of bonding are the cleanliness and chemical activation of the surface. The contaminant species and their respective concentrations are potential variables in determining bond quality. In this study, the following areas were examined: (1) surface cleanliness and techniques to measure surface concentrations of specific contaminants, and (2) surface ablation to remove contamination and to provide a chemically active surface to improve adhesive bonding.

Consistent with an absorption process that follows the Beer-Lambert law, contamination and adsorbates on surfaces change the photoelectron emission from the photoemitting target surface. Reactions between a surface and contaminants cause an alteration of the surface electron work function, which affects the efficiency of electron emission from the surface. Therefore, surface cleanliness affects photoemission based currents.

This investigation presents the capabilities of OSEE as a surface quality monitoring technique for CFRP by establishing a relationship between bond failure and OSEE readings of the surface contamination level. Each specimen set was contaminated with a measured surface concentration of PDMS, a major component of silicone based mold release agents, and then laser ablated. Silicones, even at low concentrations, are known to cause problems with adhesive bonding on CFRP surfaces [133]. Pre- and post-laser-ablation CFRP surfaces were examined with OSEE and other techniques. Mechanical testing, consistent with ASTM D5528-13 [133, 134], was performed by applying tensile load to the adhesively bonded CFRP specimens to determine failure modes, as per ASTM D5573-99 [135].

The sensitivity and accuracy of OSEE in distinguishing unfavorable CFRP surface conditions were also investigated. A separate set of specimens, cut from eight-ply CFRP and designed to fit the OSEE instrument measurement chamber, was used to establish the sensitivity of the OSEE measurement system to PDMS levels used in the DCB specimens. The failure modes in the DCB study were correlated to the results obtained with the OSEE technique. The effects of laser parameters on the OSEE signal response were analyzed when CFRP surfaces were laser treated using different scan speeds and average laser power levels.

4.2 Experimental

4.2.1 Materials

For the OSEE experiments, unidirectional CFRP panels (30.5 cm × 30.5 cm, 1.85 mm thick) were fabricated from eight plies of unidirectional Torayca P2302-19 (T800H/3900-2) prepreg. The curing process was performed in an autoclave at 177 °C for 2 hours under 690 kPa (6.9 atm). Release from the caul plate was achieved using Airtech A4000V release film, a fluorinated ethylene propylene (FEP) film, which was placed between the caul plate and the prepreg plies. Tool and caul surfaces were pre-treated with Zyvax WaterShield, a silicone-based mold release agent dispersed in water. The vacuum bagging setup and its constituents for the fabrication of unidirectional CFRP panels are shown in Figure 4.1. The laminates used for OSEE measurements were cut with a water jet into square specimens of 3.81 cm × 3.81 cm. For the fracture toughness test, 10-ply CFRP panels (30.5 cm × 30.5 cm, 2.08 mm thick) were prepared with the same procedure and machined by a water jet along the carbon fiber direction to produce samples of 2.5 cm × 24.1 cm.

4.2.2 Sample Contamination

Composite surfaces, except for the control surface, were contaminated prior to laser ablation. Contamination on CFRP samples was produced by spraying PDMS diluted with hexanes to various concentrations, leading to different layer thicknesses. Using witness silicon wafers (Si[100], 10.2 cm diameter), low (∼10 nm) and medium (∼60 nm) contamination levels were

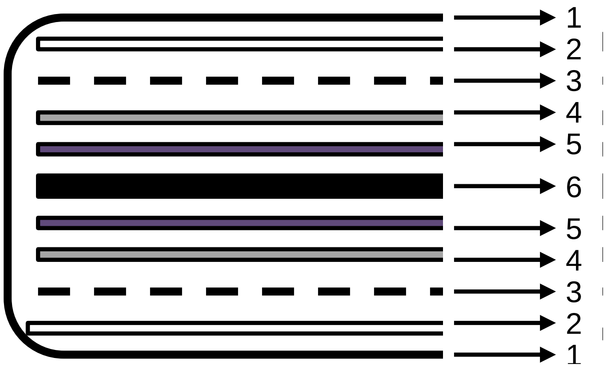

Figure 4.1: Vacuum bagging setup for the fabrication of unidirectional CFRP panels (both the eight-ply, used for OSEE data, and the 10-ply, used for fracture testing): 1. Low temperature bag material, 2. Breather fabric, Airtech Airweave N10, 3. Porous release layer, Airtech Release Ease 234 TFP, 4. Stainless steel caul plate, 5. FEP release film, Airtech A4000V, and 6. Plies of prepreg, Torayca P2302-19.

measured by using variable angle spectroscopic ellipsometry (VASE) [133, 136, 137] with a J.A. Woollam VB-400 control module and HS-190 scanning monochromator. Data were collected in the wavelength range from 370 nm to 900 nm with a 10 nm step size at different incident angles: 65°, 70°, and 75°. Using witness aluminum coupons, the film thickness of high contamination levels (∼1 µm) was determined by weight difference using an analytical balance with a nominal resolution of 0.01 mg. Both methods, VASE and weight difference, were used to infer the thickness of PDMS on CFRP, since its surface is rougher than that of Si wafers and may produce varied deposited quantities of PDMS based on the uneven topography of the composite surface.

4.2.3 Laser Ablation

Figure 4.2 shows the galvanometer-based optical scanner controlled laser system for ablation of CFRP samples. The galvanometer scanning unit controls the laser beam deflection along both X and Y axes. The stationary laser beam was guided to the surface by the galvanometer scanners, and focused by an f-theta lens, which provides a flat image field on the plane of interest.

During ablation, the CFRP sample is held stationary while the galvanometer unit scans the surface. The Coherent AVIA Nd:YAG laser system used for laser ablation was operated at 355 nm wavelength (3.5 eV photon energy). The pulse frequency was set to 80 kHz. The measured pulse width was 35 ns (FWHM). The average laser power was measured with a thermopile sensor (3A-SH) and a Nova II laser power meter from Ophir-Spiricon.

CFRP specimens were laser ablated with parallel lines, which were produced in the fiber orientation at 22.86 µm line pitch and 25.4 cm/s scan speed. The average radiant fluence F, defined as the energy irradiated on the surface per unit area, is calculated by

$$F = \frac{P_{\text{avg}}}{v_{\text{scan}} d_{\text{pitch}}} = \frac{E_p f}{v_{\text{scan}} d_{\text{pitch}}} \tag{4.1}$$

where P_{avg} is the average laser power, E_p the laser pulse energy, f the laser pulse frequency, v_{scan} the scan speed, and d_{pitch} the line pitch.

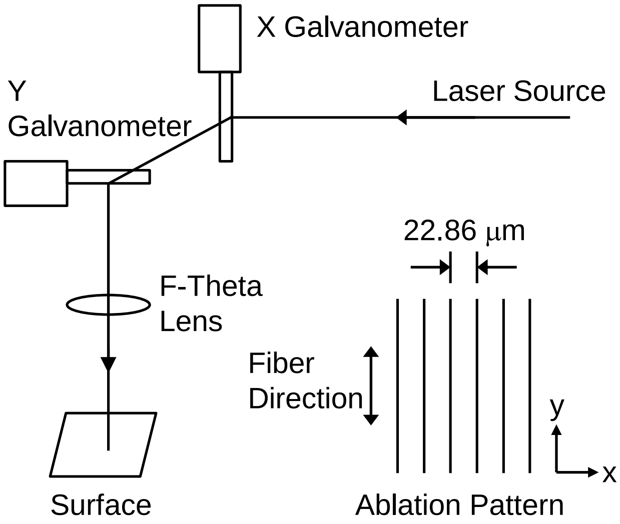

Figure 4.2: A galvanometer-based optical scanner and a laser source. The ablation pattern on the surface was produced along the fiber direction with a line pitch of 22.86 µm. The coordinate frame shows the directions of fibers and the ablation pattern.

4.2.4 Spectroscopy

One set of control CFRP surfaces was characterized for surface elemental components by X-ray photoelectron spectroscopy (XPS) before and after laser surface treatment. The XPS analysis was performed on a Surface Science Instruments SSX-100 spectrometer with a monochromatic Al K-alpha X-ray (1.486 keV photon energy) source. The analysis area was 800 µm x 800 µm.

Another set of CFRP samples (control and contaminated) was inspected after surface laser ablation to verify the presence of Si by energy-dispersive X-ray spectroscopy (EDS). The EDS analysis was conducted with an Oxford Instruments X-Max 50 mm^2 microanalysis system attached to a Hitachi scanning electron microscope (SEM). The acceleration voltage during the analysis was 5 kV.

4.2.5 OSEE

The OSEE apparatus used in this study was a prototype unit specifically designed for surface contamination research [113]. This OSEE unit applies a constant electric field for the electron collection process and a fixed UV light intensity source, which actively controls the intensity of the 185 nm line of the mercury spectrum. The regulation of photon flux and electric field tightly control the photoemission process for accurate contamination assessment during CFRP surface inspection.

The diagram of the OSEE inspection probe head [113] for CFRP surface inspection is shown in Figure 4.3. A LPMV lamp illuminated the surface under inspection with a measured photon flux of 49×10^{12} photons/s/cm^2. The photoelectrons emitted from the CFRP surface were drawn by the collector plate (a fused silica plate with the collector electrode coated onto the surface toward the specimen), which was positively biased at 200 V. The circular test area had a diameter of 2.54 cm. The distance from the collector to the target surface was 5.72 mm. The LPMV chamber was maintained in an argon environment. For each measurement, the test environment (the region between the collector plate and the specimen) was also purged with argon.

Two of the mercury lines that most contribute to the electron emission are 185 nm (6.7 eV photon energy) and 254 nm (4.9 eV photon energy). Photoemission studies, from previous tests on steel substrates, showed that the 185 nm emission line was typically responsible for 95% of the OSEE signal [21].

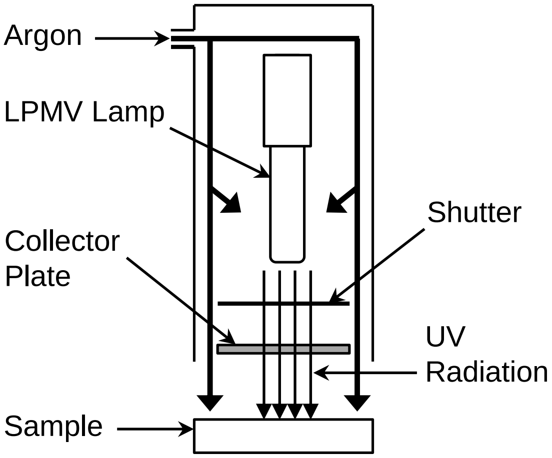

Figure 4.3: Diagram of the OSEE sensor and the target sample. The LPMV lamp chamber and the test area are purged with argon. The collector bias voltage is 200 V.

4.2.6 Adhesive Bonding

Within 48 hours of laser ablation, pairs of CFRP panels were bonded with the epoxy film adhesive Loctite EA 9696 Aero and cured for 1 hour in an autoclave at 121 °C under 680 kPa (6.8 atm). A 7.62 cm long, 12.5 µm thick film of FEP was included in the layup to create a precrack. Using a modification of ASTM D5528-13 [133, 134], samples were machined with a water jet into five specimens (2.5 cm × 24.1 cm) with notched ends for mounting directly on a clevis grip.

4.2.7 DCB testing

The DCB test method was used to mechanically test the bonded CFRP structures. With this method, the ends of a DCB specimen, as shown in Figure 4.4, are pulled apart causing crack propagation along the adhesive bond line and crack opening displacement parallel to the load direction. The bonded specimen included an initial crack a_0 of ∼70 mm; the exerted load P gradually opens the adhesively bonded specimen as the crack propagates.

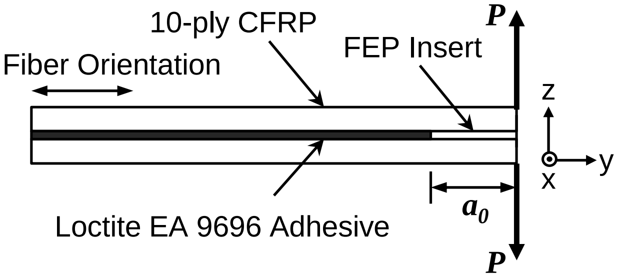

Figure 4.4: Diagram of a DCB specimen. The coordinate frame is aligned with that shown in Figure 4.2. The x-direction is out of the paper. The z-direction is the direction of the applied load P, while the y-direction is along the fiber orientation direction.

4.2.8 Failure Mode Analysis

Of the six potential failure modes described in ASTM D5573-99 [135], only the four presented in Figure 4.5 were observed in this study. Failure mode analysis was performed with the image processing and analysis software ImageJ [133, 138].

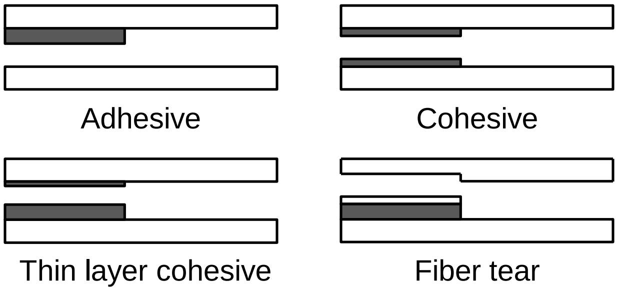

Figure 4.5: Failure modes for adhesively bonded fiber-reinforced polymers, showing the schematic diagrams of the various failure modes encountered in this study, according to ASTM D5573-99.

4.3 Results and Discussion

4.3.1 Laser Ablation

The ablation depth and width were measured from the ablated grooves produced at a scan speed of 25.4 cm/s. Figure 4.6 shows how the measurements were conducted. The grooves were ablated at 80 kHz, and considering the scan speed, there is a pulse overlap of ∼81% of the following pulse. In Figure 4.7, the ablation depth and width are shown as a function of the average laser power. The difference between ablation depth and width for the same average power was caused by the way in which power was absorbed around the focal point when striking the surface; more energy was channeled into width ablation than into depth ablation. Since the energy profile of the laser beam was essentially Gaussian, the surface ablation is nonuniform. Logarithm functions relating ablation depth with average laser power were fit to the depth and width data. From the logarithm formulae, the depth is y_d and the width y_w. From the width fitting equation, the ablation threshold is ∼53 mW (0.18 J/cm^2).

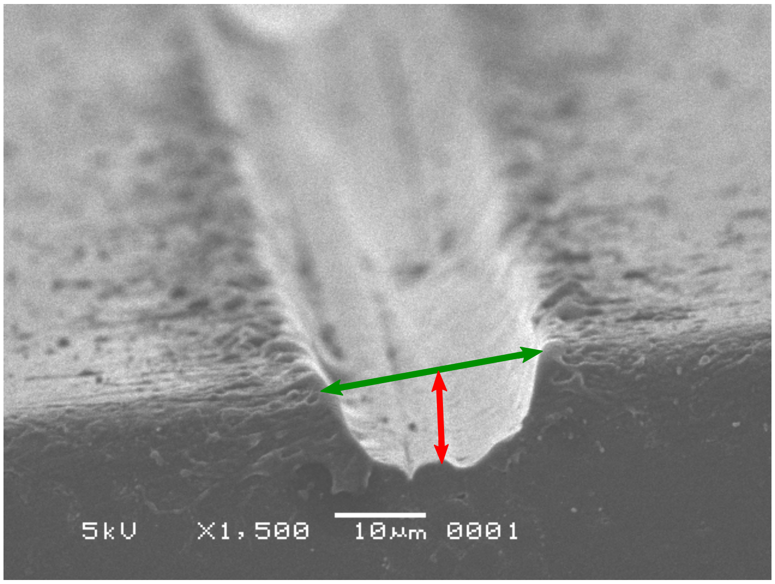

Figure 4.6: SEM micrograph of a cross-section of an ablated groove on a two-ply CFRP panel. The single groove was ablated at 600 mW and 80 kHz. The arrows indicate the method used to measure the width (green) and depth (red).

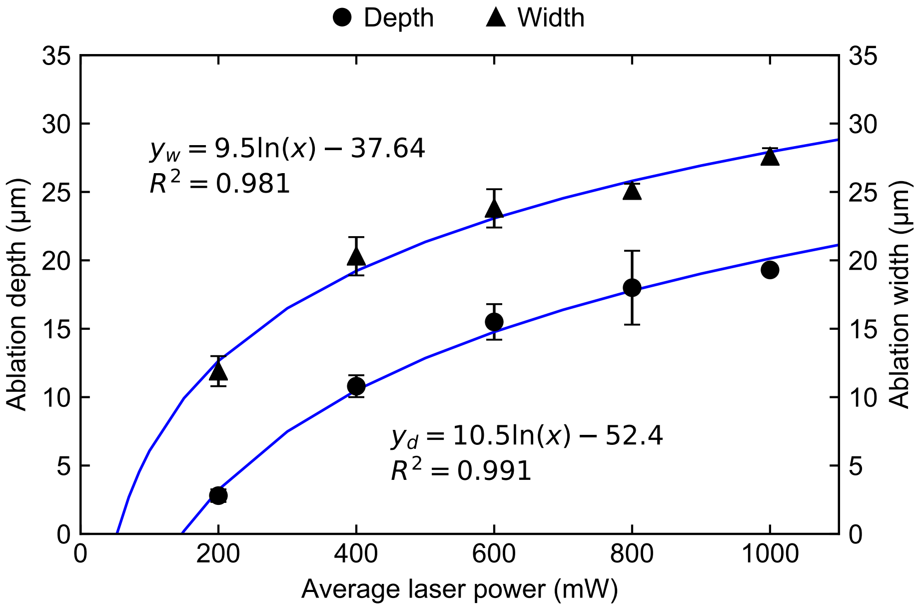

Figure 4.7: Ablation width and depth values as functions of the average laser power. The solid lines are the logarithmic fitting functions. The width fitting curve intersects the ablation threshold at ~53 mW.

4.3.2 PDMS Optical Absorption Properties

Eq. 2.2 was used to calculate the effective absorption coefficient of PDMS on the p-type silicon wafer from the plot shown in Figure 4.8. To exclude the effects of roughness and heterogeneity associated with CFRP surfaces, a p-type Si[100] wafer substrate was used to evaluate the absorption coefficient of PDMS on the OSEE photocurrent response. The photocurrent measurement for a Si[100] substrate was then based on the OSEE instrument's photocurrent readings under the same conditions used to measure photocurrents on the CFRP specimens. Under these conditions, the effective absorption coefficient of PDMS was 0.25 ± 0.04 nm^{-1}.

4.3.3 Photoemission from Laser Ablated CFRP Surfaces

Table 4.1 shows the surface characterization data, obtained by XPS, of control CFRP samples before and after laser ablation. The presence of silicone was detected by using the Si 2p peak

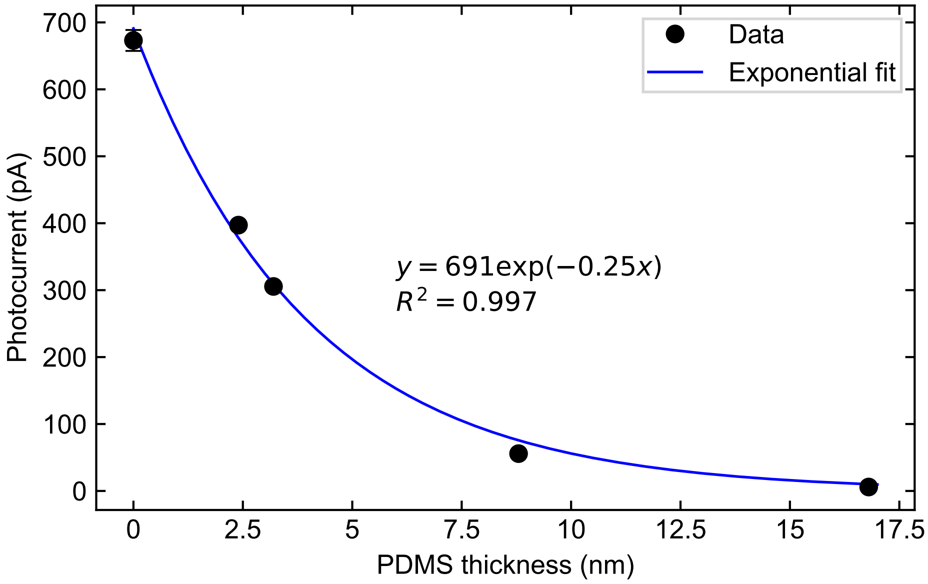

Figure 4.8: Photoemission response from p-type Si[100] substrate contaminated with PDMS. The exponential fit is in agreement with Eq. 2.2. The effective absorption coefficient is 0.25 ± 0.04 nm^{-1}.

that was located around the binding energy of 102.3 eV. After laser ablation, there was a decrease in the atomic percentage of Si from 3.4 to 1.2. This means that the silicone from the CFRP manufacturing was partly removed. Other undesirable contaminants, which were more easily removed by laser ablation, were F compounds from the FEP release film.

Table 4.1: XPS atomic percentage (at.%) for control CFRP surfaces before and after laser ablation.

	Atomic percentage (at.%)	
Element	Before laser ablation	After laser ablation
C 1s	46.4 ± 0.3	78.1 ± 0.8
F 1s	33.3 ± 0.6	0.4 ± 0.1
O 1s	13.9 ± 0.5	12.9 ± 0.8
Si 2p	3.4 ± 0.2	1.2 ± 0
N 1s	2.4 ± 0.3	6.1 ± 0.4
S 2p	0.7 ± 0	1.4 ± 0.2

Figure 4.9 summarizes the OSEE measurements for the CFRP coupons before and after laser ablation for different PDMS thicknesses. The average laser power chosen for the ablation process was 800 mW. The control sample was an untreated CFRP. The PDMS contaminated

samples yielded low OSEE responses. The high absorption by PDMS at 185 nm [139] was thought to be the contributing factor. The absence of electron emissivity of PDMS at 6.7 eV was well established and was not a factor, since PDMS has a photoelectron emission threshold of ~8.4 eV [140]. After the laser ablation treatment, the OSEE current increased significantly, which indicates a large change in the surface emission. Using the previously mentioned parameters for laser treatment, the resin surface layer in the CFRP structure was removed, and unbroken fibers were exposed, as shown in Figure 4.10. Therefore, both resin and contamination layers were laser ablated simultaneously. The exposure of carbon fibers can lead to fiber tear failure mode [6, 141]. Previous work has demonstrated that improved bond performance (~100% cohesive failure mode) has been achieved with minimal or negligible fiber exposure [141]. Since the carbon fibers are more electrically conductive and photoresponsive than the matrix resin [142], the exposure of the fibers favored higher OSEE response. Thus, the untreated and contaminated CFRP surfaces were differentiated from the laser ablated surfaces by the OSEE measurements. However, the CFRP samples that were contaminated with high PDMS levels of approximately 1 µm (1275 nm and 1347 nm) still yielded low OSEE current, owing to the incomplete removal of the PDMS layer. This was verified by EDS as shown in Table 4.2.

Table 4.2: EDS atomic percentage (at.%) of CFRP samples with remaining PDMS after laser ablation.

PDMS thickness (nm)	Atomic percentage (at.%) after laser ablation				
	C	O	N	S	Si
Control	84.71 ± 0.8	8.25 ± 0.5	5.68 ± 0.5	1.37 ± 0.06	0
6.9	84.98 ± 0.7	8.33 ± 0.007	5.59 ± 0.8	1.12 ± 0.2	0
9.1	85.07 ± 0.4	8.16 ± 0.6	5.77 ± 0.2	1.01 ± 0.04	0
49.8	86.37 ± 0.01	7.37 ± 0.4	4.81 ± 0.3	1.45 ± 0.15	0
69.7	85.84 ± 0.3	8.08 ± 0.14	5.03 ± 0.1	1.05 ± 0.1	0
1275	78.63 ± 0.44	11.59 ± 0.15	3.76 ± 0.1	0.79 ± 0.02	5.24 ± 0.7
1347	75.74 ± 3.2	12.24 ± 1.7	3.62 ± 0.7	0.75 ± 0.13	7.67 ± 2.4

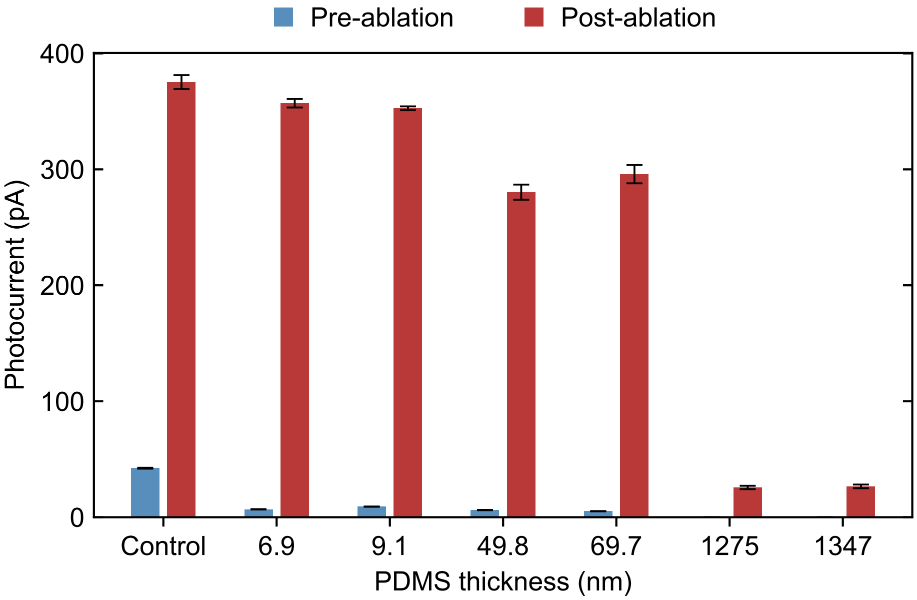

Figure 4.9: OSEE photocurrent measured at I_{th} for different PDMS thicknesses on CFRP surfaces.

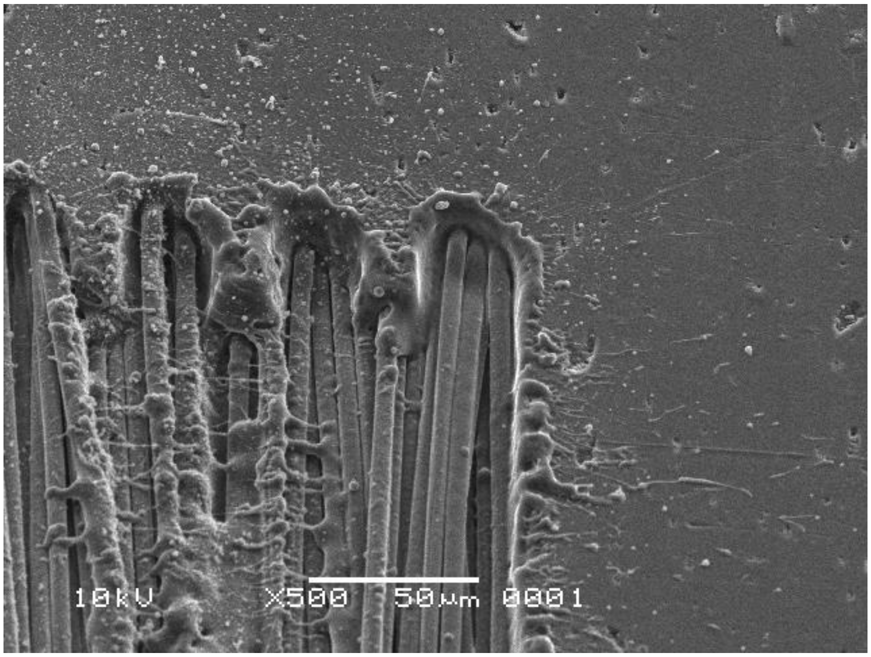

Figure 4.10: SEM micrograph of a CFRP surface laser ablated at 800 mW average power. Unbroken fibers are exposed underneath the resin surface layer.

4.3.4 Mechanical Testing and Failure Mode Analysis

Figure 4.11 shows the load-displacement traces after mechanical testing for select CFRP specimens, which are representative of their data set. The load-displacement traces were plotted for specimens with similar crack extensions of 7.89 ± 0.07 cm. As indicated by the curvature near the onset of failure (Figure 4.11), the DCB specimens did not undergo linear elastic fracture. The high toughness of the epoxy film adhesive (Loctite EA 9696 Aero) contributed to the nonlinear fracture behavior as more ductility was introduced. In addition, the bonded structures were comprised of nonlinear elastic materials, with polymeric interfaces and composite bulk substrates. Thus, linear-elastic fracture mechanics (LEFM) methods could not be applied reliably to calculate the fracture toughness. Instead, a qualitative comparison of the regions under the traces within the load and unloading boundaries indicates decreasing bond performance with increasing PDMS thickness on the CFRP surfaces prior to laser ablation and bonding. As the crack propagated along the bond line, various failure modes were observed.

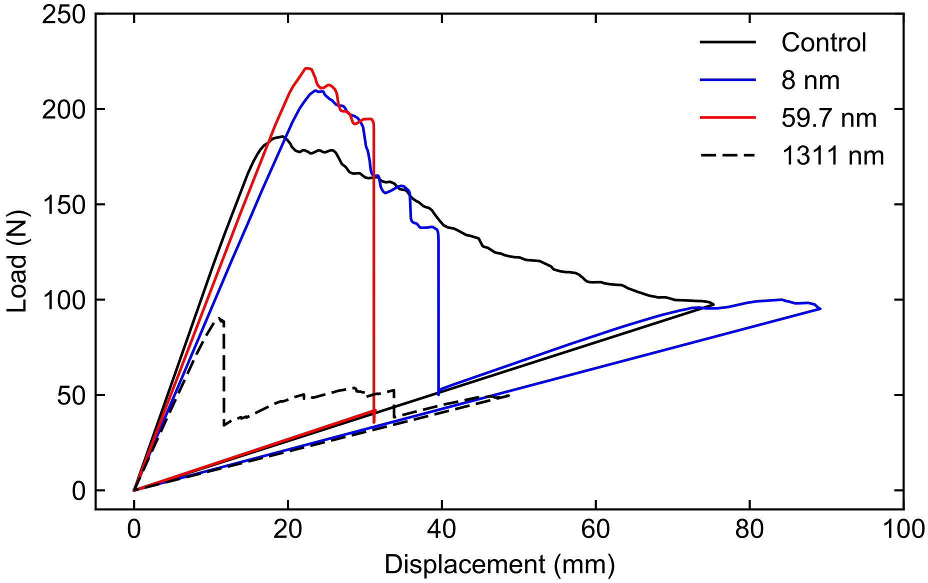

Figure 4.11: Load versus displacement traces for select DCB specimens. The CFRP adherends were contaminated with PDMS coatings and laser treated prior to adhesive bonding.

Figure 4.12 shows the photocurrent obtained after laser surface treatment, and before adhesive bonding, plotted against the cohesive failure mode calculated from the DCB tests. A higher value of photocurrent signifies that bonding is improved between the adhesive and the adherends. This is likely due to the removal of more contaminant and a consequent increase in available surface area for bonding. The OSEE photocurrent increased as contaminant levels decreased, and the target surface was chemically activated after laser ablation, as shown in Figure 4.9. The data suggest a relationship between the cohesive failure mode of the fracture surfaces and the OSEE photocurrent from target surfaces prior to adhesive bonding.

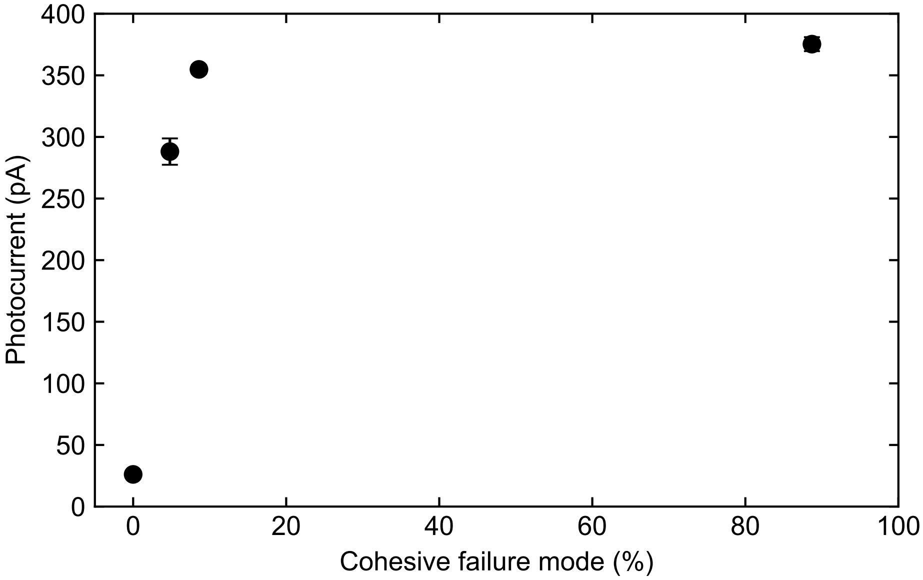

Figure 4.12: Photocurrent versus cohesive failure mode. The failure modes were analyzed after DCB testing using ImageJ and confirmed by visual inspection.

The failure modes depicted in Figure 4.5 were assessed by visual inspection and image analysis software. Figure 4.13 shows the surfaces of the failure modes obtained by using the image software ImageJ. Each image was constructed by folding the top beam about the fiber orientation axis, and placing it edge-to-edge with the bottom beam. The center line in each image denotes the edge-to-edge placement. In this alignment, the top and bottom fracture surfaces are both visible. The contoured character of the fracture surface shows up in opposite relief on opposite sides of the center line. Figure 4.13a shows a specimen that presented adhesive failure due to contamination residue, causing a poor bond between the adhesive and specimen surface. When the surface is properly treated, the bond between the adhesive and the specimen surface is stronger than the adhesive bond line. Thus, the fracture surface undergoes cohesive failure, as shown in Figure 4.13b. Figure 4.13c shows the results of a thin layer cohesive failure, in which thick adhesive layers were present on one substrate surface, and thin layers on the other. When the top fiber layer of the CFRP substrate fails, delamination occurs, as shown in Figure 4.13d. Fiber tear failures may occur from a variety of possible surface treatment techniques, such as sanding, grit blasting, and laser treatment, as well as crack propagation dynamics. Depending on the ablation energy, the laser treatment process may expose some carbon fibers in the top ply, to which the adhesive would directly bond, as shown in Figure 4.10.

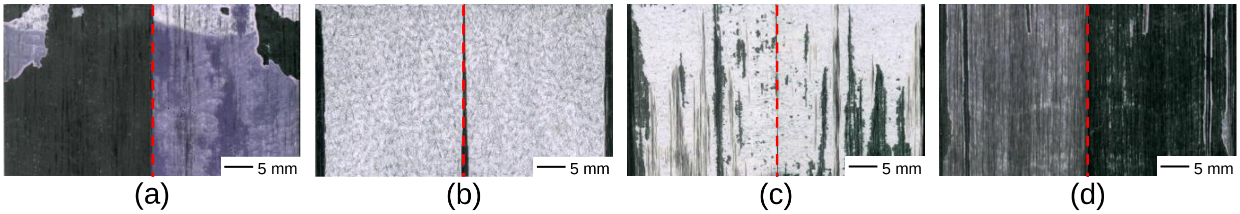

Figure 4.13: DCB failure surfaces, placed edge-to-edge, (top on the left; bottom on the right, as shown by the center line) for CFRP with predominantly a) adhesive, b) cohesive, c) thin layer cohesive, and d) fiber tear modes.

Since cohesive and thin layer cohesive failure modes are preferred over adhesive or other failure modes, Figure 4.14 displays the percentages of cohesive and thin layer cohesive failure modes from the DCB tests as a function of the PDMS molecular areal number density, which was deposited before laser ablation. For comparison, in the same graph the photocurrent is shown as a function of the PDMS areal number density. The CFRP surfaces were laser treated with 800 mW average power prior to the adhesive bonding. Five bonded joints were mechanically tested for each surface condition. The results reveal more clearly the effects of the silicone-based contamination, even after laser ablation, showing predominantly low percentages of cohesive and thin layer cohesive failures. Large differences in failure mode percentages were reported between the control surface, and those with low PDMS levels. As shown in Figure 4.9, the OSEE photocurrent of the control CFRP was slightly higher than that of the low PDMS areal number densities. The uncontaminated control sample produced cohesive failure of ∼89%, in contrast to the low percentage of cohesive failure (< 10%) for the contaminated samples prior to laser ablation. The poor bonding performance in previously contaminated surfaces was also observed, even after the laser ablation process was applied. The poor performance may imply that PDMS and similar compounds remained on the surface, because they have low absorption for wavelengths above 200 nm [139]. This may affect their removal by laser ablation at 355 nm, although the mechanisms that discourage removal are not entirely clear. Higher OSEE photocurrents indicate higher probability of cohesive failures, since larger photocurrent implies less density of surface contamination.

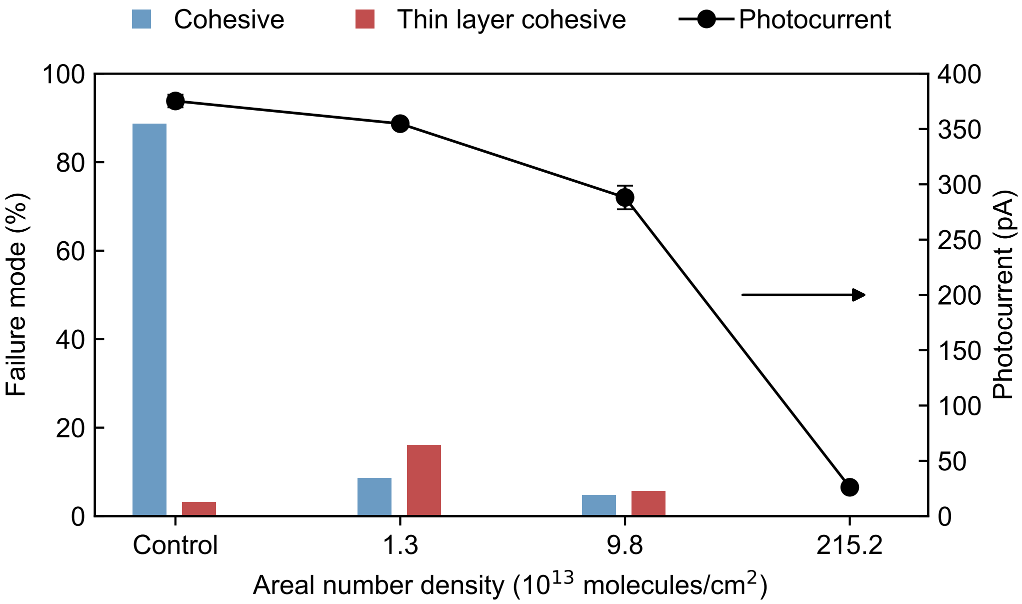

Figure 4.14: Cohesive and thin layer cohesive failures modes (left ordinate) and the photocurrent (right ordinate) as functions of the PDMS areal number density. The CFRP surfaces were contaminated with different PDMS concentrations and laser treated prior to bonding. The failure modes were determined after DCB testing.

Table 4.3 summarizes the results of measurements from photoemission (pre-ablation and post-ablation) against contaminant film thickness. The PDMS film thickness was varied by adjusting the concentration of PDMS in the solvent, which was thermally treated to completely evaporate remaining hexanes from the surface prior to the photocurrent measurements. The three levels of PDMS contaminants were chosen to provide guidance for future investigations into effects of contaminant levels on adhesive bond strength in CFRP-based structures.

Table 4.3: Relationship between PDMS thickness and photocurrent I_{th}.

Areal number density (10^{13} molecules/cm^2)	Film thickness (nm)	Film areal density (μg/cm^2)	Pre-ablation I_{th} (pA)	Post-ablation I_{th} (pA)
Control	0	0	42.3 ± 0.4	375.3 ± 5.7
1.3	8 ± 1.6	0.77 ± 0.15	8 ± 1.3	354.8 ± 3.5
9.8	59.7 ± 14.1	5.8 ± 1.4	5.7 ± 0.6	288.1 ± 10.7
215.2	1311 ± 51	126.5 ± 5	-	26.2 ± 1.5

4.3.5 CFRP Surface Topography

Laser parameters used for treatment of CFRP surfaces not only change the surface chemistry but also the surface morphology. Different laser powers created variations in selective patterns and topographical modifications on the surface prior to bonding. The parameters analyzed in this study were the laser power levels and the scan speed. The average laser power exposures were 100 mW, 300 mW, and 800 mW, which have been previously used for laser surface treatment [133, 143].

To check the effects of delayed measurements on CFRP material after exposure, control CFRP samples were tested within 24 hours of laser ablation and again after 1 week. The target samples were stored for 1 week in a desiccator with air at room temperature, normal atmospheric pressure, and at 21.8 ± 5.8 % relative humidity. Figure 4.15 shows the effect of different laser power levels on the OSEE photocurrent. Figure 4.16 shows the OSEE photocurrent for surfaces that were laser ablated at 800 mW at three different scan speeds (25.4 cm/s, 50.8 cm/s, and 101.6 cm/s). For the measurements taken within 24 hours, the photocurrent was similar for the three different laser average powers. After 1 week, there was a decrease in the photocurrent. This decrement in photocurrent may have been caused by surface contamination by organic or inorganic compounds from the air, oxidation growth on the surface, and passivation of active chemical species initially formed.

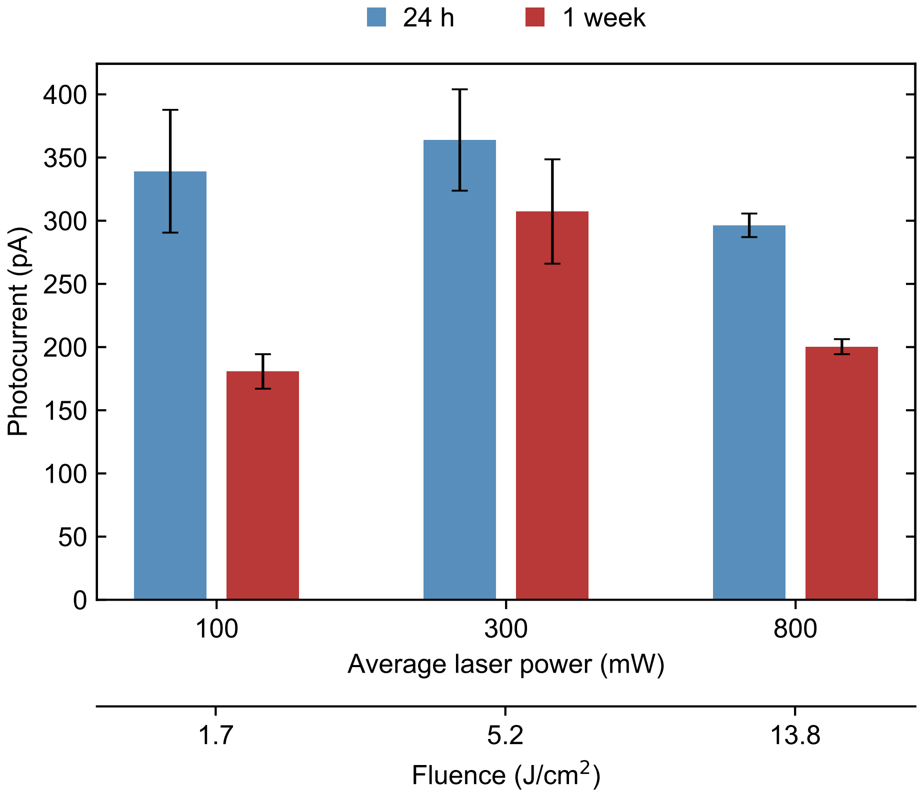

Figure 4.15: OSEE readings for CFRP samples laser ablated at different laser power levels within 24 hours and again after 1 week.

The particles adsorbed on the surface were held by weak physical bonds, in comparison to chemical bonds. These particles can alter the OSEE photocurrent measured. The London-van der Waals equation describes the adhesion force between a spherical particle and a flat surface,

$$F_{\mathrm{LW}} = \frac{Ar}{6{d_s}^2} \tag{4.2}$$

where A is the Hamaker coefficient, which depends on the particle and surface composition, r the radius of a spherical particle, and d_s the distance of separation. Theoretically, the oxidation of the surface is produced by adsorption of oxygen on the surface that bonds with the valence electrons of the surface, and thus produces carbonyl, hydroxyl, and epoxide functional groups. The oxidation films on the surface affect the work function of the material. The oxidation of species on the CFRP surface is nonuniform due to the roughness and

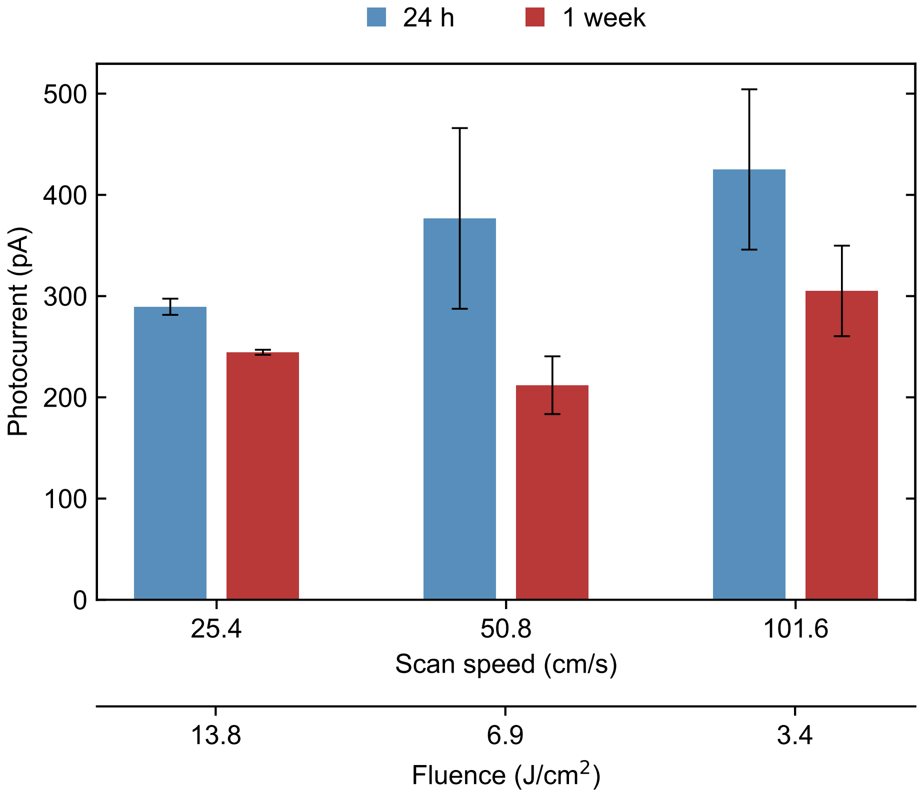

Figure 4.16: OSEE readings for CFRP samples laser ablated at 800 mW at different scan speeds within 24 hours and again after 1 week.

heterogeneity of the laser ablated composite material. For the CFRP surfaces freshly laser ablated, the surface becomes rougher as the radiant fluence increases. As surfaces become rougher, both the UV light scattering on the surface and the increase in electron emission angle affect the photoelectron emission [64].

The CFRP surface topography was analyzed with an FRT MicroProf optical profilometer. The average roughness was determined with the phase correct filter according to ISO 11562 [144]. Figure 4.17 depicts the relationship between the OSEE photocurrent and the average roughness for different CFRP surface conditions after laser ablation. As the roughness increases, the photocurrent increases to a certain level, followed by a photoemission decrease at the 13.8 J/cm^2 (800 mW). This change in the surface morphology affects the photocurrent. Possible mechanisms for this photocurrent emission change may include the increase in exposed surface due to the increase in surface roughness, and surface chemistry initiated by the UV exposure from the OSEE apparatus. Kinetics of photoelectrons may also play a role in the photocurrent variations. Despite this, photocurrent differences due to contamination level within each category were observed. However, ablation exposure in photocurrent interpretation to deduce contaminant level must be considered.

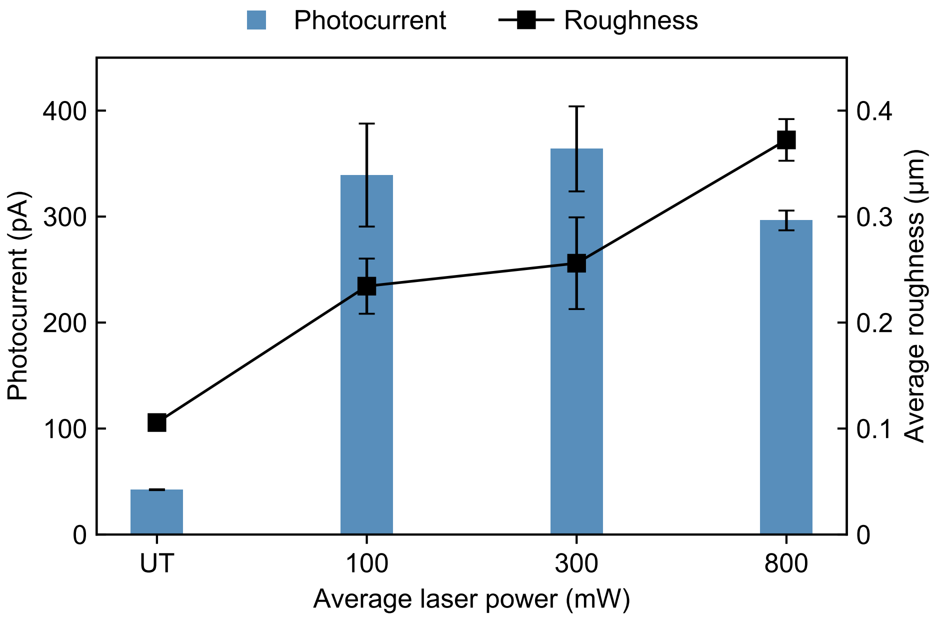

Figure 4.17: Relationship between OSEE photocurrent and average roughness as a function of the average laser power. The untreated (UT) CFRP is compared with laser ablated CFRP surfaces. The bar graph represents the photocurrent (left ordinate), while the solid squares represents the average roughness (right ordinate).

4.4 Conclusions

OSEE provided a very sensitive technique that was clearly able to detect small amounts of silicone surface contamination, even mono-molecular layer segments partially covering a surface. OSEE photocurrent measurements gave an effective absorption coefficient for a PDMS contamination layer, as confirmed by measurements with known contamination thicknesses on a Si[100] substrate. Furthermore, with OSEE measurements, it was possible to identify whether and to what degree a CFRP surface was laser ablated. The data suggest that increases in OSEE photocurrent with increasing ablation are due to the exposed carbon fibers near the surface. For the material system studied, the qualitative analysis of the regions under the traces within the load and unloading boundaries correlated with the pre-bond OSEE photocurrent intensities. This correlation indicates that the OSEE technique may be used to predict bond performance. The correlation of OSEE photocurrent with failure modes obtained from DCB tests supports the hypothesis that surface contamination species and concentrations alter fracture characteristics of adhesively bonded joints. It was clear that OSEE photocurrent levels were also affected by surface roughness, however effects of surface roughness on bonding were not investigated when surface contamination was also a factor. Based on this study, it may be possible to predict bond performance by measuring the contaminant concentration on adherend surfaces prior to applying the adhesive.

Chapter 5

Surface Characterization of CFRP Composites by Picosecond LIBS*

In this chapter, the focus is to advance the LIBS technique by using pulse energies below 100 μJ (μLIBS) for the detection of low levels of silicone contaminants in CFRP composites. The aim of using pulse energies below 100 μJ was two-fold: (1) decrease the amount of ablated material necessary to induce a plasma plume, thus increasing surface sensitivity, and (2) improve the LOD by enhancement of the line to continuum emission ratio. Various CFRP surface conditions were investigated by LIBS using ∼10 ps, 355 nm laser pulses with pulse energies below 30 μJ. Time-resolved analysis was conducted to optimize the gate delay and gate width for the detection of the C I emission line at 247.9 nm to monitor the epoxy resin matrix of CFRP composites and the Si I emission line at 288.2 nm for detection of silicone contaminants in CFRP. CFRP surfaces were coated with PDMS to investigate the hypothesis that high surface sensitivity is achieved by picosecond μLIBS to detect thin layers of silicone contamination on polymer matrix composites with both minimal ablation damage and thermal stress. The presence of PDMS is studied by inspecting the Si I emission lines at 251.6 nm and 288.2 nm. The measured PDMS areal densities range from 0.15 to 2 $\mu g/cm^2$. LIBS measurements were performed before and after laser surface ablation. The results demonstrate the successful detection of PDMS thin layers on CFRP using picosecond μLIBS.

---

*The main results and content of this chapter have been published in R. Ledesma, F. Palmieri, J. Connell, W. Yost, J. Fitz-Gerald, Spectrochim. Acta, Part B (2017) [145].

5.1 Introduction

LIBS was investigated for monitoring the presence of silicone contamination on CFRP materials. Microjoule picosecond laser pulses can produce high peak power levels that can surpass the optical breakdown thresholds of many materials. The aim of this work is to demonstrate that single UV picosecond pulses can be used for LIBS analysis of silicone contaminants on CFRP. The LIBS measurements were conducted with single laser shots on previously untested, i.e. "fresh", surfaces at low pulse energies. In this study, CFRP surfaces were contaminated with PDMS in a controlled fashion to produce thin contamination layers. The panels contaminated with PDMS were analyzed by LIBS prior to and after laser ablation to determine the ability of the laser treatment process to remove silicone as well as the ability of LIBS to detect very low levels of silicone.

5.2 Experimental

5.2.1 Materials

The fabrication process of the epoxy composites is the same as in Section 4.2.1. For convenience, this section describes again the process herein. Unidirectional carbon fiber reinforced epoxy panels (30.5 cm × 30.5 cm) were fabricated from eight plies of unidirectional Torayca P2302-19 (T800H/3900-2) prepreg. The prepreg was cured in an autoclave at 177 °C and 690 kPa. Release from the caul plate was achieved using Airtech A4000V release film, a FEP film. Tool and caul surfaces were pre-treated with Zyvax WaterShield, a silicone-based mold release agent dispersed in water. For LIBS measurements, the laminates were cut with a water jet into square samples of 1.27 cm × 1.27 cm.

XPS was performed on a Surface Science Instruments SSX-100 spectrometer with a monochromatic Al K-alpha X-ray (1.486 keV photon energy) source. The spot size was 800 µm × 800 µm.

5.2.2 Sample Contamination

Contamination on CFRP samples was produced by spraying PDMS diluted with hexanes to various concentrations, leading to different layer thicknesses. The PDMS coated samples were dried at 100 °C for 1 hour. Using witness p-type Si[100] wafers, PDMS thicknesses were measured by using VASE using a J.A. Woollam VB-400 control module and HS-190 scanning monochromator. Data were collected in the wavelength range from 370 nm to 900 nm with a 10 nm step size at three incident angles: 65°, 70°, and 75°. From these measurements, the thickness of PDMS on the CFRP surfaces was inferred.

5.2.3 Laser Ablation

Laser ablation was performed with a Nd:YVO_4 laser system (Atlantic 20-355, EKSPLA) operated at 355 nm with a nominal pulse duration of ∼10 ps, 80 mW average power, and 400 kHz pulse frequency. The calculated average photon flux of the focused laser beam was 7.17×10^{22} photons/s/cm^2. The average laser power was measured with a thermopile sensor (30A-BB-18, Ophir-Spiricon) and a laser power meter (Nova II, Ophir-Spiricon). During ablation, the CFRP sample was held stationary while the galvanometer unit scanned the composite surface. CFRP specimens were laser ablated with parallel lines, which were produced in the fiber orientation at 12.7 μm line pitch and 25.4 cm/s scan speed.

5.2.4 Surface Morphology

Depth measurements of LIBS craters produced with single shots were performed with an optical surface profiler (NewView 6000, Zygo) equipped with a 20X Mirau objective and a 1X zoom lens. CFRP surfaces were coated with Pd-Au for surface morphology analysis using a JEOL JSM-5600 scanning electron microscope operated at an accelerating voltage of 15 kV.

5.2.5 LIBS

The schematic diagram of the LIBS system is shown in Figure 5.1. The Nd:YVO_4 (Atlantic 20-355, EKSPLA) laser was operated at 355 nm with a nominal pulse duration of ∼10 ps. The laser beam was focused by an f-theta lens (S4LFT6062/075, Sill Optics) for a wavelength of 355 nm and with an effective focal length of 250 mm. The LIBS emission was measured using a 328 mm, f/4.6 SCT spectrograph (IsoPlane SCT 320, Princeton Instruments). The spectral response was recorded using an emICCD camera (PI-MAX4: 1024 EMB, Princeton Instruments). The plasma emission was collected with a collimator and guided to the spectrograph via an optical cable with 19, 200 µm fibers. A grating with 1200 grooves/mm, blazed at 300 nm, was used for all the experiments. The slit width was kept at 10 µm. The emICCD camera was externally triggered by the laser trigger output.

The LIBS spectra were generated by averaging 15 frames of 10 single laser shots. The target surface was moved with the XY stage after each single shot to expose a fresh surface for each incident pulse. The 10 single laser shots were accumulated on the CCD sensor.

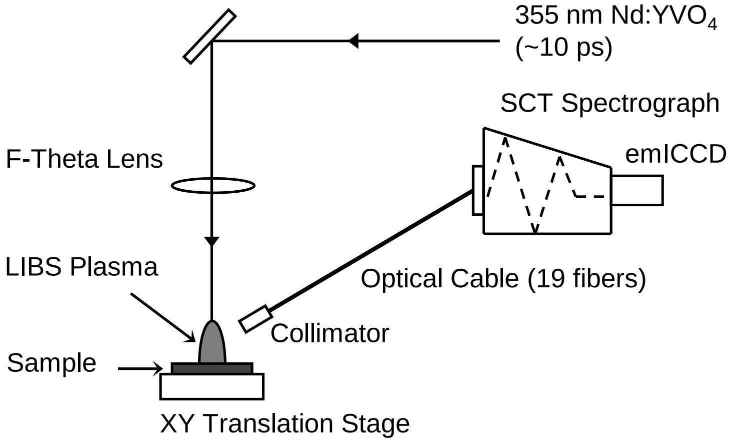

Figure 5.1: Schematic diagram of the LIBS system for the detection of contaminants on CFRP.

5.3 Results and Discussion

5.3.1 Surface Morphology

The ablation threshold for ablation depth per pulse is calculated by single-shot ablated craters with [146],

$$d_a = \delta \ln \left(\frac{E_p}{E_{th}} \right) \tag{5.1}$$

where d_a is the single-shot ablation depth, δ the effective optical penetration depth, E_p the laser pulse energy, and E_{th} the threshold energy for laser ablation.

Figure 5.2 shows the linear relationship between the single-shot ablation depth and the logarithm of the laser pulse energy. The error bars indicate 1σ standard deviation. The slope of the logarithmic fit in Eq. 5.1 yields $\delta = 0.33 \pm 0.07$ µm. The single laser shots ablated only the top layer of epoxy resin without interacting with the carbon fibers. Therefore, the threshold energy of the matrix epoxy resin calculated for a laser pulse duration of ~10 ps focused on CFRP is 2.4 µJ (1.21 J/cm^2).

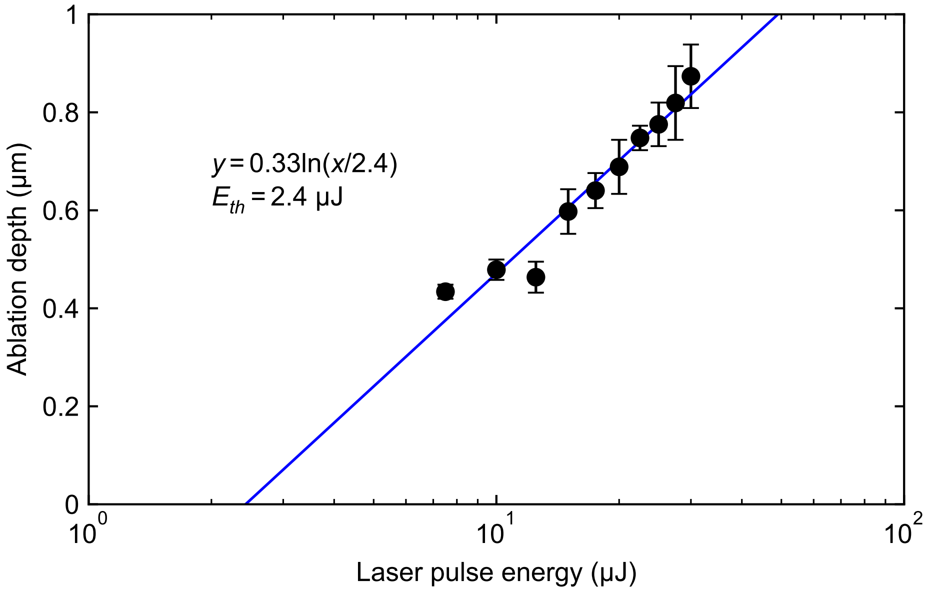

Figure 5.2: Single-shot ablation depth measurements of CFRP. The solid line represents the logarithmic fit according to Eq. 5.1, which yields an effective optical penetration depth of $\delta = 0.33 \pm 0.07$ µm and an ablation threshold of E_{th}=2.4 µJ.

Figure 5.3 shows the SEM micrographs of the craters produced on CFRP using single laser shots. The craters show no melted or redeposited material around the craters. As the pulse energy increases above 15 μJ, an inner crater starts forming owing to the increasing energy absorption of the material in the same direction of the laser beam. In addition, the crater deepens faster than it widens. In contrast to the crater contour, the inner crater has a circular shape. Similar to the external major crater, the inner crater does not exhibit melted or redeposited material around its contour. The outer crater exhibits a shallow and smooth structure likely owing to "gentle" ablation produced by two-photon absorption. In contrast, the formation of the inner crater, deeper in comparison to the outer crater, might be due to higher-order transition (three or greater photon absorption), which produces "strong" ablation effects as the laser intensity increases.

In all the LIBS measurements, the pulses do not interact with the carbon fibers underneath the resin surface layer, as shown in the SEM micrographs.

5.3.2 SNR Analysis

The SNR is a quantitative measure that defines the relative intensity between the LIBS signal and the noise. The SNR is calculated as,

$$SNR = \frac{I_p}{\sigma_b} \tag{5.2}$$

where I_p is the background-corrected height of the peak of interest, and σ_b is the standard deviation of a background-corrected spectrally quiet region away from the peak. The LOD occurs when $SNR = 3$.

The emission characteristics of the elements and the matrix composition will affect the SNR of an emission line. An untreated, unintentionally contaminated CFRP was tested for the detection of the C I emission line and the Si I emission line. The C I emission at 247.9 nm corresponds to the transition $2s^22p3s\ ^1P^o \rightarrow 2s^22p^2\ ^1S$, and the Si I emission line at

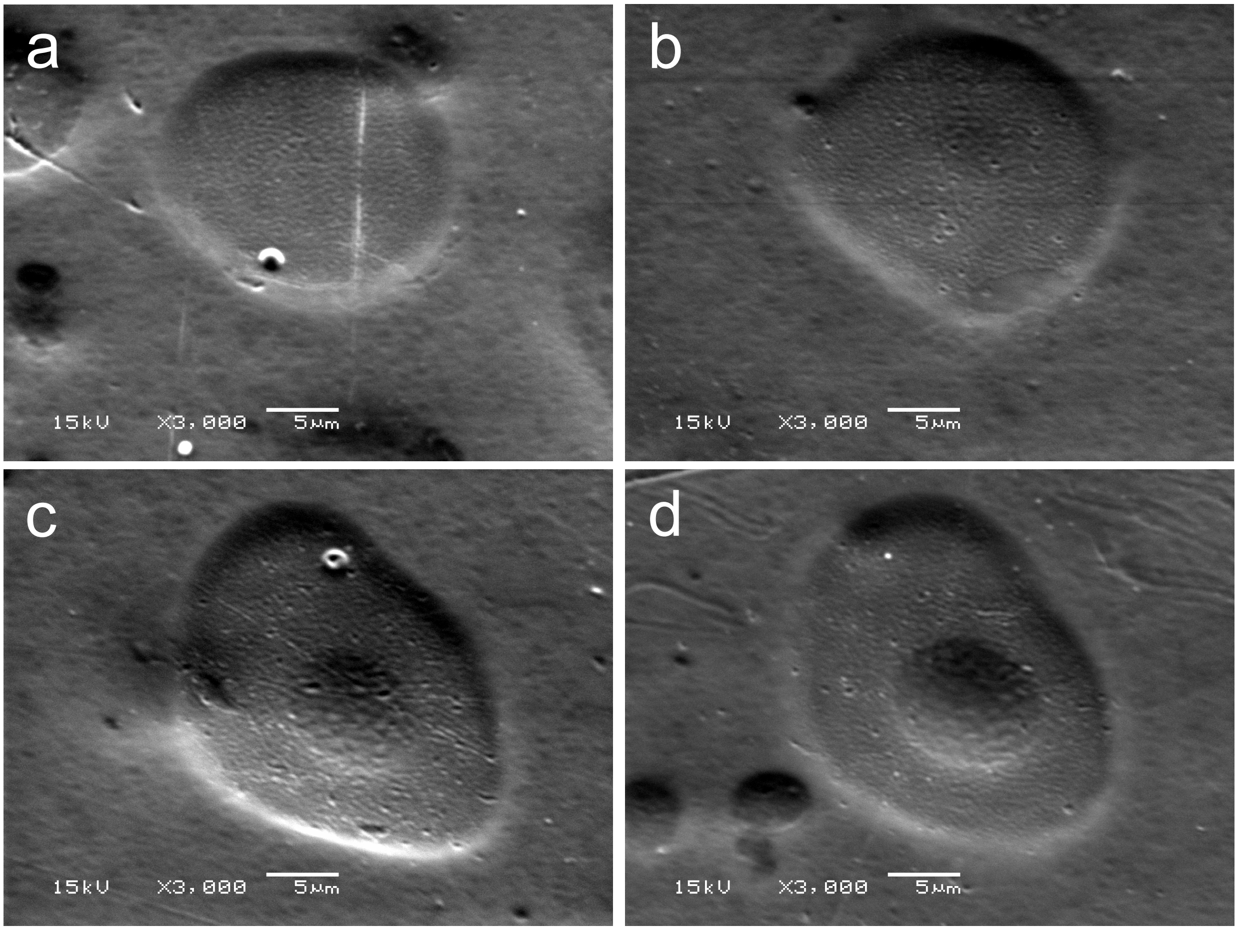

Figure 5.3: SEM micrographs of ablated craters on CFRP using single picosecond pulses of a) 7.5 µJ (3.77 J/cm^2), b) 15 µJ (7.53 J/cm^2), c) 25 µJ (12.55 J/cm^2), and d) 30 µJ (15.06 J/cm^2).

288.2 nm to $3s^23p4s\ ^1P^o \rightarrow 3s^23p^2\ ^1D$. The C I emission line is used to monitor the epoxy resin matrix from the CFRP sample, while the Si I emission line allows the monitoring of the silicone that may be present from the CFRP manufacturing. Silicone is the main component for many mold release agents used in composite fabrication. The LIBS spectra were acquired with a gate delay of 5 ns and a gate width of 250 ns. The gate width was chosen to collect all the plasma emission and to minimize noise integration on the CCD sensor. The dark signal was removed in the final frame. The spectral baseline, caused by the continuum emission, was corrected prior to calculating the SNR. Figure 5.4 shows the SNR for the C I emission line at 247.9 nm and the Si I emission line at 288.2 nm for different laser pulse energies. Each SNR data point is an average of three SNR measurements, and the error bars indicate 1σ

standard deviation. The SNR for the C I emission at 247.9 nm increases at a faster rate than that of the Si I emission at 288.2 nm. The reason is that more ablated material forms the plasma, and thus, there is an increase in C concentration that will contribute to the plasma emission. However, the concentration of Si does not significantly increase with the laser pulse energy. This may signify that the silicon compounds are localized to a uniform layer near the surface. It has been demonstrated that ablated material close to the surface contributes more to the plasma emission [147, 148]. This is also explained by the fact that the number of atoms ejected in an excited state represents a small fraction of the atoms ejected as neutrals, clusters, liquid droplets, or solid fragments [147]. Therefore, the number of emitted photons is smaller than the number of atoms ablated from the target material.

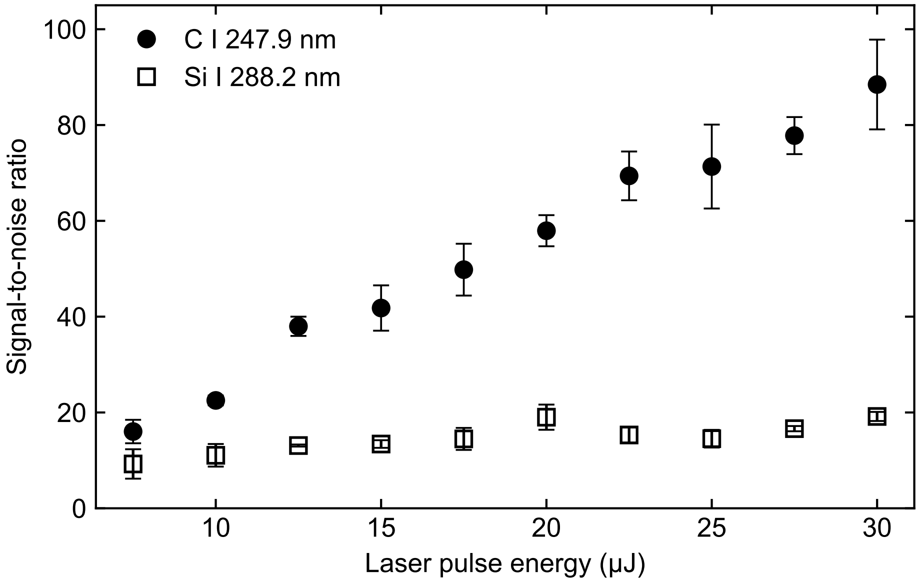

Figure 5.4: Evolution of SNR of the C I emission line at 247.9 nm and the Si I emission line at 288.2 nm for different laser pulse energies. The gate delay and gate width were set to 5 ns and 250 ns, respectively.

5.3.3 Time-resolved Analysis

The SNR varies for different gate delays and laser pulse energies. The plasma plume characteristics influence the optimum gate delay required to maximize the SNR. An untreated, unintentionally contaminated CFRP was tested to examine the SNR of C I at 247.9 nm and Si I at 288.2 nm as a function of the gate delay. A gate width of 200 ns was used in order to collect the plasma emissions and minimize noise accumulation on the CCD sensor. Figure 5.5 shows the SNR for the C I emission line at 247.9 nm for 15 μJ and 30 μJ pulse energy as a function of the gate delay. Each SNR data point is an average of three SNR measurements, and the error bars indicate 1σ standard deviation. Figure 5.6 shows the SNR for the Si I emission line at 288.2 nm for 15 μJ and 30 μJ laser pulse energy. For both laser energies, the optimum gate delays are similar for the C I and Si I emission lines from the CFRP surface. The optimum gate delay increases with the laser pulse energy. As the pulse energy increases, the plasma volume consists of more ablated material. For higher pulse energies, the plasma plume will take longer to expand and reach its optimum temperature and density for emission lines. For lower pulse energies, the generated plasma plume is smaller and less dense, and therefore the continuum emission and temperature decay faster.

A pulse energy of 15 μJ was selected for surface characterization in order to increase the surface sensitivity of the LIBS measurements using single shots and to minimize the ablation damage. This will allow the detection of surface contamination without disturbing the bulk or the carbon fibers underneath the resin surface layer. In addition, with the chosen pulse energy, the quality was not significantly compromised, assuring the correct spectral analysis for chemical identification.

Figure 5.7 shows the spectra of an untreated, unintentionally contaminated CFRP surface for different gate delays. The spectral range is 240 nm to 260 nm. To improve the SNR, each spectrum was obtained by averaging 15 frames of 10 single laser shots, and each single shot was on a fresh surface. Within that wavelength range, the main emission lines are C I at 247.9 nm and Si I at 251.6 nm. The dark signal was subtracted by online correction, but the background from the continuum emission was not corrected. Increases in the gate delay reduced the contribution of the continuum emission to the spectrum, allowing the emission lines to be more defined. For the C I emission at 247.9 nm, the optimum delay was 10 ns

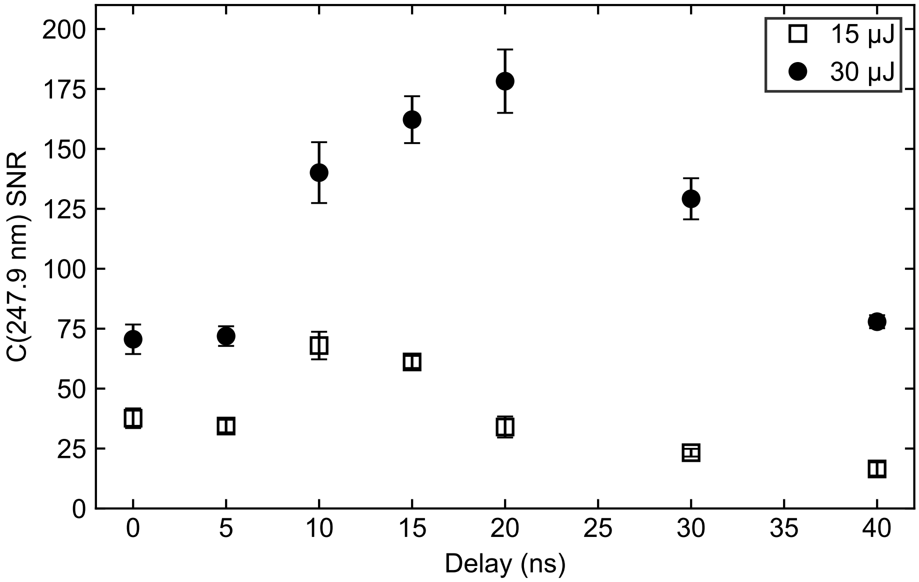

Figure 5.5: Variation of SNR as a function of the gate delay for the C I (247.9 nm) emission line for laser pulse energies of 15 µJ and 30 µJ. The sample was an untreated, unintentionally contaminated CFRP.

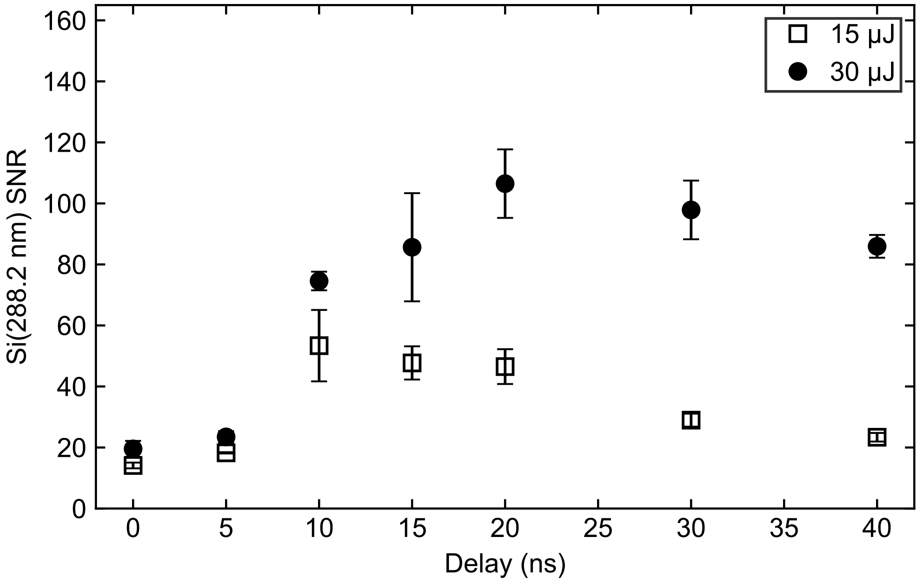

Figure 5.6: Variation of SNR as a function of the gate delay for the Si I (288.2 nm) emission line for laser pulse energies of 15 µJ and 30 µJ. The sample was an untreated, unintentionally contaminated CFRP.

for a laser pulse energy of 15 µJ, as shown in Figure 5.5. Figure 5.8 shows the spectra of an untreated, unintentionally contaminated CFRP surface for different gate delays. The spectral range is 282 nm to 294 nm. The spectral range was selected to inspect the Si I emission line at 288.2 nm. For the Si I emission at 288.2 nm, the optimum delay was 10 ns for a laser pulse energy of 15 µJ, as shown in Figure 5.6. Therefore, for both the C I (247.9 nm) and Si I (288.2 nm) emission lines, the optimum delay is 10 ns for a pulse energy of 15 µJ. The C I emission line at 247.9 nm indicates the detection of the epoxy resin matrix of the CFRP sample. The Si I emission lines at 251.6 nm and 288.2 nm reveal the presence of silicon compounds. The use of silicone based mold release agents is a source of silicon compounds that may have diffused in the epoxy matrix of the CFRP bulk during fabrication. The Si I emission lines are of interest in order to detect silicone based contaminants that interfere with adhesive bonding even at low concentrations [133].

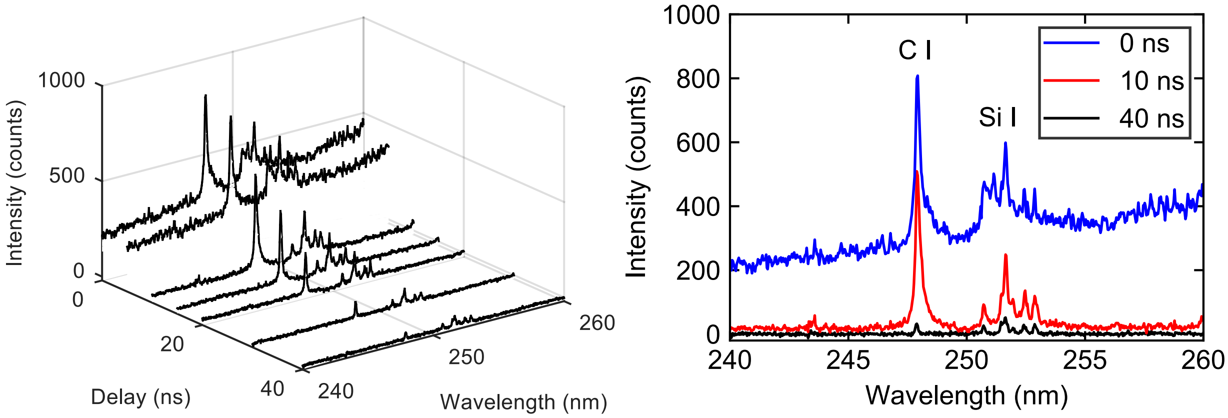

Figure 5.7: Dark signal corrected spectra from an untreated CFRP using 15 µJ pulses for different gate delays. The main emission lines are C I at 247.9 nm and Si I at 251.6 nm. Each spectrum was obtained by averaging 15 frames of 10 single laser shots. Each single shot was on a fresh surface. The continuum emission decreases as the gate delay increases, allowing more defined emission lines.

5.3.4 Laser Surface Ablation

Laser ablation is intended for surface contamination removal and surface preparation prior to adhesive bonding. The same laser system was employed for both laser surface treatment and LIBS characterization. This allows for rapid feedback from LIBS concerning the surface condition.

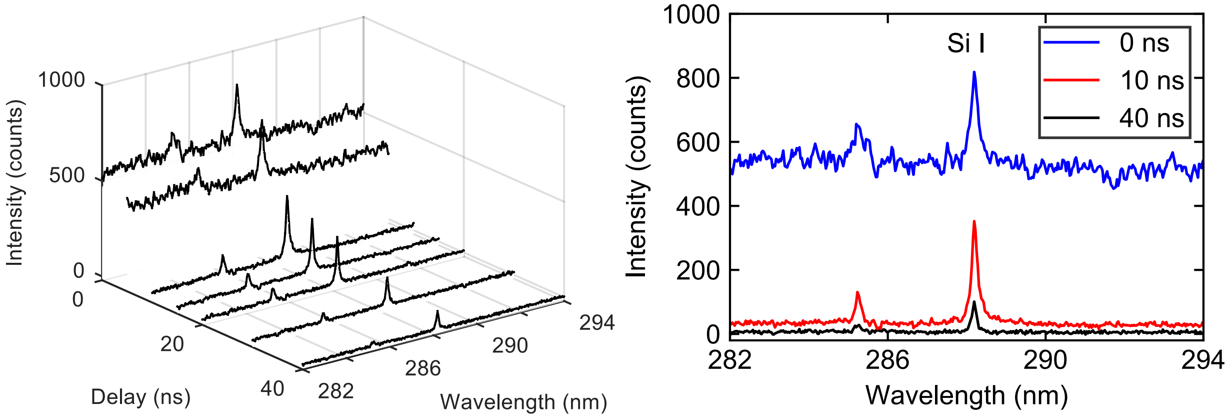

Figure 5.8: Dark signal corrected spectra from an untreated CFRP using 15 µJ pulses for different gate delays. The main emission line is Si I at 288.2 nm. Each spectrum was obtained by averaging 15 frames of 10 single laser shots. Each single shot was on a fresh surface. The continuum emission decreases as the gate delay increases, allowing more defined emission lines.

CFRP samples were inspected using LIBS to detect PDMS prior to and after laser surface ablation. Prior to PDMS contamination, the CFRP surfaces were degreased with a mild soap solution, rinsed thoroughly with water, and then dried. The control sample was not coated with PDMS and served as a reference surface. Table 5.1 shows the characteristics of the PDMS coatings. The PDMS areal number density n_A was calculated by

$$n_A = \frac{\rho N_A l}{M_m} \tag{5.3}$$

where ρ is the density of PDMS, N_A Avogadro's number, l the PDMS film thickness, and M_m the PDMS molecular weight. The PDMS film thickness is determined by ellipsometry on smooth p-type Si[100] surfaces. The PDMS distribution on Si substrates will differ from the thickness of PDMS distributed on CFRP surfaces due to their roughness and heterogeneity.

Figure 5.9 shows the LIBS spectra obtained from select CFRP surface conditions prior to laser ablation. The select PDMS areal densities were 0.15 µg/cm^2, 0.26 µg/cm^2, 0.34 µg/cm^2, and 2 µg/cm^2. The emission lines of interest are C I at 247.9 nm and Si I at 288.2 nm. Other neutral Si lines are detected between 250 nm and 255 nm, the strongest peak being at 251.6

Table 5.1: Characteristics of the PDMS coatings on CFRP surfaces. The PDMS thickness was characterized by ellipsometry. The PDMS areal density and areal number density were calculated. The latter was determined using Eq. 5.3. The mean values are indicated along with their 1σ standard deviations.

Thickness (nm)	Areal density (µg/cm^2)	Areal number density (10^{12} molecules/cm^2)
0 (Control)	0	0
1.54 ± 0.08	0.15 ± 0.008	2.5 ± 0.13
2.12 ± 0.03	0.2 ± 0.003	3.5 ± 0.05
2.63 ± 0.09	0.25 ± 0.009	4.3 ± 0.15
2.73 ± 0.1	0.26 ± 0.01	4.5 ± 0.15
3.56 ± 0.62	0.34 ± 0.06	5.8 ± 1
20.49 ± 0.03	2 ± 0.003	33.6 ± 0.05

nm. The surfaces with higher PDMS areal density show stronger emission intensities for the neutral Si species between 250 nm and 255 nm. The intensity of the neutral C peak at 247.9 nm remains similar for all surface conditions. The intensity of the Si emission line at 288.2 nm for the control sample differs significantly from the PDMS coated surfaces.

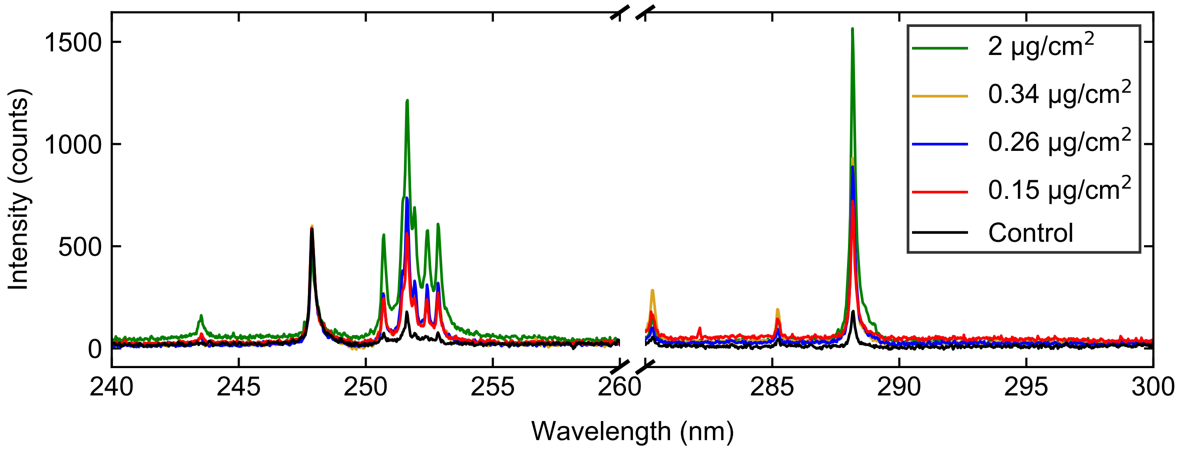

Figure 5.9: LIBS spectra prior to laser ablation for the UV regions from 240 nm to 300 nm. The peaks of interests are 247.9 nm for C I, and 251.6 nm and 288.2 nm for Si I. Other neutral Si lines are detected between 250 nm and 255 nm.

The CFRP surfaces were laser ablated with an energy fluence of 0.1 J/cm^2, a scan speed of 25.4 cm/s, and a line pitch of 12.7 µm. Figure 5.10 shows the laser ablated surface of the control CFRP sample. The parallel lines were laser ablated in the fiber direction, as shown in the SEM micrographs in Figure 5.10. The ablated lines produced a surface pattern without disturbing the carbon fibers underneath the resin surface layer. As shown in Figure 5.10b, the laser ablated portion of the surface (left) is rougher than the untreated surface (right).

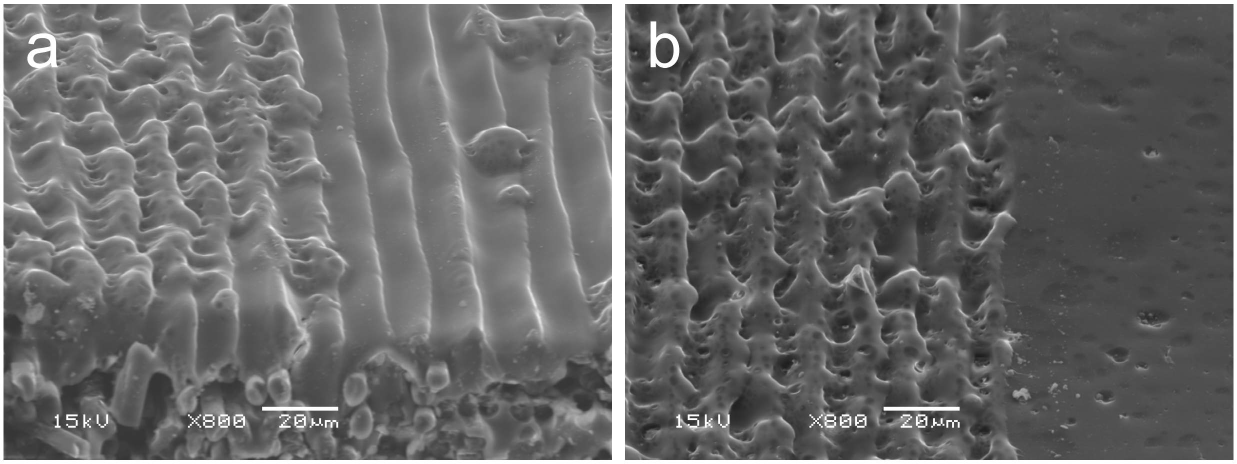

Figure 5.10: SEM micrographs of the control CFRP surface after laser ablation. (a) The parallel lines were ablated in the fiber direction with a line pitch of 12.7 µm. (b) This SEM micrograph shows the morphology differences between a laser ablated surface and an untreated region.

After laser ablation, the CFRP surfaces were characterized with LIBS. Figure 5.11 shows the spectra of the different CFRP surface conditions after laser ablation. In contrast to Figure 5.9, the neutral Si lines between 250 nm to 255 nm decreased significantly following laser ablation. For the control surface, the Si I peak at 251.6 nm could not be detected and was negligible in intensity. For the PDMS contaminated surfaces, there was still Si detected indicating that silicone remained present on the surface. The Si I emission line at 288.2 nm decreased significantly in comparison to that of Figure 5.9. The detection of Si peaks after laser ablation means that the silicone contaminant was not removed completely from the CFRP surfaces under these ablation conditions.

The data are presented as the ratio of the Si and C peak heights before and after laser ablation as shown in Figure 5.12. The Si/C peak ratio was used as an analytical parameter to compare the relative abundance of Si from silicone and C from the matrix resin. The bars represent the mean values and the error bars indicate 1σ standard deviation. The selected

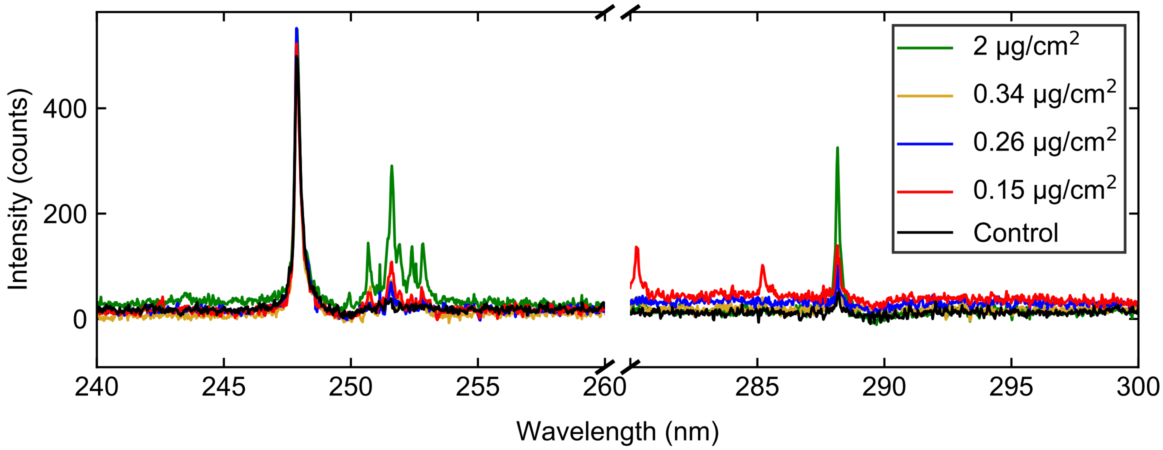

Figure 5.11: LIBS spectra after laser ablation for the UV regions from 240 nm to 300 nm. The peaks of interests are 247.9 nm for C I and 251.6 nm and 288.2 nm for Si I. Other neutral Si lines are detected between 250 nm and 255 nm.

peaks for Si I are 251.6 nm and 288.2 nm. The level of silicone contaminant was significantly reduced after laser ablation. For the control sample, the Si/C ratio for Si at 251.6 nm decays from 0.27 to 0.042, while for Si at 288.2 nm the ratio decreases from 0.3 to 0.063. Considering the surface with the highest PDMS areal density (2 µg/cm2), the Si/C ratio decays from 2.78 to 0.51 for Si I at 251.6 nm and from 3.91 to 0.64 for Si I at 288.2 nm. Therefore, considering the Si I line at 288.2 nm, the Si/C ratio decreased by ∼87%. The sensitivity of the LIBS system was able to readily detect the low levels of silicone contamination (3.4 ± 0.2 at.% using the Si 2p peak measured by XPS before laser ablation) on the control sample. Thus, LIBS can detect silicone contaminants at concentrations less than those known to pose a threat to adhesive bonding with this CFRP material system (< 1 µg/cm^2) [133], requires no sample preparation, and can provide rapid feedback of Si contamination levels. With the Si/C ratio as an analytical metric, it is possible to differentiate the control surface from the contaminated surfaces, as well as the laser treated surfaces from the untreated ones.

Figure 5.13 shows the calibration plot of the Si/C ratio as a function of the PDMS areal density before and after laser ablation. For the linear fits in the inset plot, the y-axis intercept is nonzero due to the intrinsic silicone amounts on the CFRP surfaces from the fabrication

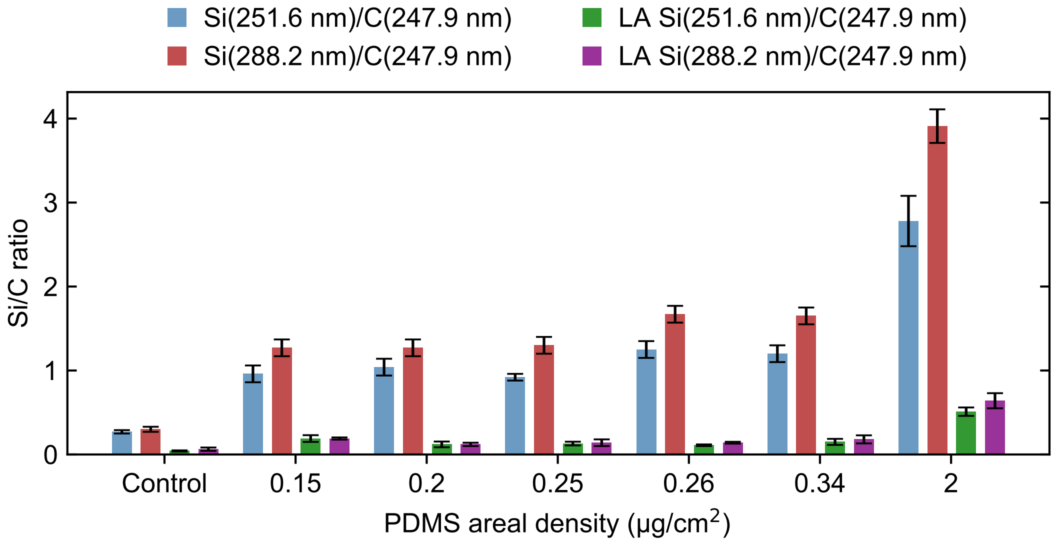

Figure 5.12: Si/C ratios for CFRP samples before and after picosecond laser ablation (LA). All the surfaces, except for the control, were coated with PDMS at different concentrations, producing different PDMS areal densities.

process, and after laser ablation, there is still trace silicone on the composite surfaces. The linear fit for the data before ablation is $y_1 = 4x + 0.44$, and for the data after laser ablation, the linear fit is $y_2 = 0.26x + 0.09$.

5.4 Conclusions

In this study, picosecond μLIBS was investigated for detection of silicone contaminants on CFRP surfaces. Using single laser shots, the ablation threshold of the resin surface layer in the CFRP material system was found to be 2.4 μJ. From the ablation depth analysis, the effective optical penetration depth was determined to be 0.33 ± 0.07 μm. By analyzing the ablation depth for different pulse energies, it was possible to select the parameters for LIBS analysis that minimize the ablation damage and increase the sensitivity of detection of surface contaminants. The outcome from the SNR analysis showed that the silicone present in the epoxy resin matrix is localized to a uniform layer near the surface. The time-resolved analysis was applied to obtain the optimum gate delay for the collection of plasma emissions.

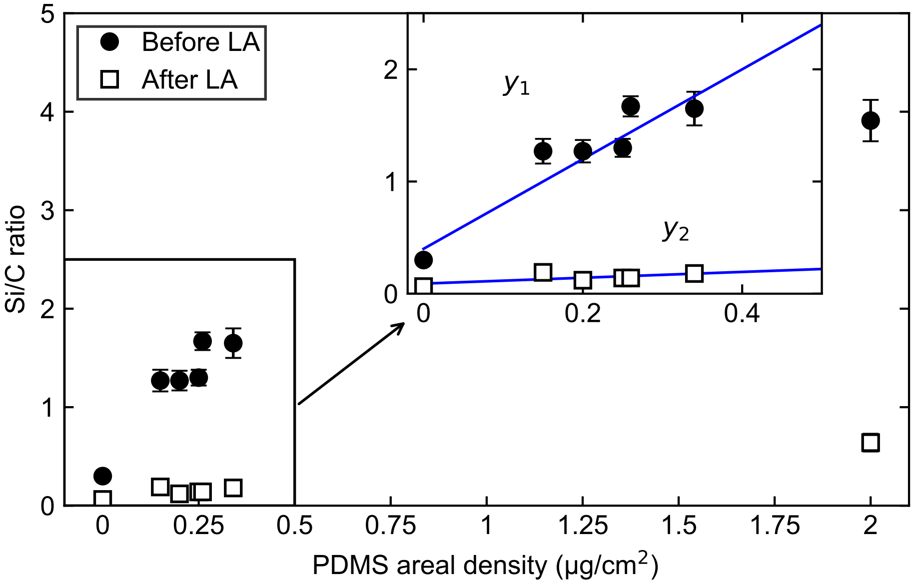

Figure 5.13: Si/C ratio as a function of the PDMS areal density before and after picosecond laser ablation (LA). The zero areal density represents the control surface. The linear fit $y_1 = 4x + 0.44$ is for the data before LA, and $y_2 = 0.26x + 0.09$ is the linear fit for the data after LA.

Detection of PDMS was demonstrated using 355 nm, 15 µJ pulses. The presence of PDMS on the epoxy matrix composites increased the Si emission intensity while suppressing the C line emission from the matrix material. After laser ablation, the C line emission increased whereas the Si line emission decreased. This demonstrated that the amount of PDMS was significantly decreased after laser surface ablation. This was corroborated by the ∼87% decrease of the Si/C ratios for all the inspected CFRP surfaces, considering the Si I line at 288.2 nm. LIBS provided a rapid surface characterization before and after laser surface ablation. Each level of PDMS contamination on the CFRP surface yielded a unique spectral response that allowed the differentiation of Si levels from that of a control CFRP. The spectral response of each contaminated surface demonstrates that materials close to the surface will contribute more to the LIBS signal. Therefore, it is possible to detect low levels of silicone for different surface conditions. The results support the hypothesis that picosecond µLIBS achieves high surface sensitivity to thin contamination layers on CFRP surfaces with both minimal ablation damage and thermal stress. Picosecond µLIBS provides sensitive detection of low levels of silicone contaminants prior to adhesive bonding of CFRP structures. By using the same laser system for both surface treatment and LIBS analysis, LIBS has potential as an in-situ technique that can be automated and integrated into the laser surface ablation process.

Chapter 6

Trace Silicone Contamination Analyses on CFRP by XPS and LIBS*

Surface characterization of CFRP composites with epoxy matrix was performed using LIBS, and the results were compared with those obtained from XPS. LIBS offers many advantages over XPS in terms of ease of use, sample preparation, and real-time results. The objective of the comparison was to study the sensitivity of LIBS and to investigate the quantification of the surface species measured by LIBS. Another objective was to assess the reliability of each technique for surface contaminant characterization. The as-processed CFRP panels had trace surface silicone contamination from the fabrication process. The composites were laser treated at select average laser power levels, resulting in varying levels of contamination reduction. The Si atomic percentage measurements using XPS were conducted on both control and laser ablated surfaces. The results showed an excellent correlation in Si concentration between the two techniques.

6.1 Introduction

A major goal of the NASA Advanced Composites Project (ACP) is reducing the timeline to certification by 30% for composite structures on commercial transport aircraft. Within the Efficient Manufacturing Processes Technical Challenge under ACP, there is a task focused on bonded structure and automated surface treatment. Within this task, team members from The Boeing Company, United Technologies - Pratt and Whitney, UTC Aerospace Systems,

---

*The main results and content of this chapter have been published in R. Ledesma, F. Palmieri, B. Campbell, W. Yost, J. Fitz-Gerald, G. Dillingham, J. Connell, Appl. Spectrosc. (2018) [149].

and NASA Langley Research Center (LaRC) have been evaluating various surface treatment methods, effects of various contaminants on adhesive bonding, and characterization tools for surface analysis [6, 75, 150–152]. Laser ablation is an attractive means of surface preparation of CFRP composites and metal alloys because it provides a clean, high precision, reproducible surface that enables high quality adhesive bonds [5, 6, 153–155].

Silicone contamination can be introduced into the CFRP laminate from the fabrication process. Even though the source of silicone contamination was not investigated, it is likely from the silicone-based mold release agent often used in our laboratory during the fabrication of composite laminates. Other items such as gloves and tools may be sources that carry silicone. In addition, some silicone species can volatilize and condense on adherend surfaces. The ability of commercial off-the-shelf (COTS) tools to reliably detect such low concentrations of silicones on surfaces was found to be lacking in requisite sensitivity and precision, ease of use, and/or data acquisition and analysis time. In some cases, COTS tools require destructive, time consuming sample preparation methods. In contrast, LIBS is a non-destructive and rapid method. In conjunction with laser ablation surface treatment, LIBS has shown significant promise in detecting silicones at concentrations well below the level known to be a threat to bonding.

In this work, the aim was to study the sensitivity of LIBS in detecting silicones by comparing the LIBS results with those of XPS. Unlike XPS, LIBS analysis is conducted in the open air at ambient pressure, no sample preparation is necessary, and the results are nearly instantaneous. The work described herein involved fabrication of two-ply epoxy composite laminates which had inherent silicone contamination, followed by laser ablation at select laser power levels to produce various surface conditions. The same surface conditions were analyzed by XPS and the results were correlated to the Si/C ratio from LIBS data. The results show an excellent correlation between the silicone levels detected by LIBS and XPS. LIBS exhibited sensitivity comparable to that of XPS, and readily detected very low levels of silicone on the CFRP surface. In addition, the silicone removal efficiency of the laser surface ablation was evaluated by adjusting the laser power and correlating it to the Si/C ratio from LIBS data. Modification of the surface topography after laser surface ablation was analyzed by SEM.

6.1.1 Laser Surface Treatment

Laser surface treatment enables high precision processing that lends itself to automation and reproducibility for surface activation and removal of surface contaminants on CFRP surfaces [5–9, 75, 150–155]. By adjusting the laser parameters, it is possible to control the laser-solid interactions to remove surface contaminants and create texture on the surface without exposing or breaking the carbon fibers underneath the resin surface layer. This technique can also be used for other surfaces such as metal alloys, and can be used to selectively remove surface layers such as paint or coatings without affecting the underlying substrate.

In this work, a picosecond laser was used to chemically activate and remove surface contaminants (e.g. silicones) on carbon fiber reinforced epoxy composite surfaces. Picosecond and ultrashort pulses enable the ablation of CFRP composites with low average laser power, which mitigates subsurface interlaminar damage.

6.1.2 LIBS

In this work, μLIBS was used for CFRP surface analysis [46, 75, 108–110, 156]. The laser system used for LIBS surface characterization was the same as that for laser surface treatment, providing the opportunity for in-situ surface inspection prior to and after laser ablation. The implemented LIBS system in the LaRC laboratory enabled the non-destructive surface characterization of CFRP surfaces in a rapid manner without any sample preparation or special atmospheric conditions [75].

6.1.3 XPS

XPS is a quantitative surface characterization technique that provides chemical information about a material, including the elemental composition at the parts per thousand range, empirical formula, chemical state, and electronic state, with a typical depth sensitivity between 10 Å and 50 Å. By irradiating the material with an X-ray source, the kinetic energy of the ejected electrons is measured. The take-off angle can influence the detected electron flux and therefore, the surface sensitivity. To enable high surface sensitivity, the instrument's analysis chamber must be maintained at high vacuum (HV) or ultra-high vacuum (UHV), typically between 10^{-7} and 10^{-10} Torr. This required vacuum level limits the sample chamber size, which necessitates substantial composite specimen dimensional preparation. Following data collection, a significant amount of data reduction must be conducted to extract the desired information concerning the chemical composition of surface species.

6.2 Experimental

6.2.1 Materials

The process of fabricating epoxy composites has been described previously [6, 75]. Two-ply unidirectional CFRP panels (30.5 cm × 30.5 cm) were fabricated from two plies of unidirectional Torayca P2302-19 (T800H/3900-2) prepreg. The prepreg was cured in an autoclave at 177 °C and 690 kPa. Release of the composite panel from the caul plate was achieved using Airtech A4000V release film, a FEP film. Tool and caul surfaces were pre-treated with Zyvax WaterShield, a silicone-based mold release agent dispersed in water. CFRP coupons of 2 cm × 3 cm were prepared for LIBS surface characterization. Subsequently, for XPS analysis, those coupons were cut into four specimens of 1 cm × 1.5 cm.

Another set of two-ply CFRP surfaces was laser ablated and coated with Pd-Au for SEM measurements and analyzed using a JEOL JSM-5600 scanning electron microscope operated at an accelerating voltage of 15 kV.

6.2.2 Laser Ablation

Laser ablation was performed with a Nd:YVO$_4$ laser system (Atlantic 20-355, EKSPLA) operated at 355 nm with ∼10 ps pulse width. To produce different surface conditions, two-ply unidirectional CFRP surfaces were laser processed using a pulse frequency of 400 kHz at select average laser power levels, ranging from 40 mW to 180 mW. The average laser power was measured with a thermopile sensor (30A-BB-18, Ophir-Spiricon) and a laser power meter (Nova II, Ophir-Spiricon). The CFRP surfaces were laser ablated with parallel lines, which were produced in the fiber direction at 12.7 μm line pitch and 25.4 cm/s scan speed. These laser conditions were constant throughout all of the experiments.

6.2.3 LIBS

The laser system utilized for LIBS characterization experiments was the same that was used for laser ablation surface treatment. The laser pulse energy was 15 μJ (7.53 J/cm^2). The plasma emission was collected with a collimator and guided to the spectrograph via an optical cable with 19 fibers (200 μm each). The LIBS emission was collected using a 328 mm, f/4.6 SCT spectrograph (IsoPlane SCT 320, Princeton Instruments). The optical emission entered the spectrograph through a slit of 10 μm width and was dispersed by a grating with 600 grooves/mm, blazed at 300 nm. The spectral response was recorded using an emICCD camera (PI-MAX4: 1024 EMB, Princeton Instruments), which was externally triggered by the laser trigger output.

A LIBS spectrum was generated by averaging 10 frames of 10 single laser shots. The target surface was moved with a XY stage after each single shot to expose a fresh surface for each incident pulse. The 10 single laser shots were accumulated on the CCD sensor. The gate delay and the gate width were set to 10 ns and 200 ns, respectively.

6.2.4 XPS

XPS analysis was performed in two separate facilities, one in the LaRC laboratory (Hampton, VA) and the other in BTG Labs (Cincinnati, OH). In the LaRC laboratory, the CFRP coupons, 1 cm × 1.5 cm, were characterized with a DESA-100 analyzer (STAIB Instruments) and a monochromatic Al K-alpha X-ray (1.486 keV photon energy) source, operated at 15 kV. Three survey scans were performed from 1100 eV to 0 eV on the CFRP surface. Each survey scan was taken in a different location on the sample surface. The take-off angle was 90°.

In BTG Labs, the CFRP coupons were analyzed with a Surface Science Instruments SSX-100 and a monochromatic Al K-alpha X-ray (1.486 keV photon energy) source, operated at 10 kV. The analysis area was 800 µm × 800 µm, and the take-off angle was 45°. Each survey scan was taken in a different location on the target surface.

6.3 Results and Discussion

The laser power conditions for treatment of the two-ply unidirectional CFRP surfaces are shown in Table 6.1. By changing the laser power, the amount of silicone contaminant removed was varied. For LIBS experiments, 20 measurements were conducted at different locations on CFRP coupons of 2 cm × 3 cm. The same coupons were cut into four coupons of 1 cm × 1.5 cm to fit the XPS analysis chamber. For the XPS measurements at LaRC, one coupon was analyzed, while BTG Labs analyzed two coupons. Regarding the CFRP surfaces ablated at 120 mW, two coupons were inspected at LaRC and four at BTG Labs. The number of XPS measurements is shown in Table 6.1. Several aspects of XPS analyses at the two facilities were different. The take-off angles for the two instruments (LaRC, 90° and BTG, 45°) can affect the results, especially at high silicone concentrations. The relationship between both electron escape depths is $d_B = \frac{\sqrt{2}}{2} d_L$, where d_B is the BTG Labs depth and d_L the LaRC depth. The time that elapsed after laser ablation treatment and when the XPS analyses were performed was also different. Typically, at LaRC, the XPS analyses were conducted within 24 to 48 hours after laser treatment since the laser system and XPS instrument were co-located. In the case of BTG, more time elapsed (72 to 96 hours) between the laser treatment and XPS analyses since the samples had to be packaged and shipped after laser treatment at LaRC.

Table 6.1: Average laser power levels used to produce different surface conditions shown with the number of XPS measurements.

Laser power (mW)	Number of measurements	
	LaRC	BTG Labs
0 (Control)	3	4
40	3	4
60	3	6
80	3	6
90	3	6
100	3	4
120	6	12
140	3	6
160	3	6
180	3	6

6.3.1 Surface Characterization Analysis

The XPS observations underwent outlier analysis for statistical inconsistencies. The methods applied were Mahalanobis distance, standardized residuals, and QQ-plot to provide a robust data rejection decision.

The silicone contaminant was monitored using the Si I emission line at 288.2 nm ($3s^2 3p4s\ ^1P^o \rightarrow 3s^2 3p^2\ ^1D$) while the C I emission line at 247.9 nm ($2s^2 2p3s\ ^1P^o \rightarrow 2s^2 2p^2\ ^1S$) was used as a reference for the epoxy matrix. Figure 6.1 shows representative LIBS spectra for two epoxy composite surfaces; one was a control and the other was laser ablated at 180 mW average laser power. Control surfaces are surfaces with inherent silicone contamination from the fabrication process and have not been laser treated prior to LIBS analysis. The difference in LIBS signal intensity was clear between the control and the ablated surface. There was a decrease in the Si I emission lines (251.6 nm and 288.2 nm) following laser ablation, whereas there was an increase in the C I emission line (247.9 nm).

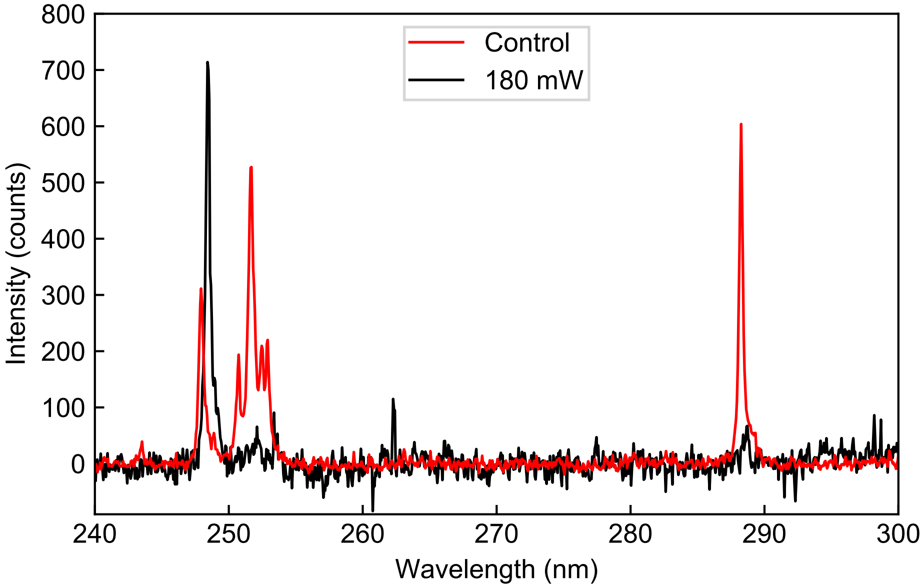

Figure 6.1: Spectra of control and laser ablated (180 mW) epoxy composite surfaces. The background was corrected for both spectra.

Figure 6.2 shows the Si/C ratio from the LIBS results as a function of the Si concentration determined by XPS. In LIBS, the Si emission lines detected were assumed to emanate from the Si in the polymeric silicone contaminant. The LIBS Si/C ratio was determined using the peak heights of the Si I emission line at 288.2 nm and the C I emission line at 247.9 nm. It was assumed that all Si species detected by XPS emanated from the polysilicone contaminant. The Si 2p peak was chosen for the detection and measurement of trace silicone on CFRP surfaces. Linear regression was applied to each XPS data set. The y-intercepts of the linear fits were zero and both slopes were similar. At higher concentrations, the difference between XPS measurements (LaRC and BTG) was ∼0.5 at.%, and at lower concentrations the measurements converged. Take-off angle influences the detection depth, and therefore affects the concentration of Si with respect to other elements. Overall, the XPS results showed excellent agreement in silicon content, suggesting that the difference in time elapsed between laser treatment and XPS analysis (within the time frame mentioned) did not affect the silicone surface contamination.

The LOD from the calibration curves presented in Figure 6.2 was calculated using linear

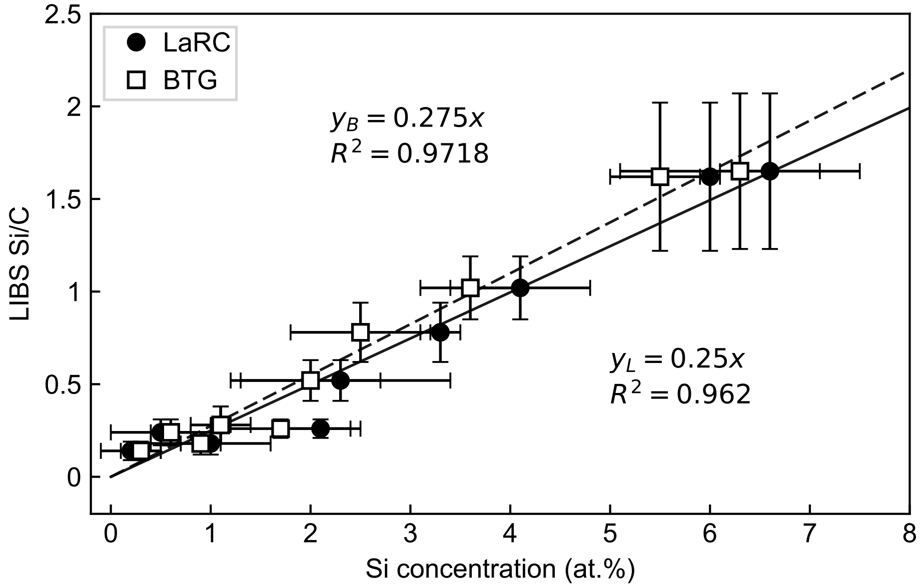

Figure 6.2: Si/C from the LIBS measurements as a function of Si concentration measured by XPS at both NASA LaRC and BTG Labs. The linear fits y_L (solid line) and y_B (dashed line) correspond to LaRC and BTG, respectively.

regression with an equation in the following form: $r = Sc$, where r is the intensity ratio, c the concentration, and S the slope, also called the analytical sensitivity. The LOD was determined by [157]

$$c_L = \frac{3\sigma}{S} \tag{6.1}$$

where c_L is the concentration limit of detection and σ is the standard deviation of the measurements of the surface with the least analyte concentration. The detection limits for LaRC and BTG are 0.6 at.% and 0.54 at.%, respectively.

The Si/C ratios determined from LIBS and XPS measurements are compared in Figure 6.3. The slopes of the linear fits were similar with both y-intercepts set to zero. This again shows that there was excellent agreement between the two laboratories with respect to the XPS measurements, and a high degree of correlation between the Si/C ratios determined by LIBS and XPS.

The XPS measurements from LaRC and BTG Labs were compared for agreement, as shown in Figure 6.4. The relationship between XPS measurements from the two facilities is

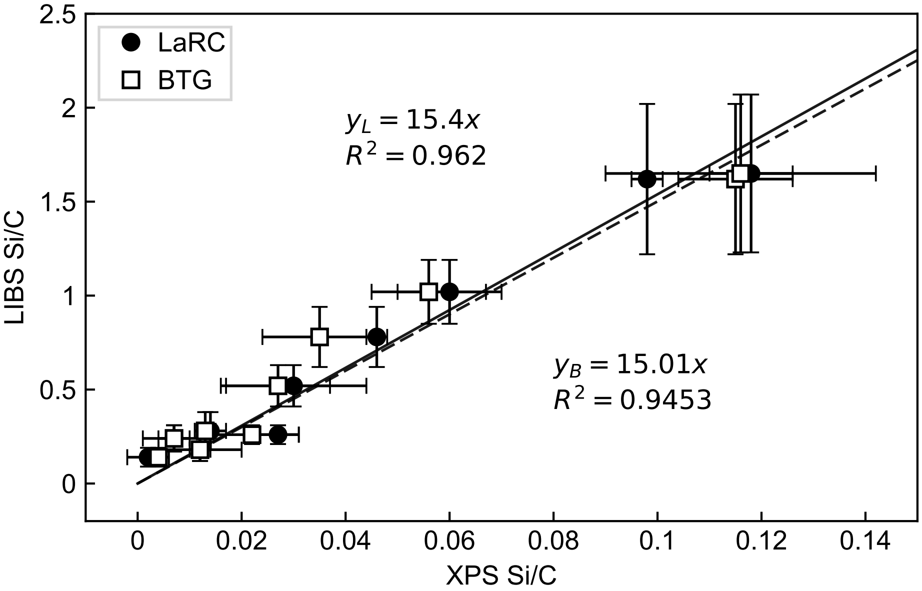

Figure 6.3: Comparison of LIBS Si/C and XPS Si/C. The linear fits y_L (solid line) and y_B (dashed line) correspond to LaRC and BTG, respectively.

close to unity; any incongruence is likely due to the difference in take-off angles of the two instruments used.

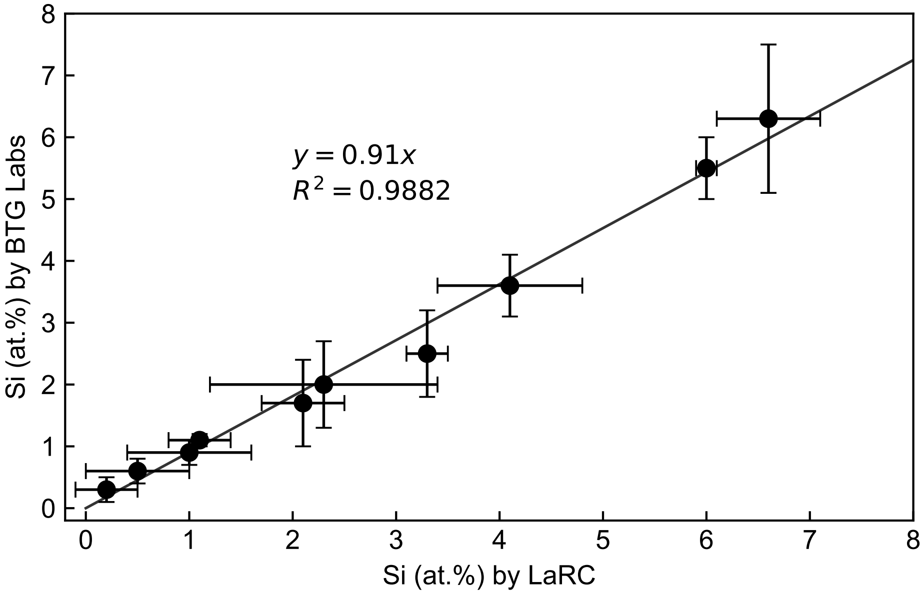

Figure 6.4: Si concentration measured by XPS at NASA LaRC and BTG Labs.

6.3.2 Laser Ablation Performance

The laser ablation performance was studied using the Si/C ratio from the LIBS measurements. The laser ablation at different laser power levels produced different surface conditions and thus different Si/C ratios. Figure 6.5 shows the Si/C ratio as a function of the average laser power utilized for laser surface treatment. Each data point was the average of 20 measurements, except for the data point at 120 mW, which was the average of 40 measurements. Based on previous experiments with the same material system, the width ablation threshold was estimated to be ∼24 mW under the same laser treatment conditions. At 40 mW, the UV laser pulses did not produce measurable surface modification on the two-ply unidirectional CFRP surface. This was likely due to the laser power being around the ablation threshold of the epoxy matrix. This can be seen clearly in the SEM micrograph in Figure 6.6a, where the CFRP surface remained almost intact after 40 mW laser treatment. Therefore, the Si/C ratios of the control surface (0 mW laser power) and the surface ablated at 40 mW were similar since no significant ablation occurred. Silicone materials weakly absorb from the UV to visible wavelengths (200 nm to 750 nm) [139]. However, the resin surface layer in CFRP has higher absorption levels at 355 nm [7, 158, 159]. Thus, the removal of silicone contamination in CFRP composites seems to couple with preferential ablation of the epoxy resin. Figure 6.5 also shows that increasing laser power led to more efficient removal of silicone contaminant. In previous work from our laboratory, Si/C ratios of less than 0.2 resulted in high quality bonded specimens that failed ∼100% cohesively, with this epoxy composite system and EA9696 epoxy film adhesive [141]. This means that the desired laser power under the previously described scan speed, frequency, and pitch, should be at least 100 mW. However, it is important to know how much silicone contamination is on the CFRP surface prior to laser ablation surface treatment so that ablation parameters can be judiciously selected.

Figure 6.6 shows the SEM micrographs of the laser ablated CFRP surfaces for select laser power levels. Again, there was no substantial surface modification in some regions

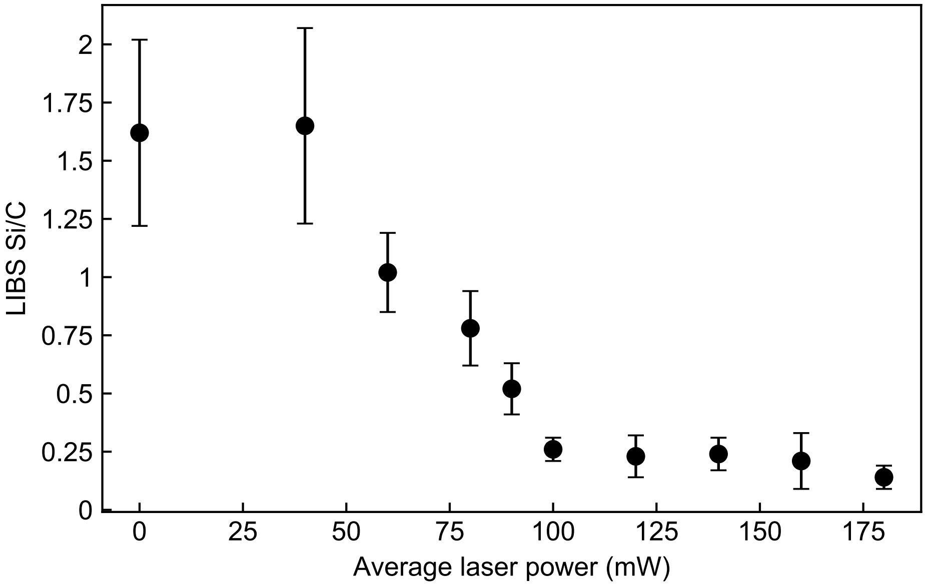

Figure 6.5: Si/C from LIBS data as a function of average laser power used for laser surface treatment. The laser power of zero corresponds to the control surface.

by the 40 mW picosecond laser pulses, whereas on some edges, as shown in Figure 6.6a, the ablative lines were more evident. As the power increased, the laser ablation was more significant and was sufficient to remove the resin surface layer, as shown in Figures 6.6b to 6.6d. The SEM micrographs also show that the resin surface layer was removed without exposing the underlying carbon fibers. No exposed carbon fibers or heat affected zones were observed. The resin surface layer thickness was non-uniform, and after laser ablation there were some locations that showed clusters of epoxy resin while other treated locations resulted in a smoother resin surface.

6.4 Conclusions

LIBS analysis of silicone surface contamination was conducted using a picosecond laser on control and laser-ablation treated CFRP surfaces. The Si/C ratio from LIBS measurements was compared with the Si concentration (Si 2p) from quantitative XPS data using two different instruments. The LIBS system developed at LaRC demonstrated excellent sensitivity with

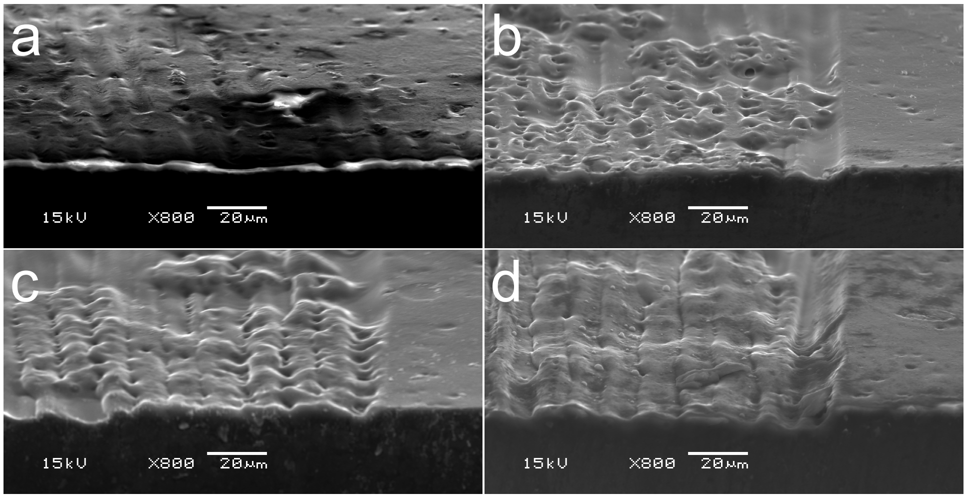

Figure 6.6: SEM micrographs of laser ablated CFRP surfaces at average laser power levels of a) 40 mW, b) 80 mW, c) 120 mW, and d) 180 mW. There is no exposure of underlying carbon fibers.

Si concentrations below 0.5 at.% detected on CFRP surfaces. From the calibration curves obtained using the LIBS Si/C ratio as a function of the Si concentration from the XPS data, the detection limits for LaRC and BTG were determined to be 0.6 at.% and 0.54 at.%, respectively. The Si/C ratios determined by LIBS and XPS exhibited excellent correlation. The similarity of the XPS results validates the data from both XPS instruments. These results demonstrate the ability of LIBS to be used as a high-fidelity tool to detect and measure surface silicone contamination in near real-time with a sensitivity equivalent to XPS.

Chapter 7

Summary & Future Work

7.1 Summary

In this work, two surface characterization techniques, OSEE and LIBS, were studied for their applicability to the inspection and detection of trace silicone contamination on laser treated CFRP surfaces for improved adhesive bonding. Laser ablation is a technology investigated for the past decade at NASA Langley Research Center for the removal of surface contaminants and for surface chemical activation. The monitoring of the adherend surface preparation is critical to ensure durable adhesively bonded structures that meet rigorous inspection criteria. The goal of the present research work was to develop characterization methods that can:

- identify the chemistry of the surface species,
- be sufficiently sensitive to detect trace amounts (< 1 μg/cm^2) of the contaminant species, and
- characterize adherend surfaces in near real time without sample preparation or special measurement environments.

7.1.1 OSEE

The application of OSEE to CFRP substrates was examined as a method to detect monomolecular silicone contaminants and to predict interfacial adhesive bonding performance. Cohesive failure modes observed after DCB mechanical testing were correlated to the OSEE photocurrent. Laser ablation using nanosecond pulses at 355 nm exposed unbroken carbon fibers, which increased the OSEE photocurrents. The surface epoxy resin layer, along with the surface contamination, was removed by laser ablation. The work function was changed by the electric and photoresponsive properties of the carbon fibers. The photocurrents were also correlated to the regions within the loading and unloading boundaries from the load-displacement traces. This approach was adopted owing to the nonlinear elastic material properties of the substrates and adhesive. The correlation of OSEE photocurrent with failure modes obtained from DCB mechanical tests support the hypothesis that surface contamination species and concentrations modify adherend fracture characteristics.

OSEE did not meet all the requirements of the overall goal of this work. As mentioned earlier, OSEE requires a specific measurement environment, and does not provide chemical information about the surface contaminants. These shortcomings will be discussed below in the Future Work section.

7.1.2 LIBS

This work addressed the application of LIBS to aerospace structures such as CFRP composites. The LIBS technique was advanced by using picosecond laser pulses and microjoule pulse energies. The picosecond laser pulses enabled photochemical ablation of the surface epoxy layer in the CFRP substrate by multiphoton transitions owing to the high peak intensity, and the optical breakdown was achieved with microjoule pulse energies. Time-resolved analyses of LIBS spectra were performed to optimize the SNR and to improve the atomic line detection. The surface sensitivity was studied by conducting LIBS on CFRP surfaces with different silicone contamination concentrations. The efficiency of laser ablation to remove silicone contamination on CFRP surfaces was assessed using LIBS at 355 nm with 15 microjoule single pulses. The Si/C ratio decreased ∼87% after laser ablation for all the CFRP surface conditions. Surface contamination layers of silicone were detected below 0.15 $\mu g/cm^2$ (∼1.54 nm), even after laser ablation. Therefore, these results support the hypothesis that picosecond μLIBS achieves high surface sensitivity to thin layers of contamination on CFRP surfaces with both minimal ablation damage and thermal stress.

The surface sensitivity and limits of detection were investigated by comparing the LIBS Si/C ratio to the Si concentration obtained with XPS. The detection limits of NASA LaRC and BTG Labs were determined to be 0.6 at.% and 0.54 at.%, respectively. The lowest Si concentration obtained by XPS and correlated to the LIBS Si/C ratio was limited by the XPS instrument LOD. The calibration curves allowed LIBS quantification of Si concentration in the CFRP material system. The LIBS Si/C ratio can be used as a parameter to quantify contamination levels when a priori analysis is performed with XPS to determine the initial surface conditions and initial Si concentration prior to laser surface treatment.

The designed LIBS instrument exceeded the goal requirements. This research work demonstrated that LIBS can measure exceptionally low concentrations of contaminants, can distinguish the chemical nature of the contaminant, requires no sample preparation or inert atmosphere to perform the measurement, and provides near instantaneous results.

7.1.3 Contributions

The contributions and achievements of this research work have been documented in peer-reviewed journal articles and conference proceedings, and can be summarized as:

- Detection of very low concentrations of silicone contamination on CFRP surfaces
- Implementation of LIBS apparatus for rapid inspection of CFRP surfaces without sample preparation
- Minimization of ablation damage by microjoule LIBS for inspection of epoxy matrix composites
- Development of process control methods for surface treatment prior to adhesive bonding
- Design and development of advanced process control strategies for state-of-the-art composite adhesive bonding

7.2 Future Work

7.2.1 OSEE

The analysis of OSEE can be advanced by investigating the photocurrent response to obtain the surface chemical kinetics through frequency domain analysis. The chemical kinetics of the adsorbates interacting with the surface and with each other are affected when the surface is irradiated by UV light in the argon environment. The analysis can provide useful information about the chemistry of the contaminant and its concentration. The working hypothesis is that different specific contaminants yield responses in the frequency domain that can be fingerprinted and normalized as a function of concentration. This analysis provides information about the contaminant structure and concentration based on the alteration of the work function of the target surface. This improvement in analysis will overcome some limitations of the current OSEE analysis methods and will enable quantification and chemical characterization of surface contaminants. Through focusing techniques, the spatial resolution of the OSEE measurements can be tailored to overcome challenging structural dimensions. Thus, the inspection area can also be adjusted to increase the spatial resolution, yielding more localized characterization. It is unclear how to mitigate the need for an inert atmosphere to conduct the measurements.

7.2.2 LIBS

Improvements can be implemented in the LIBS apparatus to advance the surface characterization of CFRP composites. In order to achieve detection of surface contamination in real time, the laser parameters for LIBS must be developed in relation to parameters associated with laser ablation cleaning. This is not trivial as laser ablation can be accomplished with a subset of parameters to remove contamination and prepare the surface for adhesive bonding, and those same parameters are not necessarily enough to generate detectable emissions from the induced plasma plume. The limitations are not only the laser-matter interactions or the intensities of the photon emissions from the plasma plume but the photon collection technology and implementation. The challenges to implement LIBS in a manufacturing environment also involve spectral data processing for real-time surface inspections. The data processing software will need to be designed to consider the LIBS timing for light collection, spectral resolution, and LIBS signal analysis for decision making. Spatial resolution can be optimized to cover larger surface regions, enhancing the monitoring process. The light collection optics will need to be arranged such that they can cover larger regions as the laser irradiates the surfaces.

LIBS analysis can be simplified and improved to provide rapid surface screening for deployable application in a manufacturing environment. Calibration curves using LIBS can provide a reference for initial surface conditions before ablation, which are important and can aid adjustment of the laser parameter for cleaning purposes. Therefore, LIBS measurements before and after laser ablation can yield useful results, since the laser ablation cleaning can be conducted again to remove remnants of surface contaminants.

Other laser pulse widths can be explored, as the shorter pulse widths will yield higher peak intensities, and those ultrashort pulses can interact with the polymer matrix more efficiently, allowing the decrease of the average laser power needed to form energetic plasma plumes. As was demonstrated and reported in the literature, short and ultrashort pulses enable photochemical ablation by multiphoton absorption. In addition, laser beams with higher photon energies (shorter wavelengths in the UV and deep UV spectral range) can enable photochemical ablation with reduced laser intensities. The combination of an ultrashort pulse width and high photon energy can be beneficial for the surface characterization of polymer matrix composites as thermal effects will be negligible.

Bibliography

[1] R. Bossi and M. Piehl, "Bonding primary aircraft structure: The issues," *Manuf. Eng.*, vol. 146, no. 3, pp. 101–109, 2011.

[2] "Advisory Circular AC 20-107B, Composite Aircraft Structure," Federal Aviation Administration, 2010.

[3] B. Ehrhart, B. Valeske, R. Ecault, M. Boustie, L. Berthe, and C. Bockenheimer, "Extended NDT for the quality assessment of adhesive bonded CFRP structures." Smart Materials, Structures & NDT in Aerospace Conf., 2011.

[4] D. Markatos, K. Tserpes, E. Rau, K. Brune, and S. Pantelakis, "Degradation of mode-I fracture toughness of CFRP bonded joints due to release agent and moisture pre-bond contamination," *J. Adhes.*, vol. 90, pp. 156–173, 2014.

[5] F. Palmieri, M. Belcher, C. Wohl, K. Blohowiak, and J. Connell, "Laser ablation surface preparation for adhesive bonding of carbon fiber reinforced epoxy composites," *Int. J. Adhes. Adhes.*, vol. 68, pp. 95–101, 2016.

[6] F. Palmieri, R. Ledesma, T. Fulton, A. Arthur, K. Eldridge, S. Thibeault, Y. Lin, C. Wohl, and J. Connell, "Picosecond pulsed laser ablation for the surface preparation of epoxy composites." SAMPE Seattle, 2017.

[7] F. Fischer, S. Kreling, P. Jäschke, M. Frauenhofer, D. Kracht, and K. Dilger, "Laser surface pre-treatment of CFRP for adhesive bonding in consideration of the absorption behaviour," *J. Adhes.*, vol. 88, pp. 350–363, 2012.

[8] F. Fischer, S. Kreling, and K. Dilger, "Surface structuring of CFRP by using modern excimer laser sources," *Phys. Procedia*, vol. 39, pp. 154–160, 2012.

[9] F. Fischer, S. Kreling, F. Gäbler, and R. Delmdahl, "Using excimer lasers to clean CFRP prior to adhesive bonding," *Reinf. Plast.*, vol. 57, pp. 43–46, 2013.

[10] H. Hertz, "Ueber einen Einfluss des ultravioletten Lichtes auf die electrische Entladung," *Ann. Phys. Chem.*, vol. 267, pp. 983–1000, 1887.

[11] W. Hallwachs, "Ueber den Einfluss des Lichtes auf electrostatisch geladene Körper," *Ann. Phys. Chem.*, vol. 269, pp. 301–312, 1888.

[12] J. Thomson, "On the masses of the ions in gases at low pressures," *Philos. Mag.*, vol. 48, pp. 547–567, 1899.

[13] P. Lenard, "Ueber die lichtelektrische Wirkung," *Ann. Phys.*, vol. 313, pp. 149–198, 1902.

[14] A. Einstein, “Über einen die Erzeugung und Verwandlung des Lichtes betreffenden heuristischen Gesichtspunkt,” *Ann. Phys.*, vol. 322, pp. 132–148, 1905.

[15] R. Millikan, “A direct determination of “h”,” *Phys. Rev.*, vol. 4, pp. 73–75, 1914.

[16] R. Millikan, “A direct photoelectric determination of Planck’s “h”,” *Phys. Rev.*, vol. 7, pp. 355–388, 1916.

[17] T. Smith, “Photoelectron emission from aluminum and nickel measured in air,” *J. Appl. Phys.*, vol. 46, pp. 1553–1558, 1975.

[18] T. Smith, “Residual silicone detection,” NASA Technical Report NASA-CR-161643, SC5252.8FR, 1980.

[19] T. Smith, “Detecting contamination with photoelectron emission,” NASA Tech Briefs, 1982.

[20] T. Smith, “Apparatus and technique for monitoring photoelectron emission from surfaces,” 1986, US Patent 4590376.

[21] C. Welch, M. Abedin, and W. Yost, “Optically stimulated electron emission: current-voltage response and spectral sensitivity,” in *Review of Progress in Quantitative Nondestructive Evaluation*, D. Thompson and D. Chimenti, Eds. New York: Plenum Press, 1992, pp. 2155–2162.

[22] W. Yost, C. Welch, E. Joe, and B. Hefner, “Quality monitor and monitoring technique employing optically stimulated electron emission,” 1995, US Patent 5393980.

[23] D. Perey, W. Yost, F. Stone, C. Welch, E. Scales, E. Gasser, E. Joe, T. Goodman, X. Pascual, B. Hefner, and J. Bly, “The design and development of a third generation OSEE instrument,” in *Proc. Aerospace Environmental Technology Conf.*, 1995, pp. 533–540.

[24] G. Gould, “The LASER: light amplification by stimulated emission of radiation,” in *The Ann Arbor Conference on Optical Pumping: The University of Michigan, June 15 Through June 18, 1959*, P. Franken and R. Sands, Eds., 1959, pp. 128–130.

[25] A. Schawlow and C. Townes, “Infrared and optical masers,” *Phys. Rev.*, vol. 112, pp. 1940–1949, 1958.

[26] A. Schawlow and C. Townes, “Masers and maser communications system,” 1960, US Patent 2929922.

[27] T. Maiman, “Stimulated optical radiation in ruby,” *Nat.*, vol. 187, pp. 493–494, 1960.

[28] F. Breck and L. Cross, “Optical microemission stimulated by a ruby maser,” *Appl. Spectrosc.*, vol. 16, p. 59, 1962.

[29] D. Sherman, M. Ruben, H. Goldman, and F. Breck, “The application of laser for the spectrochemical analysis of calcified tissues,” *Ann. N. Y. Acad. Sci.*, vol. 122, pp. 767–772, 1965.

[30] D. Glick, “The laser microprobe its use for elemental analysis in histochemistry,” *J. Histochem. Cytochem.*, vol. 14, pp. 862–868, 1966.

[31] S. Rasberry, B. Scribner, and M. Margoshes, "Laser probe excitation in spectrochemical analysis. I: characteristics of the source," *Appl. Optics*, vol. 6, pp. 81–86, 1967.

[32] P. Maker, R. Terhune, and C. Savage, "Optical third harmonic generation," in *Proc. Third Int. Conf. Quantum Electronics, Paris, 1963*, P. Grivet and N. Bloembergen, Eds., vol. 2. New York: Columbia University Press, 1964, pp. 1559–1579.

[33] J. Ready, "Development of plume of material vaporized by giant-pulse laser," *Appl. Phys. Lett.*, vol. 3, pp. 11–13, 1963.

[34] E. Runge, R. Minck, and F. Bryan, "Spectrochemical analysis using a pulsed laser source," *Spectrochim. Acta*, vol. 20, pp. 733–736, 1964.

[35] J. Debras-Guedon, N. Liodec, and J. Vilnat, "Le laser: Source d'excitation des spectres pour l'analyse qualitative et quantitative par spectrographie," in *Proc. Int. Symp. Laser-Physics and Applications*, vol. 16, 1965, pp. 155–156.

[36] M. Baudelet and B. Smith, "The first years of laser-induced breakdown spectroscopy," *J. Anal. At. Spectrom.*, vol. 28, pp. 624–629, 2013.

[37] M. Berndt, H. Krause, L. Moenke-Blankenburg, and H. Moenke, "Mikro-Emissionsspektralanalyse mit Festkörper-LASER," in *Jenaer Jahrbuch*, 1965, pp. 45–47.

[38] H. Moenke and L. Moenke-Blankenburg, "Laser-Mikrospektralanalyse," *Prakt. Chem. (Wien)*, vol. 16, p. 225, 1965.

[39] J. Daiber and J. Winans, "Radiation from laser-heated plasmas in nitrogen and argon," *J. Opt. Soc. Am.*, vol. 58, pp. 76–80, 1968.

[40] W. Schroeder, J. van Niekerk, L. Dicks, A. Strasheim, and H. Piepen, "A new electronic time resolution system for direct reading spectrometers and some applications in the diagnosis of spark and laser radiations," *Spectrochim. Acta*, vol. 26B, pp. 331–340, 1971.

[41] E. Belyaev, A. Godlevskii, and Y. Kopytin, "Laser spectrochemical analysis of aerosols," *Sov. J. Quantum Electron.*, vol. 8, pp. 1459–1463, 1978.

[42] T. Loree and L. Radziemski, "Laser-induced breakdown spectroscopy: time-integrated applications," *Plasma Chem. Plasma Process.*, vol. 1, pp. 271–279, 1981.

[43] D. Cremers and L. Radziemski, "Detection of chlorine and fluorine in air by laser-induced breakdown spectrometry," *Anal. Chem.*, vol. 55, pp. 1252–1256, 1983.

[44] L. Radziemski, T. Loree, D. Cremers, and N. Hoffman, "Time-resolved laser-induced breakdown spectrometry of aerosols," *Anal. Chem.*, vol. 55, pp. 1246–1252, 1983.

[45] D. Cremers, L. Radziemski, and T. Loree, "Spectrochemical analysis of liquids using the laser spark," *Appl. Spectrosc.*, vol. 38, pp. 721–729, 1984.

[46] H. Häkkänen and J. Korppi-Tommola, "UV-laser plasma study of elemental distributions of paper coatings," *Appl. Spectrosc.*, vol. 49, pp. 1721–1728, 1995.

[47] D. Cremers, J. Barefield, and A. Koskelo, "Remote elemental analysis by laser-induced breakdown spectroscopy using a fiber-optic cable," *Appl. Spectrosc.*, vol. 49, pp. 857–860, 1995.

[48] B. Marquardt, S. Goode, and S. Angel, “In situ determination of lead in paint by laser-induced breakdown spectroscopy using a fiber-optic probe,” *Anal. Chem.*, vol. 68, pp. 977–981, 1996.

[49] H. Bauer, F. Leis, and K. Niemax, “Laser induced breakdown spectrometry with an echelle spectrometer and intensified charge coupled device detection,” *Spectrochim. Acta Part B*, vol. 53, pp. 1815–1825, 1998.

[50] A. Ciucci, M. Corsi, V. Palleschi, S. Ratelli, A. Salvetti, and E. Tognoni, “New procedure for quantitative elemental analysis by laser-induced plasma spectroscopy,” *Appl. Spectrosc.*, vol. 53, pp. 960–964, 1999.

[51] B. A. Ali, D. Bulajic, M. Corsi, G. Cristoforetti, S. Legnaioli, L. Masotti, V. Palleschi, A. Salvetti, and E. Tognoni, “μ-LIBS/μ-Raman spectroscopic analysis of pigments in a Roman fresco,” in *Proc. SPIE, Laser Techniques and Systems in Art Conservation*, vol. 4402, 2001.

[52] S. Lui, Y. Godwal, M. Taschuk, Y. Tsui, and R. Fedosejevs, “Detection of lead in water using laser-induced breakdown spectroscopy and laser-induced fluorescence,” *Anal. Chem.*, vol. 80, pp. 1995–2000, 2008.

[53] L. Radziemski and D. Cremers, *Laser-Induced Plasmas and Applications.* New York: Marcel Dekker, 1989.

[54] A. Miziolek, V. Palleschi, and I. Schechter, *Laser-Induced Breakdown Spectroscopy (LIBS).* New York: Cambridge University Press, 2006.

[55] D. Cremers and L. Radziemski, *Handbook of Laser-Induced Breakdown Spectroscopy*, 2nd ed. Chichester: John Wiley and Sons, 2013.

[56] J. Singh and S. Thakur, *Laser-Induced Breakdown Spectroscopy.* Amsterdam: Elsevier Science, 2007.

[57] R. Noll, *Laser-Induced Breakdown Spectroscopy.* Berlin: Springer, 2012.

[58] S. Musazzi and U. Perini, *Laser-Induced Breakdown Spectroscopy.* Berlin: Springer, 2014.

[59] D. Hahn and N. Omenetto, “Laser-induced breakdown spectroscopy (LIBS), part I: review of basic diagnostics and plasma-particle interactions: still-challenging issues within the analytical plasma community,” *Appl. Spectrosc.*, vol. 64, pp. 335A–366A, 2010.

[60] D. Hahn and N. Omenetto, “Laser-induced breakdown spectroscopy (LIBS), part II: review of instrumental and methodological approaches to material analysis and applications to different fields,” *Appl. Spectrosc.*, vol. 66, pp. 347–419, 2012.

[61] N. Lanza, R. Wiens, S. Clegg, A. Ollila, S. Humphries, H. Newsom, J. Barefield, and the ChemCam team, “Calibrating the ChemCam laser-induced breakdown spectroscopy instrument for carbonate minerals on Mars,” *Appl. Opt.*, vol. 49, pp. C211–C217, 2010.

[62] E. Lakdawalla, “The story behind Curiosity’s self-portraits on Mars,” *The Planetary Society*, 2015, http://www.planetary.org/blogs/emily-lakdawalla/2015/08191059-curiosity-self-portrait-history-belly-pan.html.

[63] R. Wiens, S. Maurice, and the ChemCam team, “The ChemCam instrument suite on the Mars Science Laboratory rover Curiosity: remote sensing by laser-induced plasmas,” *Geochemical News*, vol. 145, pp. 41–48, 2011.

[64] R. Gause, “A noncontacting scanning photoelectron emission technique for bonding surface cleanliness inspection.” 5th Annual NASA NDE Workshop, 1987.

[65] C. Allen, C. Kerr, and P. Walker, “The use of optically stimulated electron emission for the detection of surface contamination,” in *Adhesion 15*, K. Allen, Ed. New York: Elsevier, 1991, pp. 131–147.

[66] G. Epstein and S. Shlanger, “Optically stimulated electron emission (OSEE): A non-invasive technique for contamination detection,” in *Review of Progress in Quantitative Nondestructive Evaluation*, D. Thompson and D. Chimenti, Eds. New York: Plenum Press, 1991, pp. 589–596.

[67] R. Mattes, “Cleanliness inspection tool for RSRM bond surfaces,” in *Proc. Aerospace Environmental Technology Conf.*, 1995, pp. 525–531.

[68] C. Welch and W. Yost, “Enhancements and extensions to OSEE contamination inspection,” in *Review of Progress in Quantitative Nondestructive Evaluation*, D. Thompson and D. Chimenti, Eds. New York: Plenum Press, 1995, pp. 1641–1648.

[69] M. Lingbloom, “Using optically stimulated electron emission as an inspection method to monitor surface contamination.” Am. Soc. Nondestr. Test. Fall Conf., 2008.

[70] K. Brune, L. Lima, M. Noeske, K. Thiel, C. Tornow, S. Dieckhoff, M. Hoffmann, and D. Stübing, “Pre-bond quality assurance of CFRP surfaces using optically stimulated electron emission,” in *Proc. 3rd Int. Conf. Engineering Against Failure*, 2013, pp. 300–307.

[71] K. Brune, C. Tornow, M. Noeske, T. Wiesner, A. Q. Barbosa, S. Stamboroski, S. Dieckhoff, and B. Mayer, “Surface analytical approaches contributing to quality assurance during manufacture of functional interfaces,” *Appl. Adhes. Sci.*, vol. 3, 2015.

[72] S. Markus, R. Wilken, S. Dieckhoff, and O.-D. Hennemann, “Quality monitoring of CFRP surfaces in bonding and coating processes,” in *Proc. 16th Int. Conf. Surface Treatments in the Aeronautic and Aerospace Industries, SURFAIR*, 2006.

[73] C. Tornow, M. Schlag, L. Lima, D. Stübing, M. Hoffmann, P.-L. Noeske, K. Brune, and S. Dieckhoff, “Quality assurance concepts for adhesive bonding of composite aircraft structures - characterisation of adherent surfaces by extended NDT,” *J. Adhes. Sci. Technol.*, vol. 29, pp. 2281–2294, 2015.

[74] “Fraunhofer Institute for Manufacturing Technology and Advanced Materials,” ENCOMB Report Summary, 2015, https://cordis.europa.eu/result/rcn/156281_en.html.

[75] R. Ledesma, F. Palmieri, J. Connell, W. Yost, and J. Fitz-Gerald, “Surface characterization of carbon fiber reinforced polymers by picosecond laser induced breakdown spectroscopy,” *Spectrochim. Acta, Part B*, vol. 140, pp. 5–12, 2017.

[76] R. Maurer, “Photoelectric effect,” in *Handbook of Physics*, E. Condon and H. Odishaw, Eds. New York: McGraw-Hill, 1967.

[77] M. Tran, B. Smith, D. Hahn, and J. Winefordner, "Detection of gaseous and particulate fluorides by laser-induced breakdown spectroscopy," *Appl. Spectrosc.*, vol. 55, pp. 1455–1461, 2001.

[78] E. Campbell, D. Ashkenasi, and A. Rosenfeld, "Ultra-short-pulse laser irradiation and ablation of dielectrics," *Mater. Science Forum*, vol. 301, pp. 123–144, 1999.

[79] B. Stuart, M. Feit, S. Herman, A. Rubenchik, B. Shore, and M. Perry, "Nanosecond-to-femtosecond laser-induced breakdown in dielectrics," *Phys. Rev. B*, vol. 53, pp. 1749–1761, 1996.

[80] R. Russo, X. Mao, J. Yoo, and J. Gonzalez, "Laser ablation," in *Laser-Induced Breakdown Spectroscopy*, J. Singh and S. Thakur, Eds. Amsterdam: Elsevier Science, 2007.

[81] S. Rand, "Inverse bremsstrahlung with high-intensity radiation fields," *Phys. Rev.*, vol. 136, pp. B231–B237, 1964.

[82] X. Mao and R. Russo, "Observation of plasma shielding by measuring transmitted and reflected laser pulse temporal profiles," *Appl. Phys. A*, vol. 64, pp. 1–6, 1997.

[83] I. Mihailescu and J. Hermann, "Laser-plasma interactions," in *Laser Processing of Materials*, P. Schaaf, Ed. Heidelberg: Springer, 2010.

[84] D. Breitling, H. Schittenhelm, P. Berger, F. Dausinger, and H. Hügel, "Shadowgraphic and interferometric investigations on Nd:YAG laser-induced vapor/plasma plumes for different processing wavelengths," *Appl. Phys. A*, vol. 69, pp. s505–s508, 1999.

[85] V. Rai and S. Thakur, "Physics of plasma in laser-induced breakdown spectroscopy," in *Laser-Induced Breakdown Spectroscopy*, J. Singh and S. Thakur, Eds. Amsterdam: Elsevier Science, 2007.

[86] B. Garrison and R. Srinivasan, "Laser ablation of organic polymers: microscopic models for photochemical and thermal processes," *J. Appl. Phys.*, vol. 57, pp. 2909–2914, 1985.

[87] J. Kephart, R. Godwin, and G. McCall, "Bremsstrahlung emission from laser-produced plasmas," *Appl. Phys. Lett.*, vol. 25, pp. 108–109, 1974.

[88] G. Bekefi, C. Deutsch, and B. Yaakobi, "Spectroscopic diagnostics of laser plasmas," in *Principles of Laser Plasmas*, G. Bekefi, Ed. New York: Wiley Interscience, 1976, pp. 549–669.

[89] S. Thakur, "Atomic emission spectroscopy," in *Laser-Induced Breakdown Spectroscopy*, J. Singh and S. Thakur, Eds. Amsterdam: Elsevier Science, 2007.

[90] M. Shirk and P. Molian, "A review of ultrashort pulsed laser ablation of materials," *J. Laser Appl.*, vol. 10, pp. 18–28, 1998.

[91] R. Russo, "Short-pulse LIBS: fundamentals and applications," in *Laser-Induced Breakdown Spectroscopy (LIBS)*, A. Miziolek, V. Palleschi, and I. Schechter, Eds. New York: Cambridge University Press, 2006, pp. 477–489.

[92] D. Bäuerle, "Ultrashort-pulse laser ablation," in *Laser Processing and Chemistry*, 4th ed. Berlin: Springer, 2011, pp. 279–313.

[93] T. Qiu and C. Tien, "Short-pulse laser heating on metals," *Int. J. Heat and Mass Transfer*, vol. 35, pp. 719–726, 1992.

[94] B. Chichkov, C. Momma, S. Nolte, F. von Alvensleben, and A. Tünnermann, "Femtosecond, picosecond and nanosecond laser ablation of solids," *Appl. Phys. A: Mater. Sci. Process.*, vol. 63, pp. 109–115, 1996.

[95] M. Gedvilas and G. Raciukaitis, "Investigation of UV picosecond laser ablation of polymers," in *Proc. SPIE, Workshop on Laser Applications in Europe*, vol. 6157, 2005.

[96] W. Kautek and M. Forster, "Ultrafast laser micro- and nanostructuring," in *Laser Precision Microfabrication*, K. Sugioka, M. Meunier, and A. Piqué, Eds. Berlin: Springer, 2010, pp. 189–213.

[97] C. Elton, "Atomic processes," in *Plasma Physics, Part A*, H. Griem and R. Lovberg, Eds. New York: Academic Press, 1970.

[98] D. Cremers and L. Radziemski, "History and fundamentals of LIBS," in *Laser-Induced Breakdown Spectroscopy (LIBS)*, A. Miziolek, V. Palleschi, and I. Schechter, Eds. New York: Cambridge University Press, 2006.

[99] D. Bäuerle, "Nanosecond-laser ablation," in *Laser Processing and Chemistry*, 4th ed. Berlin: Springer, 2011, pp. 237–278.

[100] D. von der Linde, K. Sokolowski-Tinten, and J. Bialkowski, "Laser-solid interaction in the femtosecond time regime," *Appl. Surf. Sci.*, vol. 109–110, pp. 1–10, 1997.

[101] R. Srinivasan and B. Braren, "Ultraviolet laser ablation of organic polymers," *Chem. Rev.*, vol. 89, pp. 1303–1316, 1989.

[102] R. Stoian, D. Ashkenasi, A. Rosenfeld, and E. Campbell, "Coulomb explosion in ultrashort pulsed laser ablation of Al_2O_3," *Phys. Rev. B*, vol. 62, pp. 13 167–13 173, 2000.

[103] B. Magyar, *Guide-Lines to Planning Atomic Spectrometric Analysis.* New York: Elsevier Science, 1982.

[104] W. Martin and W. Wiese, "Atomic spectroscopy," in *Handbook of Atomic, Molecular, and Optical Physics*, G. Drake, Ed. New York: Springer, 2006.

[105] H. Griem, *Spectral Line Broadening by Plasmas.* New York: Academic Press, 1974.

[106] S. Harilal, C. Bindhu, R. Isaac, V. Nampoori, and C. Vallabhan, "Electron density and temperature measurements in a laser produced carbon plasma," *J. Appl. Phys.*, vol. 82, pp. 2140–2146, 1997.

[107] I. Gornushkin, L. King, B. Smith, N. Omenetto, and J. Winefordner, "Line broadening mechanisms in the low pressure laser-induced plasma," *Spectrochim. Acta, Part B*, vol. 54, pp. 1207–1217, 1999.

[108] G. Rieger, M. Taschuk, Y. Tsui, and R. Fedosejevs, "Laser-induced breakdown spectroscopy for microanalysis using submillijoule UV laser pulses," *Appl. Spectrosc.*, vol. 56, pp. 689–698, 2002.

[109] G. Rieger, M. Taschuk, Y. Tsui, and R. Fedosejevs, “Comparative study of laser-induced plasma emission from microjoule picosecond and nanosecond KrF-laser pulses,” *Spectrochim. Acta, Part B*, vol. 58, pp. 497–510, 2003.

[110] I. Gornushkin, K. Amponsah-Manager, B. Smith, N. Omenetto, and J. Winefordner, “Microchip laser-induced breakdown spectroscopy: A preliminary feasibility investigation,” *Appl. Spectrosc.*, vol. 71, pp. 762–769, 2004.

[111] M. Taschuk, Y. Tsui, and R. Fedosejevs, “Detection and mapping of latent fingerprints by laser-induced breakdown spectroscopy,” *Appl. Spectrosc.*, vol. 60, pp. 1322–1327, 2006.

[112] S. Banerjee and R. Fedosejevs, “Single shot depth sensitivity using femtosecond laser induced breakdown spectroscopy,” *Spectrochim. Acta, Part B*, vol. 92, pp. 34–41, 2014.

[113] D. Perey, “A portable surface contamination monitor based on the principle of optically stimulated electron emission (OSEE).” JANNAF Propulsion and Joint Subcommittee Meeting, 1996.

[114] C. Palmer, *Diffraction Grating Handbook*, 6th ed. New York: Newport Corporation, 2005.

[115] J. McClure, “Anastigmatic imaging spectrograph,” 2014, US Patent 8773659.

[116] J. McClure, “The Schmidt-Czerny-Turner spectrograph,” in *Proc. SPIE, Photonic Innovations and Solutions for Complex Environments and Systems II*, vol. 9189, 2014.

[117] R. Ledesma, F. Palmieri, J. Fitz-Gerald, and J. Connell, “Determination of cross-sectional area of focused picosecond Gaussian laser beam,” NASA/TM-2018-219809, 2018.

[118] I. Winer, “A self-calibrating technique measuring laser beam intensity distributions,” *Appl. Opt.*, vol. 5, pp. 1437–1439, 1966.

[119] M. Mauck, “Knife-edge profiling of Q-switched Nd:YAG laser beam and waist,” *Appl. Opt.*, vol. 18, pp. 599–600, 1979.

[120] J. Liu, “Simple technique for measurements of pulsed Gaussian-beam spot sizes,” *Opt. Lett.*, vol. 7, pp. 196–198, 1982.

[121] Y. Kiang and R. Lang, “Measuring focused Gaussian beam spot sizes: A practical method,” *Appl. Opt.*, vol. 22, pp. 1296–1297, 1983.

[122] J. Krüger and W. Kautek, “Ultrashort pulse laser interaction with dielectrics and polymers,” *Adv. Polym. Sci.*, vol. 168, pp. 247–289, 2004.

[123] V. Lednev, S. Pershin, E. Obraztsova, S. Kudryashov, and A. Bunkin, “Single-shot and single-spot measurement of laser ablation threshold for carbon nanotubes,” *J. Phys. D: Appl. Phys.*, vol. 46, p. 052002, 2013.

[124] Y. Roichman, A. Waldron, E. Gardel, and D. Grier, “Optical traps with geometric aberrations,” *Appl. Opt.*, vol. 45, pp. 3425–3429, 2006.

[125] H. Sun, “Laser diode beam basics,” in *A Practical Guide to Handling Laser Diode Beams*. Springer Netherlands, 2015, pp. 27–51.

[126] J. Alda, “Laser and Gaussian beam propagation and transformation,” in *Encyclopedia of Optical and Photonic Engineering*, C. Hoffman and R. Driggers, Eds. CRC Press, 2015, pp. 1–15.

[127] H. Haskal and A. Rosen, “Power and focusing considerations for recording with a laser beam in the TEM_{00} mode,” *Appl. Opt.*, vol. 10, pp. 1354–1358, 1971.

[128] S. Preuss, A. Demchuk, and M. Stuke, “Sub-picosecond UV laser ablation of metals,” *Appl. Phys. A*, vol. 61, pp. 33–37, 1995.

[129] J. Byskov-Nielsen, J.-M. Savolainen, M. Christensen, and P. Balling, “Ultra-short pulse laser ablation of copper, silver and tungsten: experimental data and two-temperature model simulations,” *Appl. Phys. A*, vol. 103, pp. 447–453, 2011.

[130] R. Sniaukasa and G. Raciukaitis, “Laser micro-cutting of thick tungsten sheets.” Lasers in Manufacturing Conference, 2015.

[131] M. Pfeifenberger, M. Mangang, S. Wurster, J. Reiser, A. Hohenwarter, W. Pfleging, D. Kiener, and R. Pippan, “The use of femtosecond laser ablation as a novel tool for rapid micro-mechanical sample preparation,” *Mater. Des.*, vol. 121, pp. 109–118, 2017.

[132] R. Ledesma, W. Yost, F. Palmieri, D. Cataldo, and J. Connell, “Correlation of optically stimulated electron emission with failure mode of adhesively bonded epoxy composites,” *Int. J. Adhes. Adhes.*, vol. 84, pp. 257–264, 2018.

[133] F. Palmieri, R. Ledesma, D. Cataldo, Y. Lin, C. Wohl, M. Gupta, and J. Connell, “Controlled contamination of epoxy composites with PDMS and removal by laser ablation.” SAMPE Long Beach, 2016.

[134] “ASTM D5528-13, Standard test method for mode I interlaminar fracture toughness of unidirectional fiber-reinforced polymer matrix composites,” ASTM International, 2013.

[135] “ASTM D5573-99, Standard practice for classifying failure modes in fiber-reinforced-plastic (FRP) joints,” ASTM International, 2012.

[136] J. Woollam, P. Snyder, and M. Rost, “Variable angle spectroscopic ellipsometry: a nondestructive characterization technique for ultrathin and multilayer materials,” *Thin Solid Films*, vol. 166, pp. 317–323, 1988.

[137] J. Woollam and P. Snyder, “Fundamentals and applications of variable angle spectroscopic ellipsometry,” *Mater. Sci. Eng. B*, vol. 5, pp. 279–283, 1990.

[138] W. Rasband, “ImageJ,” U.S. National Institutes of Health, Bethesda, Maryland, USA, http://imagej.nih.gov/ij/, 1997–2016.

[139] V.-M. Graubner, R. Jordan, O. Nuyken, T. Lippert, M. Hauer, B. Schnyder, and A. Wokaun, “Incubation and ablation behavior of poly(dimethylsiloxane) for 266 nm irradiation,” *Appl. Surf. Sci.*, vol. 197–198, pp. 786–790, 2002.

[140] H. Koizumi, K. Lacmann, and W. Schmidt, “Light-induced electron emission from silicone oils,” *J. Phys. D: Appl. Phys.*, vol. 25, pp. 857–861, 1992.

[141] R. Ledesma, F. Palmieri, J. Dennie, J. Dowdell, J. Fitz-Gerald, and J. Connell, "Detection of trace silicone contamination on CFRP surfaces by picosecond LIBS." The Adhesion Society, 2018.

[142] Y. Chekanov, R. Ohnogi, S. Asai, and M. Sumita, "Electrical properties of epoxy resin filled with carbon fibers," *J. Mater. Sci.*, vol. 34, pp. 5589–5592, 1999.

[143] F. Palmieri, J. Hopkins, C. Wohl, Y. Lin, J. Connell, M. Belcher, and K. Blohowiak, "Laser surface preparation of epoxy composites for secondary bonding: optimization of ablation depth." SAMPE Baltimore, 2015.

[144] "DIN EN ISO 11562, Geometrical Product Specifications - Surface texture: Profile method - Metrological characteristics of phase correct filters," International Organization for Standardization, 1998.

[145] R. Ledesma, F. Palmieri, J. Connell, W. Yost, and J. Fitz-Gerald, "Surface characterization of carbon fiber reinforced polymers by picosecond laser induced breakdown spectroscopy," *Spectrochim. Acta, Part B*, vol. 140, pp. 5–12, 2017.

[146] A. Ben-Yakar and R. Byer, "Femtosecond laser ablation properties of borosilicate glass," *J. Appl. Phys.*, vol. 96, pp. 5316–5323, 2004.

[147] M. Taschuk, "Quantification of laser-induced breakdown spectroscopy at low energies," Ph.D. dissertation, University of Alberta, Canada, 2007.

[148] S. Banerjee and R. Fedosejevs, "Single shot depth sensitivity using femtosecond laser induced breakdown spectroscopy," *Spectrochim. Acta, Part B*, vol. 92, pp. 34–41, 2014.

[149] R. Ledesma, F. Palmieri, B. Campbell, W. Yost, J. Fitz-Gerald, G. Dillingham, and J. Connell, "Correlation of trace silicone contamination analyses on epoxy composites by X-ray photoelectron spectroscopy (XPS) and laser induced breakdown spectroscopy (LIBS)," *Appl. Spectrosc.*, 2018, (https://doi.org/10.1177/0003702818809928).

[150] F. Palmieri, M. Belcher, C. Wohl, K. Blohowiak, and J. Connell, "Laser ablation surface preparation of carbon fiber reinforced epoxy composites for adhesive bonding." SAMPE Long Beach, 2013.

[151] X. Fang, J. Jalowka, J. Riehl, W. Zhao, and D. Goberman, "Contamination effect on composite-to-metal adhesive bond performance." SAMPE Seattle, 2017.

[152] E. Kutscha, P. Vahey, M. Belcher, P. VanVoast, W. Grace, K. Blohowiak, F. Palmieri, and J. Connell, "Contamination and surface preparation effects on composite bonding." SAMPE Seattle, 2017.

[153] M. Belcher, C. Wohl, J. Hopkins, and J. Connell, "Laser surface preparation for bonding of aerospace composites," *Proc. Inst. Civ. Eng.: Eng. Comp. Mech.*, vol. 164, pp. 133–138, 2011.

[154] F. Palmieri, K. Watson, G. Morales, T. Williams, R. Hicks, C. Wohl, J. Hopkins, and J. Connell, "Laser ablative surface treatment for enhanced bonding of Ti-6Al-4V alloy," *ACS Appl. Mater. Interfaces*, vol. 5, pp. 1254–1261, 2013.

[155] C. Wohl, M. Belcher, J. Connell, and J. Hopkins, “Modification of surface energy via direct laser ablative surface patterning,” 2015, US Patent 8987632.

[156] I. Cravetchi, M. Taschuk, Y. Tsui, and R. Fedosejevs, “Evaluation of femtosecond LIBS for spectrochemical microanalysis of aluminium alloys,” *Anal. Bioanal. Chem.*, vol. 385, pp. 287–294, 2006.

[157] A. Eppler, D. Cremers, D. Hickmott, M. Ferris, and A. Koskelo, “Matrix effects in the detection of Pb and Ba in soils using laser-induced breakdown spectroscopy,” *Appl. Spectrosc.*, vol. 50, pp. 1175–1181, 1996.

[158] D. Blass, S. Kreling, S. Nyga, T. Westphalen, B. Jungbluth, H.-D. Hoffmann, and K. Dilger, “CFRP bonding pre-treatment with laser radiation of 3 μm wavelength: laser/material interaction,” in *Proc. SPIE, Laser-based Micro- and Nanoprocessing X*, vol. 9736, 2016.

[159] K. Takahashi, M. Tsukamoto, S. Masuno, and Y. Sato, “Heat conduction analysis of laser CFRP processing with IR and UV laser light,” *Composites, Part A*, vol. 84, pp. 114–122, 2016.